Deformation Mechanisms and Weldability in High Entropy Alloys

A Dissertation
Presented in Partial Fulfillment of the Requirements for the
Degree of Doctor of Philosophy
with a
Major in Materials Science and Engineering
in the
College of Graduate Studies
University of Idaho
by
Anumat Sittiho

Major Professor: Indrajit Charit, Ph.D.
Committee Members: Krishnan Raja, Ph.D.; Samrat Choudhury, Ph.D.; Thomas Williams, Ph.D.
Department Administrator: Mark Roll, Ph.D.

August 2021

Authorization to Submit Dissertation

This dissertation of Anumat Sittiho, submitted for the degree of Doctor of Philosophy with a Major in Materials Science and Engineering and titled "Deformation Mechanisms and Weldability in High Entropy Alloys," has been reviewed in final form. Permission, as indicated by the signatures and dates below, is now granted to submit final copies to the College of Graduate Studies for approval.

Major Professor: ____ Date: ____________
Indrajit Charit, Ph.D.

Committee Members: ____ Date: ____________
Krishnan Raja, Ph.D.

____ Date: ____________
Samrat Choudhury, Ph.D.

____ Date: ____________
Thomas Williams, Ph.D.

Department
Administrator: ____ Date: ____________
Mark Roll, Ph.D.

Abstract

High entropy alloys (HEAs) are an emerging type of metallic materials which are generally comprised of five or more fundamental elements. Because of the influence of configurational entropy, HEAs exhibit a simple single phase which is beneficial in alloy design and applications. For structural application, HEAs show an interesting combination between strength and ductility compared to conventional alloys because of twinning induced plasticity (TWIP) and transformation induced plasticity (TRIP). Selected HEA alloys, $Al_{0.4}CoCrFeNi$ and $Fe_{42}Mn_{28}Cr_{10}Cr_{15}Si_5$, with TWIP and TRIP characteristics, respectively, are used in this study.

The characteristic of transformative HEA and its weldability are studied through TRIP HEA by using friction stir welding/processing (FSP/W) and pressure resistance welding techniques. The FSP of TRIP HEA is done using a tungsten rhenium tool with the parameters of a rotational speed of 300 rpm, traverse speed of 25.4 mm/min, and forging force of 30 kN. The FSPed specimen then was examined for its mechanical properties and microstructural relationship compared to the base metal specimen. The microstructural study is performed through the optical microscope, x-ray diffraction, transmission electron microscope, and scanning electron microscope. Mechanical properties of both specimens are tests using Vickers microhardness for mapping the weld cross-section and uniaxial compression for revealing the flow behavior of the specimens. The TRIP HEA displays good weldability when using the FSW technique. The microstructure undergoes dynamic recrystallization followed by gamma to epsilon phase transformation during FSP. The superior strength of the FSPed specimen compared to the base metal is the result of different martensitic transformation behavior as elucidated by the microstructural observation.

Pressure resistance welding (PRW) is applied to conduct PRW weldability of the TRIP HEA. The weld parameters are varied to prototype the welding parameter on this type of material. The microstructural analysis utilizing optical microscopy and scanning electron microscopy to evaluate the quality of the weld in the TRIP HEA. The finite element analysis using the electro-thermo-structural analysis model is created to visualize the heat generation and material behavior during the PRW process.

Mechanical properties in both macro and micro scales of TWIP HEA are studied through bulk compression testing and micropillar testing. The relationship between micro and macro scale is compared. Phase transformation characterization is done by using optical metallography, X-ray diffraction, and electron microscopy methods. The results reveal the dislocation dynamics during the deformation enhance the strain hardening in the alloys by forming dislocation microbands that initiate from the formation of Lomer-Cottrell lock dislocation.

Thermal stabilities of the TWIP HEA involving second phase precipitation, high-temperature flow behavior, and thermal expansion are studied by using Vickers microhardness, high-temperature uniaxial compression testing, and dilatometer. The B2 phase precipitation kinetics can be explained by using the JMA model (Avrami's kinetic). The flow curves at 600^{o}C display serration flow which can be the effect of dynamic strain aging. The alloy shows no strain rate sensitivity in the homogenized specimen but small inverse strain rate sensitivity in the as-cast specimen. The thermal expansion of this alloy is higher compared to the other conventional FCC alloys and HEAs.

Acknowledgments

First, I would like to express deep and sincere gratitude toward my major professor, Professor Indrajit Charit, for having me in his research group during the past 4 years of my Ph.D. study. I am very grateful for his trust, time, patience, and dedication. He has permitted me to carry on the research from my ideas since the beginning of the research. He also helps me get reach to novel experimental area which is a paradigm of research up to date.

I would like to express my sincere gratitude and respect to all my committee members, Professor Krishnan Raja, Dr. Samrat Choudhury, Dr. Thomas Williams, for their invaluable comments and time for improving my dissertation quality.

I would like to acknowledge Dr. Eric Aston and Dr. Mark Roll as the chair of the Department of Chemical and Material Science and Engineering at the University of Idaho and other faculty members. I appreciate other department staff, Mrs. Margaret Baker, Mrs. Gail Bergman, Dr. Dave McPherson, and Mr. Charles Cornwall for assisting me in any endeavors for a lot of years.

I would like to also thank Dr. Rajiv Mishra for giving the high entropy alloy materials for this research. Dr. Sanjit Bhowmick, Brukers, for helping me in conducting the micro compression testing and permitting me to the analysis software to create stunning results.

Thank my fellow lab mates, Ankan Guria and Cody Hill, for introducing me to metallurgy research. Dr. Arnab Kundu, Dr. Madhumanti Bhattacharyya, Mr. Martin Taylors, Mr. Dallas Robert, Mr. Alli Hussam, Dr. Brandon Day, and Norah, for the research discussions, for a new perspective on my research, and all the fun we have had during our time in the research group. Also, I thank my other friends at The University of Idaho. I would like to also thank Dr. Cody Steven for the insightful discussion and suggestion on the electron microscopy technique.

Also, I am grateful for my non-academic friends around the Palouse area, Mrs. Tanya Nitta, Mr. William Bill, and Mrs. Apiradee Tak Siegwart, Mrs. Sara Shingle, and Mr. David and Mrs. Brenda Howards, for kindness and friendship that make memorable experiences during the time I am studying here.

Finally, I am thankful to The Royal Thai Navy for the financial aid and scholarship during the time I am studying at the University of Idaho.

Dedication

This dissertation is dedicated to my wife Nan and my children Galin, Tywyn, Marvin, and Marlin.

Table of Contents

List of Figures

List of Tables

Chapter 1: Introduction

1.1 Motivations and objectives

Metallic materials have evolved through human history along with the technique and elements that are used for making tools and components. In practice, pure metals find only little use due to the lack of strength. This issue is overcome by using alloys by introducing a small number of solute elements into a larger number of solvent elements. Conventionally, the alloy systems have base metals and alloying elements, *i.e.,* steel is made by alloying carbon in iron, stainless steel is made by alloying chromium, and carbon in iron. Normally, the alloying element will not exceed 10% for conventional alloys.

In order to facilitate the development of a new generation of metallic alloys, multiple elements are introduced to the system in an equimolar fashion. These new alloy systems are called high entropy alloys because of their high configurational entropy. The concept of high entropy alloys has opened a new era of alloy design because it stretches the possibility of obtaining alloys to a large number instead of only several tens of systems in the conventional alloy system paradigm.

Some high entropy alloys show unique plasticity modes which are transformation induced plasticity (TRIP) and twining induced plasticity (TWIP) effect. These deformation modes are beneficial because they help alloys overcome the strength-ductility trade-off found in most conventional metallic alloys.

The primary aim of this work is to study the weldability and effect of transformative HEA (CoCrFeMnSi) on the quality of the weld by using two solid-state welding techniques, namely, friction stir welding/processing and pressure resistance welding. Another aim is to fundamentally study the plasticity in the TWIP HEA ($Al_{0.4}$CoCrFeNi) in both macroscale and microscale and its thermal stability.

1.2 Background

1.2.1 Thermodynamics of phase transformations

Phase transformations of metals and alloys are guided by the thermodynamics of the systems. Under constant temperature and pressure, the system changes are dictated by the changes in Gibbs free energy, which is derived from the change in enthalpy and entropy of the system. The change in Gibbs free energy can be expressed as Equation (1.1).

$$\Delta G = \Delta H - T\Delta S \qquad (1.1)$$

where G is Gibbs free energy, H is enthalpy, T is temperature, and S is an entropy of the system. The system is said to be at equilibrium when the change in the free energy is equal to zero represented in

Figure 1. For the system to be in equilibrium, the combination between enthalpy and entropy of the system must be at its localized minimum.

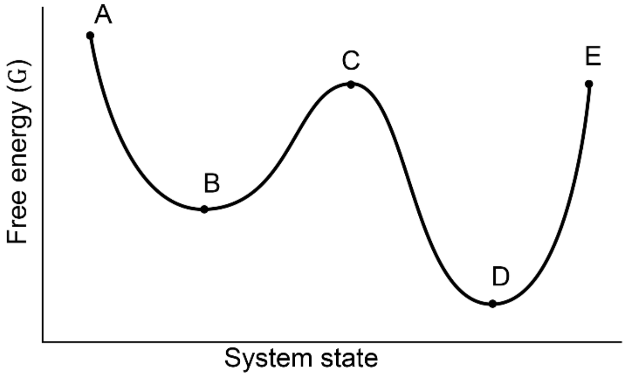

Figure 1.1. Schematic of free energy in different states of an arbitrary system.

The variables in Equation (1), G, H, and S are state variables. That means there is no absolute value and no consideration along the path of the reaction, but they can be measured by determining the initial and the end state of a system. From **Figure 1**, the system goes through phase transformation from point A to point E. Two states show steady-state ($dG = 0$), *i.e.*, point B and point D. However, when the whole phase transformation process is considered, G_{D-A} is smaller than G_{B-A}. Then D state is the steady-state of the system and the B state is called the metastable state.

1.2.1.2 Enthalpy

Enthalpy (H) is the total heat content of the system. In thermodynamics, enthalpy is a state variable which is the sum of internal energy plus product of pressure and volume of the system. Enthalpy can be expressed in the mathematical formula as Equation (1.2)

$$H = U + PV \qquad (1.2)$$

where U is the internal energy of the system, P is the pressure, and V is the volume of the system. In a simple situation, when the pressure and volume remain constant during the process, *i.e.*, in a solid or liquid state, enthalpy is equal to the internal energy of the system and enthalpy becomes the change in heat of the process.

$$\Delta H = \Delta U = q \qquad (1.3)$$

where q is the heat input or output of the system. This relation is a predominant view in thermodynamic of phase transformation. Enthalpy is dependent on temperature. For an ideal gas, under constant pressure and constant volume as shown in the following Equation 1.4. [1].

$$\Delta H = C_p \Delta T \qquad (1.4\ \text{-}1)$$

$$\Delta H = C_v \Delta T \qquad (1.4\ \text{-}2)$$

Enthalpy is an important variable to consider in making an alloy as it dictates the outcome of the alloy phase present at the final. This happens when two elements are bonding; they emit or absorb the heat of mixing, H_{mix}.

$$H_{mix} = \Delta H_{mix} + \sum C_i H_i \qquad (1.5)$$

where C_i is the mole fraction of substance and H_i is the enthalpy of pure substance. This heat of mixing can be calculated by using Miaedema's theory [2-5] but often be measured experimentally. Troparevsky *et al*. [6] used data mining and calculated the enthalpy of formation of binary alloy from transition elements as shown in **Figure 1.2**. The chart shows the enthalpy of formation between elemental pairs listed on each row and column.

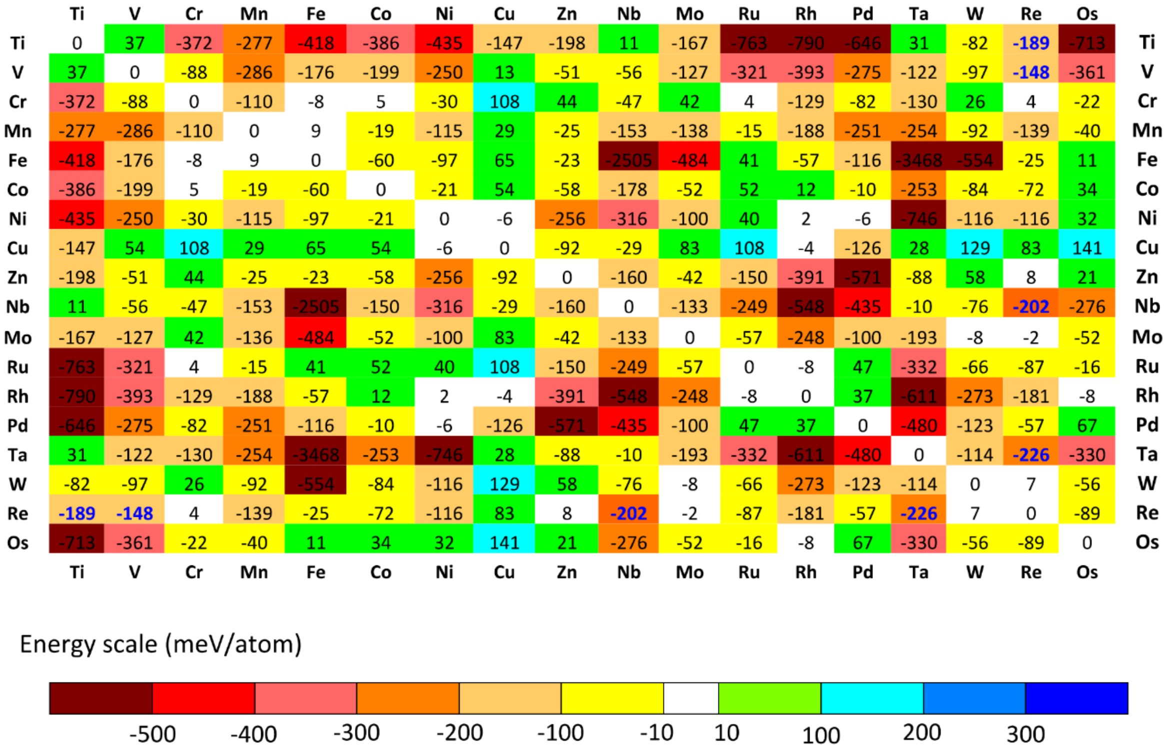

	Ti	V	Cr	Mn	Fe	Co	Ni	Cu	Zn	Nb	Mo	Ru	Rh	Pd	Ta	W	Re	Os	
Ti	0	37	-372	-277	-418	-386	-435	-147	-198	11	-167	-763	-790	-646	31	-82	**-189**	-713	**Ti**
V	37	0	-88	-286	-176	-199	-250	13	-51	-56	-127	-321	-393	-275	-122	-97	**-148**	-361	**V**
Cr	-372	-88	0	-110	-8	5	-30	108	44	-47	42	4	-129	-82	-130	26	4	-22	**Cr**
Mn	-277	-286	-110	0	9	-19	-115	29	-25	-153	-138	-15	-188	-251	-254	-92	-139	-40	**Mn**
Fe	-418	-176	-8	9	0	-60	-97	65	-23	-2505	-484	41	-57	-116	-3468	-554	-25	11	**Fe**
Co	-386	-199	5	-19	-60	0	-21	54	-58	-178	-52	52	12	-10	-253	-84	-72	34	**Co**
Ni	-435	-250	-30	-115	-97	-21	0	-6	-256	-316	-100	40	2	-6	-746	-116	-116	32	**Ni**
Cu	-147	54	108	29	65	54	-6	0	-92	-29	83	108	-4	-126	28	129	83	141	**Cu**
Zn	-198	-51	44	-25	-23	-58	-256	-92	0	-160	-42	-150	-391	-571	-88	58	8	21	**Zn**
Nb	11	-56	-47	-153	-2505	-150	-316	-29	-160	0	-133	-249	-548	-435	-10	-76	**-202**	-276	**Nb**
Mo	-167	-127	42	-136	-484	-52	-100	83	-42	-133	0	-57	-248	-100	-193	-8	-2	-52	**Mo**
Ru	-763	-321	4	-15	41	52	40	108	-150	-249	-57	0	-8	47	-332	-66	-87	-16	**Ru**
Rh	-790	-393	-129	-188	-57	12	2	-4	-391	-548	-248	-8	0	37	-611	-273	-181	-8	**Rh**
Pd	-646	-275	-82	-251	-116	-10	-6	-126	-571	-435	-100	47	37	0	-480	-123	-57	67	**Pd**
Ta	31	-122	-130	-254	-3468	-253	-746	28	-88	-10	-193	-332	-611	-480	0	-114	**-226**	-330	**Ta**
W	-82	-97	26	-92	-554	-84	-116	129	58	-76	-8	-66	-273	-123	-114	0	7	-56	**W**
Re	**-189**	**-148**	4	-139	-25	-72	-116	83	8	**-202**	-2	-87	-181	-57	**-226**	7	0	-89	**Re**
Os	-713	-361	-22	-40	11	34	32	141	21	-276	-52	-16	-8	67	-330	-56	-89	0	**Os**
	Ti	**V**	**Cr**	**Mn**	**Fe**	**Co**	**Ni**	**Cu**	**Zn**	**Nb**	**Mo**	**Ru**	**Rh**	**Pd**	**Ta**	**W**	**Re**	**Os**	

Figure 1.2. Calculated enthalpy of formation for different binary alloys [6].

1.2.1.2 Entropy

Entropy is the thermodynamic property of a material that shows the amount of thermal energy per unit temperature in the system that cannot be used. In materials, entropy comes from two sources, i.e., static (configurational) and dynamic (vibrational) sources [7]. Configurational entropy (S_{conf}) is the entropy of a system that comes from the discrete position of particles, *i.e.*, the arrangement of the constituent elements in the lattices. The famous Boltzmann equation is shown as Equation 1.6. The form of the Boltzmann equation used for alloys is written as Equation 1.7.

$$\Delta S = k_B ln\ \Omega \qquad (1.6)$$

$$\Delta S = -R\Sigma C_i lnC_i \qquad (1.7)$$

where ΔS is the change of configurational entropy, R is the gas constant (8.314 $J \cdot mol^{-1} \cdot K^{-1}$), k_B is the Boltzmann constant (1.38×10^{-23} $J \cdot K^{-1}$), C_i is the concentration of components in the system, and Ω is the number of distinguishable configurations of the system. In nature, the process direction always occurs in such a way that increases the entropy of a system. For example, in the phase transition from liquid to solid, the increase in entropy level can be observed [8]. This excess entropy $S_{liquid} - S_{crystal}$ decreases if the supercooling temperature is reduced [9]. If the supercooled state at temperature is kept on decreasing, Kauzman temperature: T_K, the excess entropy becomes negative, *i.e.*, $S_{liquid} < S_{crystal}$, the metallic glass could be formed. This is called the Kauzman paradox effect as it is unusual that the Entropy of liquid can be lower than that of the solid. This topic is more important to the creation of metallic glass which is somewhat related to HEAs.

1.2.2 High Entropy Alloy

1.2.2.1 Alloy design

After the end of the stone age (3500 BC), humankind starts using metal as a material for tool making. At the beginning of the copper age, the metal had been used in a pure state. Then, the method of alloying to make the stronger tools were discovered. To date, the method of alloying has been improved based on the same basis of alloying since the copper age, *i.e.*, introducing a small amount of solute element in a major solvent element.

In 2004, the idea of using multi-component alloys was introduced by two scientists, Yeh and Cantor [10, 11]. The multicomponent alloys are later recognized as high entropy alloys (HEAs) on the basis of having high configurational entropy. The configurational entropy can be calculated by using Equations 1.6 and 1.7. When the number of constituent elements is 3 and 5, ΔS is $1.10R$ and $1.61R$. According to Richard's rule of entropy of metallic fusion, the approximate entropy of fusion of metals is roughly the value of R at its melting point [12]. Thus, when there are 3 constituent elements in the system, the ΔS is larger than the entropy of fusion. This is a preferred state for the system to form a disorder solid solution. In addition, there are other contributions from vibrational entropy, electronic entropy, and other quantum interactions that make the entropy of mixing even greater than the solely calculated configurational entropy. Nevertheless, this maximizing configurational entropy method for making the single-phase disordered solid solution is not effective. Some elements are more compatible than others, *e.g.*, Ni-Al or Ti-Al, which are likely to form intermetallic phases as they have low enthalpy of formation that dominates the free energy of those systems. Consequently, systems containing such elements will not have a single-phase solid solution but would contain ordered, constituent, or intermetallic phases [13].

Other factors affect the phase stability of HEAs. From the studies of Cantor and Otto [11, 13], it is depicted that the single-phase solid solution cannot be obtained by simply adding more elements. Thus, using only Gibb free energy criteria to predict the phase stability of the HEAs is not adequate. There are a number of research proposing empirical rules for predicting the phase of the HEAs [King -Chen]. From Humes-Rothery rules of mixing, the following criteria for making a solid solution are needed to be considered [14].

1. The atomic radius of the solute and solvent atoms must not be different by more than 15%.
2. The crystal structures of solute and solvent must be similar.
3. Complete solubility occurs when the solvent and solute have the same valency.
4. The solute and solvent should have similar electronegativity.

The pioneering research in HEA alloying design focused on narrowing down the combination of the HEA system based on atomic radii, crystal structures, the valency of elements, and electronegativity as dictated by Hume-Rothery rules [15]. The factors of atomic radii and enthalpy of mixing are used to predict the solid solution formation [16]. Atomic size different factor (δ) can be calculated from Equation 1.8 and the change in mixing enthalpy, ΔH_{mix}, between two elements, is expressed as Equation 1.9 [16].

$$\delta = \sqrt{\sum_{i=1}^{n} C_i \left(1 - \frac{r_i}{\bar{r}}\right)^2} \qquad (1.8)$$

$$\Delta H_{mix} = \sum_{i=1, i\neq j}^{n} \Omega_{ij} C_i C_j \text{ and } \Omega_{ij} = 4H_{mix}^{ij} \qquad (1.9)$$

The single-phase solid solution HEA forms when δ is in the range between 1 and 6 while ΔH_{mix} between -15 to 5 kJ/mol. The effect of electronegativity on the constituent elements is studied by Ji [17]. The electronegativity difference (Δe) in the HEA is calculated from Equation 1.10.

$$\Delta e = \sqrt{\sum_{i=1}^{n} C_i (e_i - \bar{e})^2} \qquad (1.10)$$

where e_i is Pauling electronegativity and $e_i = \sum_{i=1}^{n} C_i e_i$. The single-phase solid solution prefers a low Δe value (lower than 0.17 for AlCoCrFeNiTi HEA).

Valency of the constituting elements of the HEAs can also play a role in stabilizing certain crystal structures. The solid solution can be obtained when the valence electron concentration (VEC), as calculated from Equation 1.11. For AlCoCrCuFeNi systems, the system prefers the FCC phase when VEC is greater than 8.0 and the BCC phase when VEC is less than 6.8, and in between a dual-phase structural state (BCC + FCC) is predominant [18]. The valency state of the alloy affects the solid solution crystal structure as shown in these studies [18-22].

$$VEC = \sum_{i=1}^{n} C_i(VEC_i)\,. \qquad (1.11)$$

1.2.2.2 Properties of high entropy alloys

Unlike conventional alloys, there is no base metal or major alloying element that dominates the properties of the HEA. Conversely, the properties of HEAs are affected by the multi-component nature of the alloys. There are 4 core effects of HEAs namely high entropy effect, lattice distortion effect, sluggish diffusion effect, and cocktail effect.

High entropy effect

As discussed in the previous section, HEAs have high mixing entropy, which consists of configurational entropy, vibrational entropy, and electronic entropy. This high mixing entropy dominates the phase stability in Gibbs free energy equation. Hence, HEAs are found to stabilize the disordered solid solution phase. This evidence can be portrayed via the Gibbs phase rule as written in Equation 1.12.

$$F = C - P + 2 \qquad (1.12)$$

when F is the degrees of freedom, C is the number of components in the system, and P is the possible number of phases in the system. In the pure substance case with constant temperature and pressure, if $F = 0$ and $C = 1$, the number of possible phases present in the system (P) is 3. In the case of HEAs with 5 principal elements, let $F = 0$ and $C = 5$, possible phases can be 7. However, HEAs show that they have fewer phases than the calculated, which proves that high configurational entropy helps suppress the multiple phase formation. This high entropy effect is the design fundamental of the HEAs. Nevertheless, this high entropy effect is found to have a limit. There are only a handful of HEAs that exhibit stable single-phase solid solution, *e.g.,* VNbMoTaW, $TiV_{0.3}ZrNbMo_{0.3}$, CoCrFeMnNi,

$Al_{0\text{-}0.15}CoCrFeNi$ [11, 22-25]. Other HEA systems are susceptible to phase instability. The $Al_{0.2\text{-}1.8}CoCrFeNi$ is found to have Ni-Al precipitates and sigma phase when aged at an intermediate temperature [24]. It can be concluded from such observations that the HEAs are prone to be unstable as a single-phase solid solution as more elements are introduced to the system. This is because of the influences of the mixing enthalpy effect and physical miscibility. Even though some HEA systems cannot avoid having second phases, the entropy effect still plays a significant role in keeping the number of phases at its possible lowest number than that the system can possibly have when calculated using the Gibbs phase rule.

Severe lattice distortion effect

By heavily alloying, the lattice sites of HEAs are occupied randomly by different element atoms. Due to the difference in the atomic radii among different atomic species of the nearest neighbor, the lattice of HEAs becomes distorted. The schematic of lattice distortion in the HEAs is shown in Figure 1.3.

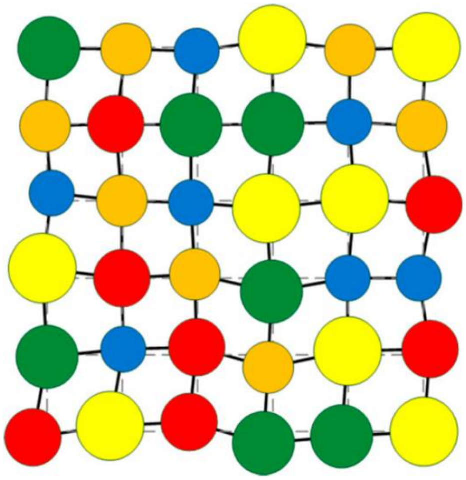

Figure 1.3. Schematic of the lattice structure in a HEA with five alloying elements [26].

In the classical theory of mechanical metallurgy, the yield strength is the stress which can move dislocations through the lattice plane. This distortion of the lattice elastically interacts with the moving dislocations and increasing the strength by solid solution strengthening. In structural materials, the severe lattice distortion effect improves the mechanical properties of the HEAs to overcome the strength-ductility trade-off dilemma [27]. Lattice distortion is not only strengthened the HEAs, but it also softens the physical properties. One example is the XRD peaks reducing in intensity are observed in several HEAs [28-30]. This occurrence of XRD intensity reducing was not to be construed as the result of the atomic size difference but the lattice strain around the sites [31].

Sluggish diffusion effect

One of the interesting characteristics of HEAs is related to diffusion. Designing an alloy with low solid diffusivity benefits other properties of the alloy, such as. high temperature strength, high temperature creep, and corrosion resistance. The sluggish diffusion in HEAs is the result of the randomness in the arrangement of different elements in the lattice. The localized energy fluctuation serves as an atomic trap site. The schematic representation of the phenomenon is shown in Figure 1.4 [28]. Pioneering work demonstrating this sluggish diffusion effect in HEA was done by Tsai *et al.* on *CoCrFeMnNi* HEA

[32]. The work shows that the normalized diffusion activation energy (Q/T_m), where Q is the activation energy and T_m is the melting point, of the HEA is higher compared to that of its constituent elements. A study by Laplance [33] shows that the lattice diffusivity of Cr atoms in HEA is slower than that of Cr in stainless steel and pure Ni at the same homologous temperature (T_m/T). However, lattice diffusivity is enhanced by other diffusion mechanisms, *i.e.*, pipe diffusion and grain boundary diffusion. Conversely, there are many studies on the sluggish diffusion effect of HEAs that show the diffusion effect in HEAs is not slower than that of the conventional alloys [34, 35].

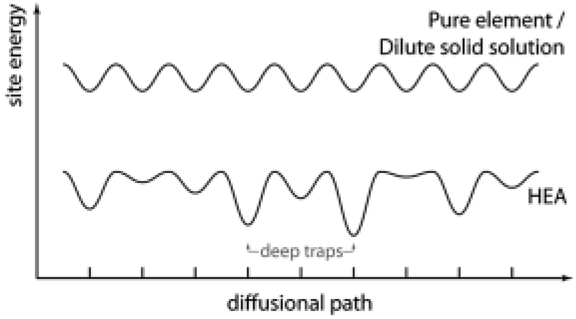

Figure 1.4. Schematic representation of the localized energy trap in the HEA [28].

Cocktail effect

The cocktail effect in the HEAs is rather abstract [26][36]. The term 'cocktail' refers to the way that multiple metals are mixed like a cocktail to tailor new alloy with prominent properties [37]. It can be described as a HEA characteristic that arises from the complex atomic interactions among the alloying elements that can bring unprecedented properties in conventional alloys, compared to the conventional metallic alloys, in the HEAs. These HEAs properties can be tailored by using the cocktail effect including but not limiting to promoting metastable crystalline microstructure, precipitating beneficial intermetallic phase [38].

1.2.3 Development of Face Center Cubic High Entropy Alloys

Even though HEAs have not been commercially used to the best knowledge of this author, there are promising applications of HEAs. The unique properties of the HEAs allow them to be used as wear-resistant and corrosion-resistant materials [39-45], hydrogen storage [46], and diffusion barrier [47, 48]. There are 3 crystal structures found in HEAs, *i.e.*, body-centered cubic (BCC), face-centered cubic (FCC), and hexagonal close packed (HCP). In general, BCC HEAs are made by using refractory metals, *e.g.*, W, Mo, V, Nb, etc. while the FCC HEAs are derived from the transition elements, *e.g.*, Fe, Co, Cr, Mn, Ni, Cu, etc. The HCP-based HEAs are rather scarce [49]. Some of the HCP based HEAs are GdHoLaTbY, CoFeReRu, DyGdHoTbY, DyGdLuTbY and DyGdLuTbTm. The BCC-based HEAs are made for high strength and elevated temperature applications as they usually show higher yield strength compared to the FCC-based alloys. Some examples of the BCC-based HEAs are MoNbTaW, and MoNbTaVW [50]. The FCC-based HEAs are known to have better ductility than BCC-based HEAs and are less anisotropic compared to HCP-based alloys. These FCC-based alloys show a good combination between strength and ductility because of the close-packed crystal structure and the inherent 12 slip systems. The FCC based HEAs, AlCoCrCuFeNi, AlCoCrFeNi, and AlCoCrFeMnNi are the most studied HEA systems [51-61]. Later, the development of FCC-based HEAs is derived from these systems by using CoCrFeNi as a base composition because the composition is thermally stable and shows exceptional mechanical properties at intermediate and cryogenic temperatures [62, 63].

Single-phase solid solution HEAs sometimes have relatively low strength which does not meet the desired application requirement. Hence, the non-equiatomic HEAs are made for tailoring the properties of the HEAs to match the needs. Even though the HEAs design philosophy is based on maximizing configurational entropy to have single-phase solid solution alloys, most of the time HEAs exhibit intermetallic phases and second-phase precipitation. By careful alloy design, the non-equiatomic HEAs involve phase instability leading to useful intermetallic precipitation and subsequent phase transformations [38, 64]. Non-equiatomic HEAs sometimes satisfy the prospect of using HEAs in practice. One of the strategies of designing non-equiatomic HEAs is to adjust the system composition for tuning the stacking fault energy or to create a metastable phase in the systems. These HEAs undergo phase transformation upon deformation to help maintain the ductility of the alloys while increasing their strength [64, 65]. These metastable HEAs show martensitic transformation during the deformation in the same fashion with other advanced materials such as high manganese steel [66-69].

Al_xCoCrFeNi High Entropy Alloy

The Al_xCoCrFeNi HEAs have been developed based on the FCC-based CoCrFeNi HEA. Depending on the amount of Al in the alloy, this HEA exhibits phase change over the range of x as shown in the study by Kao *et al.* [61]. When $0.5 \leq x \leq 0.75$, the alloy exhibits its duplex nature by having both BCC and FCC phases. When $x \leq 0.375$, only FCC phase is present. Besides the BCC phase dominates the microstructure at $0.875 \leq x$. The ThermoCalC calculated phase diagram of the alloy can be found elsewhere in the work by Zhang et al. [71, 72]. This HEA composition is reported for having deformation twinning during deformation at both room and cryogenic temperatures [73].

A study on this HEA microstructure and mechanical behavior was done by Yang *et al.* with $x = 0.1 – 1.75$ [74]. The phases shown in the alloy are FCC, A2-BCC, and B2-BCC phases. Al stabilizes B2 phase. The BCC phase in $Al_{0.6}$CoCrFeNi exhibits martensitic transformation (BCC to orthorhombic) as confirmed by the study of Ma *et al.* [75]. This finding implies the benefit of having dual-phase nature of the alloy to the mechanical properties as a martensitic transformation during loading of the materials improves its toughness. Wang *et al.* found that the response to thermal aging of this HEA is different depending on the value of x [54]. The study also reports that the HEA has better softening resistance when compared to conventional alloys, T-800 and In718 at high homologous temperatures (above 0.5 Tm).

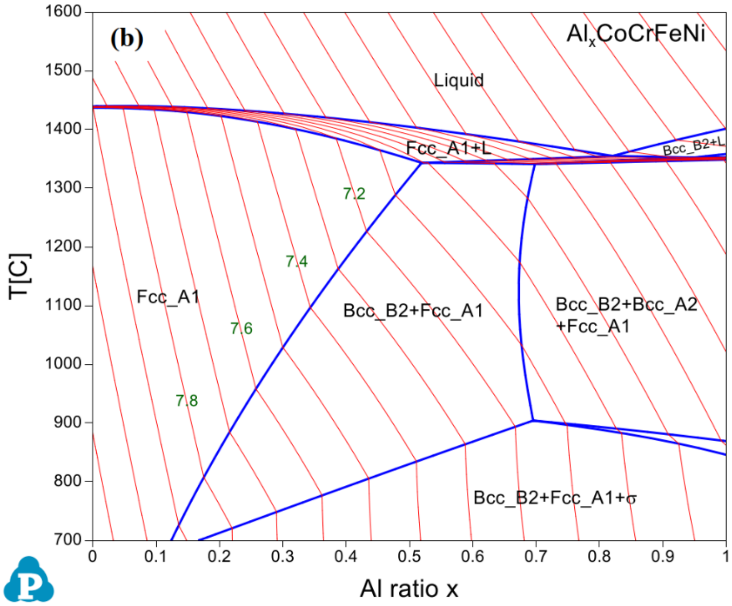

Figure 1.5. Calculated phase diagram of $Al_xCoCrFeNi$ HEA [24].

$Fe_{42}Co_{10}Cr_{15}Mn_{28}$ non-Equiatomic High Entropy Alloy

This HEA system is a non-equiatomic HEA that is designed for gaining exceptional mechanical properties. In conventional alloys, to improve the strength of an alloy, the ductility is sacrificed [76]. This problem is called the strength-ductility trade-off. By producing the HEA that shows the ability to undergo deformation twinning or deformation-induced martensitic transformation, this strength-ductility dilemma problem is solved [77]. This HEA is designed to have low stacking fault energy, which influences the deformation mechanisms of the alloy [78], to obtain such a property. Li *et al.* proposed the idea of changing HEA composition from equiatomic alloys to non-equiatomic to adjust the stacking fault energy of the HEA. This results in the HEA with $Fe_{42}Co_{10}Cr_{15}Mn_{28}$ composition [64]. Later this HEA is modified by adding Si, Cu, Al to combine twinning induced plasticity and transformation induced plasticity effect. That results in HEA with good ductility (50% elongation to fracture) with high strength (1 GPa) [79, 80-83]

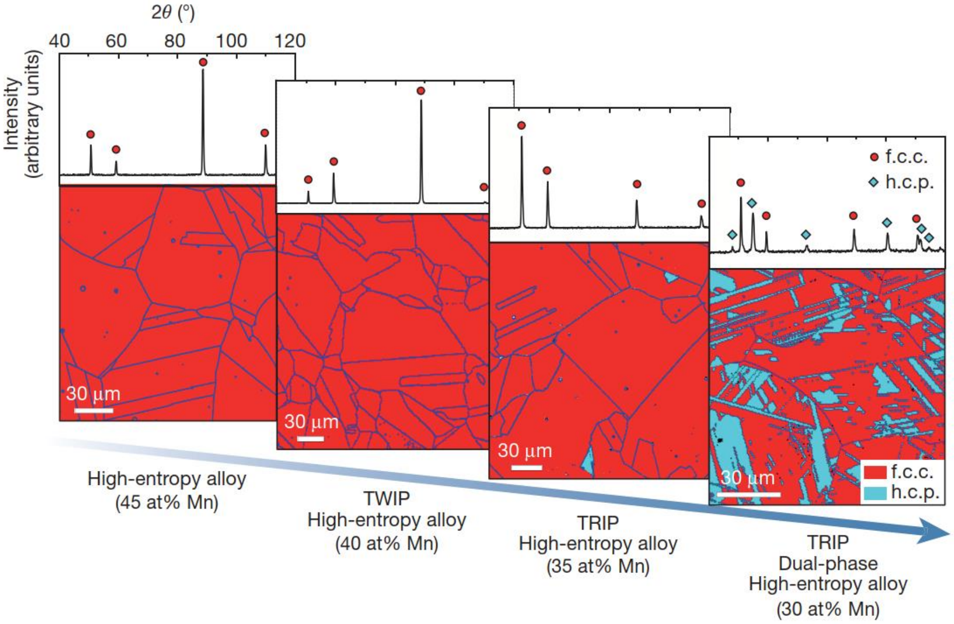

Figure 1.6. Effect of Mn addition on the deformation mechanisms of $Fe_{80-x}Co_{10}Cr_{10}Mn_x$.

1.2.3. Strength of FCC metals

The alloys with FCC crystal structure find their place in a wide range of applications because of their good combination between strength and toughness. The yield strength of metallic materials is made up of 5 individual contributions as the following equation 1.13.

$$\sigma_y = \sigma_0 + \sigma_{SS} + \sigma_{WH} + \sigma_{PPT} + \sigma_{H-P} \qquad (1.13)$$

where σ_0 is Peierls stress, σ_{SS} is solid solution strengthening, σ_{WH} is work hardening, σ_{PPT} is precipitation strengthening, σ_{H-P} is Hall-Petch strengthening. Peierls stress or lattice friction stress is the resistance of the lattice against shearing 2 adjacent lattice planes. The relationship can be expressed as equation 1.14.

$$\sigma_0 = \frac{2MG}{(1-\nu)\cdot EXP(-2\pi w/b)} \qquad (1.14)$$

Where M is a Taylor factor, G is shear modulus, ν is the Poisson ratio, and w and b are dislocation core width and Burgers vector magnitude. Metals undergo plastic deformation by moving dislocation through the lattice plane. In the case of pure metals or diluted alloys, this lattice plane is considered to have equal resistance from each lattice. In HEAs, the lattices are occupied with different atoms that make the lattice plane distorted. When a dislocation moves through this distorted potential field it moves through the field in a viscous manner. Zhao and Neil's study shows that the Peierls stress increases when the lattice is distorted. Comparing the diluted FCC alloys with more than 3 multicomponent alloys, the Peierls stress in Multicomponent alloys are greater than that of diluted alloys by an order of magnitude [84, 85]. The energy of dislocation (E_d) can be estimated by using equation 1.15.

$$E_d = G\sum_{i=1}^{n} b_i^2 l_i \qquad (1.15)$$

Where G is shear modulus, b is Burgers vector, and l is dislocation length. To predict the local contribution to the Peierls stress, localize interaction energy is needed. However, to the best of the author's knowledge, there is no study on this matter has been done. Thus, the exact value of E_d is yet known. But the assumption that the E_d in HEAs is higher than conventional alloy can be implied from the fact that the lattice distortion (dilated lattice) is higher in HEA. Shrinking dislocation core effect is also proposed by the same authors as the σ_0 is proportional to the $\frac{w}{b}$ value as shown in equation (1.14).

Solid solution strengthening is the interaction between dislocation and solute elements. La Rosa *et al.* treats the lattice site as random with the presence of short-range order, *i.e.*, Varvenne, Luque, and Curtin model [86]. Thus, the intrinsic strength of the HEAs comes from the contribution of stochastic potential in the crystal structure and the presence of the short-range order phase which forces dislocation to bow out those high energy sites [87. Like the formula for calculating the solid solution strengthening of the metals, the contributions to the strength from each elements are proposed empirically. The following model is proposed by Carabollo [88] for concentrated solid solution strengthening.

$$\sigma_{ss} = \sum[A_i^{3/2}\, C_i]^{2/3} \qquad (1.16)$$

Where A_i and C_i are contribution and concentration from the ith element in the system.

In conventional alloy, the precipitation strengthening is the interaction between dislocation and second phase precipitation in the alloy. The second phase behaves as the pinning point against the dislocation line that creates tension deterring the mobility of dislocation. Single-phase solid solution HEAs suffer from having low yield strength. Hence, there are attempts to increase the strength of the HEAs by using precipitation strengthening coming from short-range order phase or second phase precipitation [89-93]. There are two strengthening mechanisms in precipitation hardening alloy, namely, dislocation shearing and dislocation bowing (Orowan strengthening). The precipitation strengthening in CoCrFeNi HEAs is found to be particle shearing type [94]. There are several contributions namely particle/matrix coherency ($\sigma_{Coherency}$), modulus mismatch ($\sigma_{Mismatch}$), and atomic ordering ($\sigma_{Ordering}$). These contributions are described in the equation 1.17.1-1.17.3 [94].

$$\sigma_{Coherency} = M \cdot 0.0055(\Delta G)^{1.5}\left(\frac{2f}{G}\right)^{0.5}\left(\frac{r}{b}\right)^{1.5m-1} \qquad (1.17.1)$$

$$\sigma_{Mismatch} = M \cdot \alpha_{\varepsilon}(G \cdot \varepsilon)^{1.5}\left(\frac{rf}{0.5Gb}\right)^{0.5} \qquad (1.17.2)$$

$$\sigma_{Ordering} = M \cdot 0.81(\frac{\gamma_{APB}}{2b})^{1.5}\left(\frac{3\pi f}{8}\right)^{0.5} \qquad (1.17.3)$$

Where α_{ε} = 2.6 for FCC structure, m = 0.85, $\varepsilon \approx 2/3 \cdot (\Delta a/a)$ is the constrained lattice parameter mismatch, f is the volume fraction of the precipitates, ΔG is the shear modulus mismatch between precipitates and matrix, and γ_{APB} is the anti-phase boundary energy of the precipitates.

Hall-Petch strengthening is a strengthening of an alloy through the effect of grain boundary blockage on the dislocation movement and causes dislocation piled-up. The behavior of HEAs is similar to that of the conventional alloys in that the strength of the alloys increases inverse proportionally to the grain size [14, 52, 66, 95, 96]. The classic Hall-Petch relationship can be written as equation 1.18.

$$\sigma_{H-P} = Kd^{0.5} \qquad (1.18)$$

where K is materials coefficient or the dislocation unpinning parameter for Hall-Petch strengthening and d is grain size. The value of K for different HEAs are listed in Table 1.1.

Table 1.1. Reported K value for Hall-Petch strengthening in some HEAs

HEA	K (MPa·μm$^{-0.5}$)	Reference
CoCrFeNiMn	226	[96]
$Al_{0.3}$CoCrFeNi	227	[52]
CoFeNi	131	[66]
CoCrFeNi	165	[66]
CoCrNi	654	[95]

1.2.4. Plasticity of FCC HEAs

Plasticity is the ability that a material undergoes permanent deformation. In metals, the plasticity arises from the shear movement of the slip plane over the other. More practically, the plasticity is contributed from the movement of the dislocation on the slip plane. A typical engineering stress-strain ($\sigma - \varepsilon$)curve is shown in Figure 1.7. From the figure, the elastic limit of metals star from ε = 0 to ε = 0.2%. At this part, the slope of the curve is Young's modulus (E), where $E = \frac{d\sigma}{d\varepsilon}$.

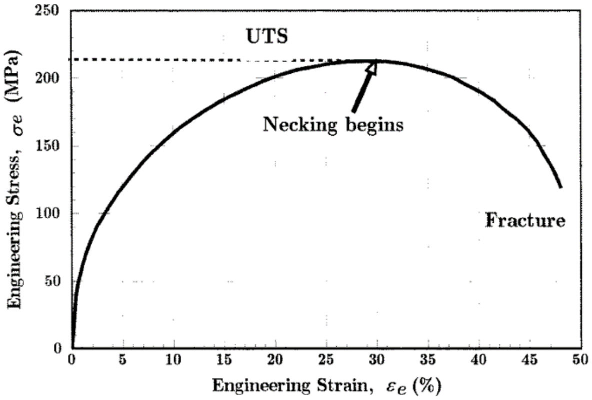

Figure 1.7. Engineering Stress-strain curve of metal.

From ε = 0.2% onward to the apex of the curve, the metals deform plastically. During plastic deformation, dislocation is moving following the slip system of crystal structures. In FCC metals, the slip systems of perfect dislocation glide are in {111} planes and in <110> directions. Perfect dislocation Burgers is $b = \frac{a}{2}\langle 110\rangle$. Sometimes, for the energy favorable, a perfect dislocation dissociates into 2 Shockley partials as Equation (1.19). The lattice translation of this perfect dislocation can be visualized by using Thomson tetrahedron or using a hardball model of stacking. The perfect dislocation is that when the blue atom movie and sit on the next blue lattice site. A partial dislocation is when an atom on the blue site moves diagonally to the C stacking and another.

$$\frac{a}{2}\langle 110\rangle \rightarrow \frac{a}{6}\langle 121\rangle + \frac{a}{6}\langle 21\bar{1}\rangle \qquad (1.19)$$

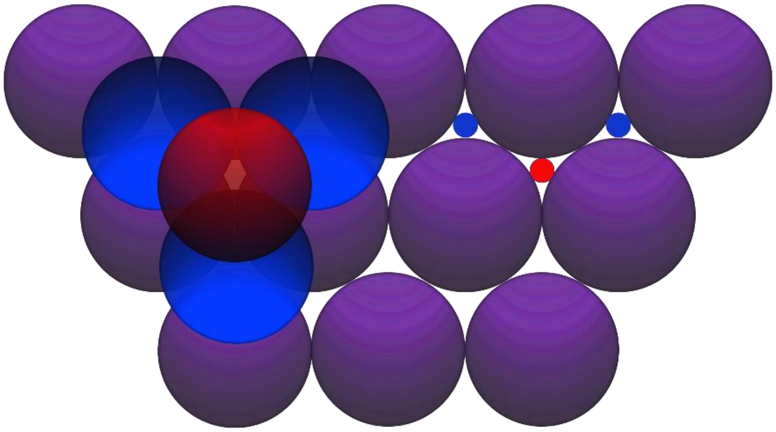

Figure 1.8. Hardball model of stacking in FCC crystal. When we down at the [111] plane of FCC crystal. The purple ball is stacking A. Blue layer is stacking B and Red is stacking C. The perfect Burgers vector and two partial dislocations are denoted as the arrow in the figures.

The work hardening behavior during the plasticity of metals is the phenomenon that occurs because of the increase in dislocation density. Several mathematical models are used to explain this work hardening behavior, namely, perfect elastic, linear work hardening, and power law work hardening [97].

$\sigma = K\varepsilon_{plastic}^{n}$ (Hollomon's strain hardening) (1.20.1)

$\sigma = \sigma_y + A\varepsilon_{plastic}$ (Linear strain hardening) (1.20.2)

$\sigma = K(\varepsilon_{plastic} + \varepsilon_0)^n$ (Swift law) (1.20.3) [98]

Where σ is stress, n is strain hardening exponent, K is strength coefficient, and A is a plastic modulus of a material.

Stacking faults energy is the indicator that measures the likelihood that the stacking sequence of the crystal remaining the same after shear stress is applied. It strongly controls the mechanical behaviors and plasticity of the FCC metals [99]. In steels, the threshold value of stacking faults energy for dislocation glide is greater than 20 mJ/m^2. Transformation-induced plasticity (TRIP) occurs at SFE between 10-40 mJ/m^2 and transformation-induced plasticity (TWIP) happened at SFE lower than 20 mJ/m^2 [100].

In the advanced metal alloys, it is often time refer the alloys that undergo TWIP as TRIP under the deformation as TWIP or TWIP alloys. These TWIP and TRIP phase transformation modes occur in the same manner, *i.e.*, the change in stacking sequence as shown in Figure 1.9. When low stacking faults metals become sheared the original stacking sequence starts to change.

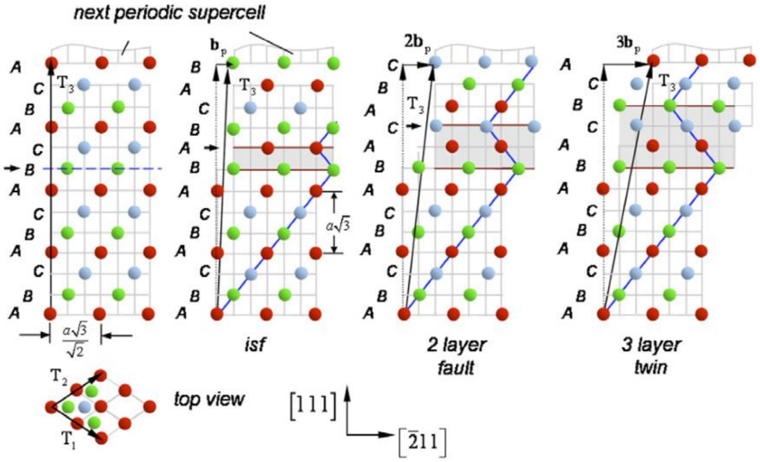

Figure 1.9. Change in stacking sequence when a low SFE metal is sheared [101]

1.2.5 Micromechanical properties

Micromechanical properties are the mechanical properties on a small scale (less than 100 μm). The testing techniques provide an advantage in obtaining individual phases' mechanical behaviors and learning behaviors of the specimen under different shapes, crystal orientations, and sizes [102-104]. This helps to understand the discrete properties and, hence, grasping the bulk behavior of metal. The methods for testing such properties are micropillar compression, nanoindentation, Vickers hardness testing.

One of the novel micromechanical property characterizations is the micropillar compression testing technique. This technique involves using fabricating the materials into a small pillar and then compressing with a hard punch, equipped in a scanning electron microscope. However, the interpretation of the micromechanical properties is slightly different from that of the bulk mechanical properties because of the inherently different testing specimen design. The micropillar compression testing schematic is shown in Figure 1.10. The micropillar typically locates on a substrate having the same material. Hence, when the pillar is compressed, it presses the substrate underneath and against the punch, too. As a result, the strain (ε) measured in the micropillar compression is the sum of strain from the punch, the pillar, and the substrates which can be expressed as in equation 1.21.

$$\chi_{total} = \chi_{substrate} + \chi_{indenter} + \chi_{pillar} \qquad (1.21)$$

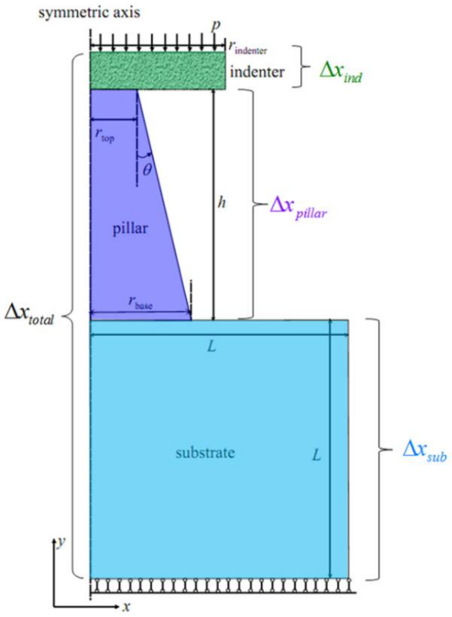

Figure 1.10. Schematic of axisymmetric half-space of micropillar compression [105].

To calculate the substrate displacement, Sneddon [106] proposed the analytic solution for solving the displacement caused by pressing an axisymmetric punch on the substrate, *i.e.*, the Boussinesq problem. The compliance of the displacement can be written as equation 1.22.

$$C_{Sneddon} = \frac{(1-\upsilon^2)\sqrt{\pi}}{2E\sqrt{A_p}} \qquad (1.22)$$

Where E is the elastic modulus A_p is the pillar crossectional area, and υ is the Poisson's ratio. From the micropillar compression testing configuration, the pillar is considered a punch pressing into the indenter and substrate. The displacement of those substrates, i.e., indenter and the pillar's substrate is assimilated as a series of connecting springs.

$$\chi_{indenter} = C_{indenter} f \text{ and } \chi_{substrate} = C_{substrate} f \qquad (1.23)$$

Where $f = \pi r_i^2 p$ and p is the load applied to the pillar during the compression test. The pillar displacement is then written as follows.

$$\chi_{pillar} = \chi_{total} - \frac{(1-\upsilon_{substrate}^2)\cdot f}{2E_{substrate}\cdot r_{base}} - \frac{(1-\upsilon_{indenter}^2)\cdot f}{2E_{indenter}\cdot r_{top}} \qquad (1.24)$$

The engineering strain and stress can be calculated from the following equations.

$$\varepsilon_{pillar} = \frac{\chi_{pillar}}{h} \qquad (1.25.1)$$

$$\sigma = \frac{r_{indenter}^2}{r_{pillar}^2} p \qquad (1.25.2)$$

This stress calculation is less accurate if the pillar is tapered. This error becomes greater when the aspect ratio of the pillar is larger coupling and coupling with tapered effect.

1.2.6 Solid-state welding of HEA

One of the important properties of a metal is its weldability. Sometimes parts or tools cannot be made single piece. Thus, a joining technique is needed. Welding is one of the techniques that has been used widely in industrial works because the production of the parts cannot make the net shape parts. During welding, metals are exposed to different thermal histories in which alter both the microstructure and the mechanical properties. The fusion welding techniques used until today are tungsten gas welding (TIG), metal gas welding (MIG), plasma welding, laser welding, and electron beam welding. These fusion welding techniques produced different affected zone as shown in Figure 1.11. This width of the heat-affected area varies based on the heat input of the welding techniques [107].

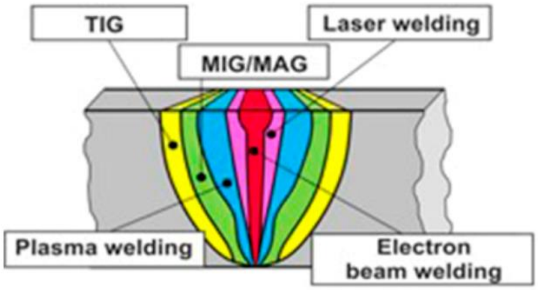

Figure 1.11. The affected area on the welded piece in different fusion welding techniques.

Exploring the weldability of the HEAs eventually pushes the alloy into practical usage. There is welding research being done on HEAs. The welding technique that is used is arc welding (AW), laser welding [108], electron beam welding [109], and friction stir welding (FSW) [80-82]. First two techniques reduced the hardness, strength, and ductility of the HEAs but when the mechanical properties are improved when the welding is done by using FSW technique. The wide range of elements in HEAs sometimes makes the welding of HEAs rather difficult. Some HEAs contain elements that are susceptible to the thermal effect. Manganese, notoriously oxidized at a very high rate, will deplete after the welding [110]. HEA containing Co needs to be taking care not to have Cu contamination since the weld cracking can be formed [111, 112]].

Friction stir welding (FSW) is a solid-state joining technique, wherein a non-consumable tool is plunged into a material and traversed along with the joint interface as shown in Figure 1.12. The heat is mainly generated from the friction between the rotating tool and the material surface, and to a less extent, from the adiabatic heat generated by the high strain-rate adiabatic plastic deformation during the process [113]. FSW has also been developed as a powerful thermomechanical processing technique and a host of friction stir based applications have been termed friction stir processing (FSP). The materials under FSP dynamically recrystallize by the effects of heat and strain [114]. This results in the FSPed material having, equiaxed grain structure.

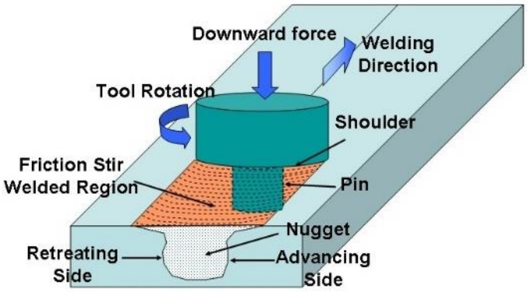

Figure 1.12. Schematic of friction stir welding/processing process [115].

FSW/P technique has advantages over fusion welding in that the welded specimens do not undergo a melt-solidification cycle. Thus, some microstructural features such as precipitates and grain structure can be preserved [108]. Since FSW/P is a thermomechanical process, it can be used as a method for microstructural modification in some metal alloys including HEAs [80-82][116].

Another solid-state welding technique is pressure resistance welding (PRW). This welding technique involves passing the electric current through welding coupons pressed together. The heat comes from the change in resistance along the current path, *i.e.*, the coupon contact. Thus, the PRW process is a Thermo-electro-mechanical process. To the best of the author's knowledge, there is no research has been done on applying the PRW technique on HEAs. However, there are some works on using a similar technique for cladding the HEA on different alloys by using the resistance seam welding method [117].

References

[1] Porter, D. A., & Easterling, K. E. (1992). Phase transformations in metals and alloys (2nd ed.). Chapman & Hall.1.

[2] Miedema, A. R. (1973). The electronegativity parameter for transition metals: Heat of formation and charge transfer in alloys. *Journal of The Less-Common Metals*. https://doi.org/10.1016/0022-5088(73)90078-7

[3] Zhang, B., Liao, S., Shu, X., Xie, H., & Yuan, X. (2013). Theoretical calculation of the mixing enthalpies of 21 IIIB-IVB, IIIB-VB and IVB-VB binary alloy systems. *Physics of Metals and Metallography*. https://doi.org/10.1134/S0031918X13060045

[4] Debski, A., Debski, R., & Gasior, W. (2015). New Features of Entall Database: Comparison of Experimental and Model Formation Enthalpies/ Nowe Funkcje Bazy Danych Entall: Porównanie Doświadczalnych I Modelowych Entalpii Tworzenia. *Archives of Metallurgy and Materials*. https://doi.org/10.2478/amm-2014-0228

[5] Takeuchi, A., & Inoue, A. (2005). Classification of bulk metallic glasses by atomic size difference, heat of mixing and period of constituent elements and its application to characterization of the main alloying element. *Materials Transactions*. https://doi.org/10.2320/matertrans.46.2817

[6] Troparevsky, M. C., Morris, J. R., Kent, P. R. C., Lupini, A. R., & Stocks, G. M. (2015). Criteria for predicting the formation of single-phase high-entropy alloys. *Physical Review X*. https://doi.org/10.1103/PhysRevX.5.011041

[7] Fultz, B. (2014). Phase transitions in materials. In *Phase Transitions in Materials*. pp. 164. https://doi.org/10.1017/CBO9781107589865

[8] Tekuchev, V. V., Kalinkin, D. P., & Ivanova, I. V. (2018). Calculating the Entropy of Solid and Liquid Metals, Based on Acoustic Data. *Russian Journal of Physical Chemistry A*. https://doi.org/10.1134/S003602441805031X

[9] Kauzmann, W. (1948). The Nature of the Glassy State and the Behavior of Liquids at Low Temperatures. *Chemical Reviews*. https://doi.org/10.1021/cr60135a002

[10] Yeh, J. W. (2015). Physical Metallurgy of High-Entropy Alloys. *JOM*. https://doi.org/10.1007/s11837-015-1583-5

[11] Cantor, B., Chang, I. T. H., Knight, P., & Vincent, A. J. B. (2004). Microstructural development in equiatomic multicomponent alloys. *Materials Science and Engineering A*. https://doi.org/10.1016/j.msea.2003.10.257

[12] Tiwari, G. P. (1978). Modification of richard's rule and correlation between entropy of fusion and allotropic behaviour. *Metal Science*. https://doi.org/10.1179/msc.1978.12.7.317

[13] Otto, F., Yang, Y., Bei, H., & George, E. P. (2013). Relative effects of enthalpy and entropy on the phase stability of equiatomic high-entropy alloys. *Acta Materialia*. https://doi.org/10.1016/j.actamat.2013.01.042

[14] Dieter, G. E., & Bacon, D. J. (1986). Mechanical metallurgy (Vol. 3). New York: McGraw-hill.

[15] King, D. J. M., Middleburgh, S. C., McGregor, A. G., & Cortie, M. B. (2016). Predicting the formation and stability of single phase high-entropy alloys. *Acta Materialia*, *104*, 172–179. https://doi.org/10.1016/j.actamat.2015.11.040

[16] Zhang, Y., Zhou, Y. J., Lin, J. P., Chen, G. L., & Liaw, P. K. (2008). Solid-solution phase formation rules for multi-component alloys. *Advanced Engineering Materials*. https://doi.org/10.1002/adem.200700240

[17] Ji, X. (2015). Relative effect of electronegativity on formation of high entropy alloys. *International Journal of Cast Metals Research*, *28*(4), 229–233. https://doi.org/10.1179/1743133615Y.0000000004

[18] Guo, S., Ng, C., Lu, J., & Liu, C. T. (2011). Effect of valence electron concentration on stability of fcc or bcc phase in high entropy alloys. *Journal of Applied Physics*. https://doi.org/10.1063/1.3587228

[19] Ke, G. Y., Chen, S. K., Hsu, T., & Yeh, J. W. (2006). FCC and BCC equivalents in as-cast solid solutions of AlxCo yCrzCu0.5FevNiw high-entropy alloys. *Annales de Chimie: Science Des Materiaux*. https://doi.org/10.3166/acsm.31.669-684

[20] Tung, C. C., Yeh, J. W., Shun, T. tsung, Chen, S. K., Huang, Y. S., & Chen, H. C. (2007). On the elemental effect of AlCoCrCuFeNi high-entropy alloy system. *Materials Letters*. https://doi.org/10.1016/j.matlet.2006.03.140

[21] Chen, R., Qin, G., Zheng, H., Wang, L., Su, Y., Chiu, Y. L., Ding, H., Guo, J., & Fu, H. (2018). Composition design of high entropy alloys using the valence electron concentration to balance strength and ductility. *Acta Materialia*, *144*, 129–137. https://doi.org/10.1016/j.actamat.2017.10.058

[22] Senkov, O. N., Wilks, G. B., Miracle, D. B., Chuang, C. P., & Liaw, P. K. (2010). Refractory high-entropy alloys. *Intermetallics*. https://doi.org/10.1016/j.intermet.2010.05.014

[23] Wu, Y. D., Cai, Y. H., Chen, X. H., Wang, T., Si, J. J., Wang, L., … Hui, X. D. (2015). Phase composition and solid solution strengthening effect in TiZrNbMoV high-entropy alloys. *Materials and Design*. https://doi.org/10.1016/j.matdes.2015.06.072

[24] Zhang, C., Zhang, F., Diao, H., Gao, M. C., Tang, Z., Poplawsky, J. D., & Liaw, P. K. (2016). Understanding phase stability of Al-Co-Cr-Fe-Ni high entropy alloys. *Materials & Design*, 109, 425-433.

[25] Zhang, C., Zhang, F., Chen, S., & Cao, W. (2012). Computational thermodynamics aided high-entropy alloy design. *JOM*. https://doi.org/10.1007/s11837-012-0365-6

[26] Pickering, E. J., & Jones, N. G. (2016). High-entropy alloys: a critical assessment of their founding principles and future prospects. *International Materials Reviews*. https://doi.org/10.1080/09506608.2016.1180020

[27] Sohn, S. S., Kwiatkowski da Silva, A., Ikeda, Y., Körmann, F., Lu, W., Choi, W. S., … Raabe, D. (2019). Ultrastrong Medium-Entropy Single-Phase Alloys Designed via Severe Lattice Distortion. *Advanced Materials*. https://doi.org/10.1002/adma.201807142

[28] Yeh, J. W. (2015). Physical Metallurgy of High-Entropy Alloys. In *JOM*. https://doi.org/10.1007/s11837-015-1583-5

[29] Tsai, C. W., Chen, Y. L., Tsai, M. H., Yeh, J. W., Shun, T. T., & Chen, S. K. (2009). Deformation and annealing behaviors of high-entropy alloy Al0.5CoCrCuFeNi. *Journal of Alloys and Compounds*. https://doi.org/10.1016/j.jallcom.2009.06.182

[30] Chou, H. P., Chang, Y. S., Chen, S. K., & Yeh, J. W. (2009). Microstructure, thermophysical and electrical properties in AlxCoCrFeNi ($0 \leq x \leq 2$) high-entropy alloys. *Materials Science and Engineering B: Solid-State Materials for Advanced Technology*. https://doi.org/10.1016/j.mseb.2009.05.024

[31] Butler, B. D., Withers, R. L., & Welberry, T. R. (1992). Diffuse absences due to the atomic size effect. *Acta Crystallographica Section A*. https://doi.org/10.1107/S0108767392003131

[32] Tsai, K. Y., Tsai, M. H., & Yeh, J. W. (2013). Sluggish diffusion in Co-Cr-Fe-Mn-Ni high-entropy alloys. *Acta Materialia*. https://doi.org/10.1016/j.actamat.2013.04.058

[33] Laplanche, G. (2020). Growth kinetics of σ-phase precipitates and underlying diffusion processes in CrMnFeCoNi high-entropy alloys. *Acta Materialia*. https://doi.org/10.1016/j.actamat.2020.08.023

[34] Mehta, A., & Sohn, Y. (2020). High Entropy and Sluggish Diffusion “Core” Effects in Senary FCC Al–Co–Cr–Fe–Ni–Mn Alloys. *ACS Combinatorial Science*, *22*(12), 757–767. https://doi.org/10.1021/ACSCOMBSCI.0C00096

[35] Kucza, W., Dąbrowa, J., Cieślak, G., Berent, K., Kulik, T., & Danielewski, M. (2018). Studies of “sluggish diffusion” effect in Co-Cr-Fe-Mn-Ni, Co-Cr-Fe-Ni and Co-Fe-Mn-Ni high entropy alloys; determination of tracer diffusivities by combinatorial approach. *Journal of Alloys and Compounds*, *731*, 920–928. https://doi.org/10.1016/J.JALLCOM.2017.10.108

[36] Miracle, D. B., & Senkov, O. N. (2017). A critical review of high entropy alloys and related concepts. *Acta Materialia*. https://doi.org/10.1016/j.actamat.2016.08.081

[37] Ranganathan, S. (2003). Alloyed pleasures: Multimetallic cocktails. *Current Science*.

[38] Cao, B. X., Wang, C., Yang, T., & Liu, C. T. (2020). Cocktail effects in understanding the stability and properties of face-centered-cubic high-entropy alloys at ambient and cryogenic temperatures. *Scripta Materialia*. https://doi.org/10.1016/j.scriptamat.2020.06.008

[39] Ye, X., Ma, M., Cao, Y., Liu, W., Ye, X., & Gu, Y. (2011). The property research on high-entropy alloy AlxFeCoNiCuCr coating by laser cladding. *Physics Procedia*. https://doi.org/10.1016/j.phpro.2011.03.039

[40] Qiu, X. W., Zhang, Y. P., He, L., & Liu, C. G. (2013). Microstructure and corrosion resistance of AlCrFeCuCo high entropy alloy. *Journal of Alloys and Compounds*. https://doi.org/10.1016/j.jallcom.2012.09.091

[41] Zhang, H., Pan, Y., He, Y., & Jiao, H. (2011). Microstructure and properties of 6FeNiCoSiCrAlTi high-entropy alloy coating prepared by laser cladding. *Applied Surface Science*. https://doi.org/10.1016/j.apsusc.2010.09.084

[42] Zhang, H., Pan, Y., & He, Y. Z. (2011). Synthesis and characterization of FeCoNiCrCu high-entropy alloy coating by laser cladding. *Materials and Design*. https://doi.org/10.1016/j.matdes.2010.12.001

[43] Chen, T. K., Wong, M. S., Shun, T. T., & Yeh, J. W. (2005). Nanostructured nitride films of multi-element high-entropy alloys by reactive DC sputtering. *Surface and Coatings Technology*. https://doi.org/10.1016/j.surfcoat.2005.08.081

[44] Huang, P. K., Yeh, J. W., Shun, T. T., & Chen, S. K. (2004). Multi-principal-element alloys with improved oxidation and wear resistance for thermal spray coating. *Advanced Engineering Materials*. https://doi.org/10.1002/adem.200300507

[45] Zhao, D., Yamaguchi, T., & Wang, W. (2020). Fabrication and wear performance of Al0.8FeCrCoNi high entropy alloy coating on magnesium alloy by resistance seam welding. *Materials Letters*. https://doi.org/10.1016/j.matlet.2019.127250

[46] Kao, Y. F., Chen, S. K., Sheu, J. H., Lin, J. T., Lin, W. E., Yeh, J. W., … Wang, C. W. (2010). Hydrogen storage properties of multi-principal-component CoFeMnTi xVyZrz alloys. *International Journal of Hydrogen Energy*. https://doi.org/10.1016/j.ijhydene.2010.06.012

[47] Chang, S. Y., & Chen, D. S. (2009). 10-nm-thick quinary (AlCrTaTiZr)N film as effective diffusion barrier for Cu interconnects at 900 °c. *Applied Physics Letters*. https://doi.org/10.1063/1.3155196

[48] Chang, S. Y., Huang, Y. C., Li, C. E., Hsu, H. F., Yeh, J. W., & Lin, S. J. (2013). Improved diffusion-resistant ability of multicomponent nitrides: From unitary TiN to senary high-entropy (TiTaCrZrAlRu)N. *JOM*. https://doi.org/10.1007/s11837-013-0676-2

[49] Zhao, Y. J., Qiao, J. W., Ma, S. G., Gao, M. C., Yang, H. J., Chen, M. W., & Zhang, Y. (2016). A hexagonal close-packed high-entropy alloy: The effect of entropy. *Materials and Design*. https://doi.org/10.1016/j.matdes.2016.01.149

[50] Maresca, F., & Curtin, W. A. (2020). Mechanistic origin of high strength in refractory BCC high entropy alloys up to 1900K. *Acta Materialia*. https://doi.org/10.1016/j.actamat.2019.10.015

[51] Tsai, M. H., & Yeh, J. W. (2014). High-entropy alloys: A critical review. *Materials Research Letters*. https://doi.org/10.1080/21663831.2014.912690

[52] Gwalani, B., Soni, V., Lee, M., Mantri, S. A., Ren, Y., & Banerjee, R. (2017). Optimizing the coupled effects of Hall-Petch and precipitation strengthening in a Al0.3CoCrFeNi high entropy alloy. *Materials and Design*. https://doi.org/10.1016/j.matdes.2017.02.072

[53] Wang, W. R., Wang, W. L., Wang, S. C., Tsai, Y. C., Lai, C. H., & Yeh, J. W. (2012). Effects of Al addition on the microstructure and mechanical property of Al xCoCrFeNi high-entropy alloys. *Intermetallics*. https://doi.org/10.1016/j.intermet.2012.03.005

[54] Wang, W. R., Wang, W. L., & Yeh, J. W. (2014). Phases, microstructure and mechanical properties of AlxCoCrFeNi high-entropy alloys at elevated temperatures. *Journal of Alloys and Compounds*. https://doi.org/10.1016/j.jallcom.2013.11.084

[55] Cao, T., Shang, J., Zhao, J., Cheng, C., Wang, R., & Wang, H. (2016). The influence of Al elements on the structure and the creep behavior of AlxCoCrFeNi high entropy alloys. *Materials Letters*. https://doi.org/10.1016/j.matlet.2015.11.016

[56] Joseph, J., Stanford, N., Hodgson, P., & Fabijanic, D. M. (2017). Understanding the mechanical behaviour and the large strength/ductility differences between FCC and BCC AlxCoCrFeNi high entropy alloys. *Journal of Alloys and Compounds*. https://doi.org/10.1016/j.jallcom.2017.08.067

[57] Zhang, K. B., Fu, Z. Y., Zhang, J. Y., Wang, W. M., Wang, H., Wang, Y. C., … Shi, J. (2009). Microstructure and mechanical properties of CoCrFeNiTiAlx high-entropy alloys. *Materials Science and Engineering A*. https://doi.org/10.1016/j.msea.2008.12.053

[58] Manzoni, A. M., Singh, S., Daoud, H. M., Popp, R., Völkl, R., Glatzel, U., & Wanderka, N. (2016). On the path to optimizing the Al-Co-Cr-Cu-Fe-Ni-Ti high entropy alloy family for high temperature applications. *Entropy*. https://doi.org/10.3390/e18040104

[59] Dolique, V., Thomann, A. L., Brault, P., Tessier, Y., & Gillon, P. (2009). Complex structure/composition relationship in thin films of AlCoCrCuFeNi high entropy alloy. *Materials Chemistry and Physics*. https://doi.org/10.1016/j.matchemphys.2009.05.025

[60] Chang, Y. J., Jui, C. Y., Lee, W. J., & Yeh, A. C. (2019). Prediction of the Composition and Hardness of High-Entropy Alloys by Machine Learning. *JOM*. https://doi.org/10.1007/s11837-019-03704-4

[61] Kao, Y. F., Chen, T. J., Chen, S. K., & Yeh, J. W. (2009). Microstructure and mechanical property of as-cast, -homogenized, and -deformed AlxCoCrFeNi ($0 \leq x \leq 2$) high-entropy alloys. *Journal of Alloys and Compounds*, *488*(1), 57–64. https://doi.org/10.1016/j.jallcom.2009.08.090

[62] He, F., Wang, Z., Wu, Q., Li, J., Wang, J., & Liu, C. T. (2017). Phase separation of metastable CoCrFeNi high entropy alloy at intermediate temperatures. *Scripta Materialia*. https://doi.org/10.1016/j.scriptamat.2016.08.008

[63] Liu, J., Guo, X., Lin, Q., He, Z., An, X., Li, L., … Zhang, Y. (2019). Excellent ductility and serration feature of metastable CoCrFeNi high-entropy alloy at extremely low temperatures. *Science China Materials*. https://doi.org/10.1007/s40843-018-9373-y

[64] Li, Z., Pradeep, K. G., Deng, Y., Raabe, D., & Tasan, C. C. (2016). Metastable high-entropy dual-phase alloys overcome the strength-ductility trade-off. *Nature*. https://doi.org/10.1038/nature17981

[65] Zhang, C., Zhu, C., Harrington, T., Casalena, L., Wang, H., Shin, S., & Vecchio, K. S. (2019). Multifunctional Non-Equiatomic High Entropy Alloys with Superelastic, High Damping, and Excellent Cryogenic Properties. *Advanced Engineering Materials*. https://doi.org/10.1002/adem.201800941

[66][H ding] Ding, H., Ding, H., Song, D., Tang, Z., & Yang, P. (2011). Strain hardening behavior of a TRIP/TWIP steel with 18.8% Mn. *Materials Science and Engineering A*, *528*(3), 868–873. https://doi.org/10.1016/j.msea.2010.10.040

[67][Jin] Jin, J. E., & Lee, Y. K. (2009). Strain hardening behavior of a Fe-18Mn-0.6C-1.5Al TWIP steel. *Materials Science and Engineering A*, *527*(1–2), 157–161. https://doi.org/10.1016/j.msea.2009.08.028

[68][Rana] Rana, R., Lahaye, C., & Ray, R. K. (2014). Overview of Lightweight Ferrous Materials: Strategies and Promises. *JOM 2014 66:9*, *66*(9), 1734–1746. https://doi.org/10.1007/S11837-014-1126-5

[69][Madivala] Madivala, M., Schwedt, A., Wong, S. L., Roters, F., Prahl, U., & Bleck, W. (2018). Temperature dependent strain hardening and fracture behavior of TWIP steel. *International Journal of Plasticity*, *104*, 80–103. https://doi.org/10.1016/J.IJPLAS.2018.02.001

[70] Wu, Z., Bei, H., Otto, F., Pharr, G. M., & George, E. P. (2014). Recovery, recrystallization, grain growth and phase stability of a family of FCC-structured multi-component equiatomic solid solution alloys. *Intermetallics*. https://doi.org/10.1016/j.intermet.2013.10.024

[71] Zhang, C., Zhang, F., Chen, S., & Cao, W. (2012). Computational thermodynamics aided high-entropy alloy design. *JOM*. https://doi.org/10.1007/s11837-012-0365-6

[72] Zhang, C., Zhang, F., Diao, H., Gao, M. C., Tang, Z., Poplawsky, J. D., & Liaw, P. K. (2016). Understanding phase stability of Al-Co-Cr-Fe-Ni high entropy alloys. *Materials and Design*. https://doi.org/10.1016/j.matdes.2016.07.073

[73] Bönisch, M., Wu, Y., & Sehitoglu, H. (2018). Twinning-induced strain hardening in dual-phase FeCoCrNiAl0.5 at room and cryogenic temperature. *Scientific Reports*. https://doi.org/10.1038/s41598-018-28784-1

[74] Yang, T., Xia, S., Liu, S., Wang, C., Liu, S., Zhang, Y., … Wang, Y. (2015). Effects of AL addition on microstructure and mechanical properties of AlxCoCrFeNi High-entropy alloy. *Materials Science and Engineering A*. https://doi.org/10.1016/j.msea.2015.09.034

[75] Ma, L., Wang, L., Nie, Z., Wang, F., Xue, Y., Zhou, J., Cao, T., Wang, Y., & Ren, Y. (2017). Reversible deformation-induced martensitic transformation in Al0.6CoCrFeNi high-entropy alloy investigated by in situ synchrotron-based high-energy X-ray diffraction. *Acta Materialia*. https://doi.org/10.1016/j.actamat.2017.02.014

[76] Ritchie, R. O. (2011). The conflicts between strength and toughness. *Nature Materials*. https://doi.org/10.1038/nmat3115

[77] Wei, Y., Li, Y., Zhu, L., Liu, Y., Lei, X., Wang, G., … Gao, H. (2014). Evading the strength-ductility trade-off dilemma in steel through gradient hierarchical nanotwins. *Nature Communications*. https://doi.org/10.1038/ncomms4580

[78] Borovikov, V., Mendelev, M. I., King, A. H., & Lesar, R. (2015). Effect of stacking fault energy on mechanism of plastic deformation in nanotwinned FCC metals. *Modelling and Simulation in Materials Science and Engineering*. https://doi.org/10.1088/0965-0393/23/5/055003

[79] Mishra, R. S., Nene, S. S., Frank, M., Sinha, S., Liu, K., & Shukla, S. (2020). Metastability driven hierarchical microstructural engineering: Overview of mechanical properties of metastable complex concentrated alloys. *Journal of Alloys and Compounds*. https://doi.org/10.1016/j.jallcom.2020.155625

[80] Nene, S. S., Frank, M., Liu, K., Sinha, S., Mishra, R. S., McWilliams, B., & Cho, K. C. (2018). Reversed strength-ductility relationship in microstructurally flexible high entropy alloy. *Scripta Materialia*. https://doi.org/10.1016/j.scriptamat.2018.05.043

[81] Nene, S. S., Sinha, S., Frank, M., Liu, K., Mishra, R. S., McWilliams, B. A., & Cho, K. C. (2018). Unexpected strength–ductility response in an annealed, metastable, high-entropy alloy. *Applied Materials Today*. https://doi.org/10.1016/j.apmt.2018.09.002

[82] Nene, S. S., Frank, M., Liu, K., Mishra, R. S., McWilliams, B. A., & Cho, K. C. (2018). Extremely high strength and work hardening ability in a metastable high entropy alloy. *Scientific Reports*. https://doi.org/10.1038/s41598-018-28383-0

[83] Li, Z., Tasan, C. C., Springer, H., Gault, B., & Raabe, D. (2017). Interstitial atoms enable joint twinning and transformation induced plasticity in strong and ductile high-entropy alloys. *Scientific Reports*. https://doi.org/10.1038/srep40704

[84] Zhao, Y. Y., & Nieh, T. G. (2017). Correlation between lattice distortion and friction stress in Ni-based equiatomic alloys. *Intermetallics*. https://doi.org/10.1016/j.intermet.2017.03.011

[85] Zhao, Y. Y., Lei, Z. F., Lu, Z. P., Huang, J. C., & Nieh, T. G. (2019). A simplified model connecting lattice distortion with friction stress of Nb-based equiatomic high-entropy alloys. *Materials Research Letters*. https://doi.org/10.1080/21663831.2019.1610105

[86] LaRosa, C. R., Shih, M., Varvenne, C., & Ghazisaeidi, M. (2019). Solid solution strengthening theories of high-entropy alloys. *Materials Characterization*. https://doi.org/10.1016/j.matchar.2019.02.034

[87][L shang] Zhang, L., Xiang, Y., Han, J., & Srolovitz, D. J. (2019). The effect of randomness on the strength of high-entropy alloys. *Acta Materialia*. https://doi.org/10.1016/j.actamat.2018.12.032

[88] Toda-Caraballo, I., & Rivera-Díaz-Del-Castillo, P. E. J. (2015). Modelling solid solution hardening in high entropy alloys. *Acta Materialia*. https://doi.org/10.1016/j.actamat.2014.11.014

[89] Yao, H. W., Qiao, J. W., Hawk, J. A., Zhou, H. F., Chen, M. W., & Gao, M. C. (2017). Mechanical properties of refractory high-entropy alloys: Experiments and modeling. *Journal of Alloys and Compounds*. https://doi.org/10.1016/j.jallcom.2016.11.188

[90] Shun, T. T., & Du, Y. C. (2009). Microstructure and tensile behaviors of FCC Al0.3CoCrFeNi high entropy alloy. *Journal of Alloys and Compounds*. https://doi.org/10.1016/j.jallcom.2008.12.088

[91] Tang, Q. H., Huang, Y., Huang, Y. Y., Liao, X. Z., Langdon, T. G., & Dai, P. Q. (2015). Hardening of an Al0.3CoCrFeNi high entropy alloy via high-pressure torsion and thermal annealing. *Materials Letters*. https://doi.org/10.1016/j.matlet.2015.03.066

[92] Yasuda, H. Y., Shigeno, K., & Nagase, T. (2015). Dynamic strain aging of Al0.3CoCrFeNi high entropy alloy single crystals. *Scripta Materialia*. https://doi.org/10.1016/j.scriptamat.2015.06.022

[93] Li, D., Li, C., Feng, T., Zhang, Y., Sha, G., Lewandowski, J. J., … Zhang, Y. (2017). High-entropy Al0.3CoCrFeNi alloy fibers with high tensile strength and ductility at ambient and cryogenic temperatures. *Acta Materialia*. https://doi.org/10.1016/j.actamat.2016.10.038

[94] He, J. Y., Wang, H., Huang, H. L., Xu, X. D., Chen, M. W., Wu, Y., … Lu, Z. P. (2016). A precipitation-hardened high-entropy alloy with outstanding tensile properties. *Acta Materialia*. https://doi.org/10.1016/j.actamat.2015.08.076

[95] Lu, W., Luo, X., Yang, Y., & Huang, B. (2020). Hall-petch relationship and heterogeneous strength of CrCoNi medium-entropy alloy. *Materials Chemistry and Physics*. https://doi.org/10.1016/j.matchemphys.2020.123073

[96] Liu, W. H., Wu, Y., He, J. Y., Nieh, T. G., & Lu, Z. P. (2013). Grain growth and the Hall-Petch relationship in a high-entropy FeCrNiCoMn alloy. *Scripta Materialia*. https://doi.org/10.1016/j.scriptamat.2012.12.002

[97] Kim, J. H., Serpantié, A., Barlat, F., Pierron, F., & Lee, M. G. (2013). Characterization of the post-necking strain hardening behavior using the virtual fields method. *International Journal of Solids and Structures*. https://doi.org/10.1016/j.ijsolstr.2013.07.018

[98] Gumbsch, P. (2003). MATERIALS SCIENCE: Modeling Strain Hardening the Hard Way. *Science*. https://doi.org/10.1126/science.1090482

[99] Curtze, S., & Kuokkala, V. T. (2010). Dependence of tensile deformation behavior of TWIP steels on stacking fault energy, temperature and strain rate. *Acta Materialia*. https://doi.org/10.1016/j.actamat.2010.05.049

[100] Choi, W. S., De Cooman, B. C., Sandlöbes, S., & Raabe, D. (2015). Size and orientation effects in partial dislocation-mediated deformation of twinning-induced plasticity steel micro-pillars. *Acta Materialia*. https://doi.org/10.1016/j.actamat.2015.06.065

[101] Kibey, S., Liu, J. B., Johnson, D. D., & Sehitoglu, H. (2007). Predicting twinning stress in fcc metals: Linking twin-energy pathways to twin nucleation. *Acta Materialia*, *55*(20), 6843–6851. https://doi.org/10.1016/j.actamat.2007.08.042

[102] Uchic, M. D., Dimiduk, D. M., Florando, J. N., & Nix, W. D. (2004). Sample dimensions influence strength and crystal plasticity. *Science*. https://doi.org/10.1126/science.1098993

[103] Greer, J. R., Oliver, W. C., & Nix, W. D. (2005). Size dependence of mechanical properties of gold at the micron scale in the absence of strain gradients. *Acta Materialia*. https://doi.org/10.1016/j.actamat.2004.12.031

[104] Greer, J. R., & De Hosson, J. T. M. (2011). Plasticity in small-sized metallic systems: Intrinsic versus extrinsic size effect. *Progress in Materials Science*. https://doi.org/10.1016/j.pmatsci.2011.01.005

[105] Fei, H., Abraham, A., Chawla, N., & Jiang, H. (2012). Evaluation of micro-pillar compression tests for accurate determination of elastic-plastic constitutive relations. *Journal of Applied Mechanics, Transactions ASME*. https://doi.org/10.1115/1.4006767

[106] Sneddon, I. N. (1965). The relation between load and penetration in the axisymmetric boussinesq problem for a punch of arbitrary profile. *International Journal of Engineering Science*. https://doi.org/10.1016/0020-7225(65)90019-4

[107] Kundu, J., Ray, T., Kundu, A., & Shome, M. (2019). Effect of the laser power on the mechanical performance of the laser spot welds in dual phase steels. *Journal of Materials Processing Technology*. https://doi.org/10.1016/j.jmatprotec.2018.12.014

[108] Sokkalingam, R., Sivaprasad, K., Muthupandi, V., & Duraiselvam, M. (2018). Characterization of laser beam welded Al0.5CoCrFeNi high-entropy alloy. *Key Engineering Materials*. https://doi.org/10.4028/www.scientific.net/KEM.775.448

[109] Wu, Z., David, S. A., Leonard, D. N., Feng, Z., & Bei, H. (2018). Microstructures and mechanical properties of a welded CoCrFeMnNi high-entropy alloy. *Science and Technology of Welding and Joining*. https://doi.org/10.1080/13621718.2018.1430114

[110] Shigesato, G., & Sugiyama, M. (2002). Development of in situ observation technique using scanning ion microscopy and demonstration of Mn depletion effect on intragranular ferrite transformation in low-alloy steel. *Journal of Electron Microscopy*. https://doi.org/10.1093/jmicro/51.6.359

[111] Savage, W. F., Nippes, E. F., & Mushala, M. C. (1978). LIQUID-METAL EMBRITTLEMENT OF THE HEAT-AFFECTED ZONE BY COPPER CONTAMINATION. *Welding Journal (Miami, Fla)*.

[112] Nippes, E. F., & Ball, D. J. (1982). COPPER-CONTAMINATION CRACKING: CRACKING MECHANISM AND CRACK INHIBITORS. *Welding Journal (Miami, Fla)*.

[113] Nandan, R., Roy, G. G., Lienert, T. J., & Debroy, T. (2007). Three-dimensional heat and material flow during friction stir welding of mild steel. *Acta Materialia*, *55*(3), 883–895. https://doi.org/10.1016/j.actamat.2006.09.009

[114] Zener, C., & Hollomon, J. H. (1944). Effect of strain rate upon plastic flow of steel. *Journal of Applied Physics*, *15*(1), 22–32. https://doi.org/10.1063/1.1707363

[115] Mishra, R. S., & Ma, Z. Y. (2005). Friction stir welding and processing. *Materials Science and Engineering R: Reports*. https://doi.org/10.1016/j.mser.2005.07.001

[116] Sittiho, A., Tungala, V., Charit, I., & Mishra, R. S. (2018). Microstructure, mechanical properties and strengthening mechanisms of friction stir welded Kanthal APMT^{TM} steel. *Journal of Nuclear Materials*, *509*. https://doi.org/10.1016/j.jnucmat.2018.07.001

[117] Zhao, D., Yamaguchi, T., Shu, J., Tokunaga, T., & Danjo, T. (2020). Rapid fabrication of the continuous AlFeCrCoNi high entropy alloy coating on aluminum alloy by resistance seam welding. *Applied Surface Science*, *517*, 145980. https://doi.org/10.1016/j.apsusc.2020.145980

Chapter 2: Friction Stir Processing of a High Entropy Alloy $Fe_{42}Co_{10}Cr_{15}Mn_{28}Si_5$ with Transformative Characteristics: Microstructure and Mechanical Properties

Abstract

High entropy alloys (HEA) are an emerging class of novel metallic alloys with the ability to develop unique microstructural modification by using thermomechanical processing techniques. In this study, friction stir processing (FSP), widely regarded as an effective thermomechanical processing technique, was applied to a rolled HEA of nominal composition $Fe_{42}Co_{10}Cr_{15}Mn_{28}Si_5$ (at.%). The work involves examination and analysis of the microstructural characteristics by optical microscopy, transmission electron microscopy, and electron backscatter diffraction. Also, X-ray diffraction was used to identify the different phases present in the HEA both before and after FSP. The mechanical behavior of the HEA was evaluated by compression testing at room temperature. The compressive yield stress of the base metal changed from 277 MPa to about 270 MPa although statistically no appreciable change was noted. The work hardenability of the SZ and the parent material was analyzed in terms of strain hardening exponents and strain hardening rates in the light of existing work hardening theories.

2.1 Introduction

Originally, HEAs were designed to have five or more equiatomic elements in order to have high configurational entropy leading to stabilization of single-phase solid solution alloys and suppression of undesired intermetallic phase formation. While HEAs based on such alloy design exhibited instances of certain improved properties, the strict alloy design rule failed to deliver superior combinations of properties in most cases. This led to the advent of non-equiatomic HEAs by relaxing the prior restrictive rules of single-phase solid solution HEAs [1- 3]. The purpose of developing non-equiatomic HEAs is to obtain the desired properties by adjusting their chemical compositions while maintaining high configurational entropy to suppress detrimental intermetallic phase formation.

By modifying the chemistry of an equiatomic HEA, the alloys with a combination of high strength and decent ductility can be obtained. This is attributed to the low stacking fault energy (SFE) which promotes special modes of deformation in the alloys [4-7]. The factors that affect SFE in those alloys include chemical composition, processing temperature, grain size and strain [8-10]. In crystalline materials, plasticity generally involves movement of dislocations. Apart from deformation by slip, in low-SFE alloys the plasticity is accompanied by displacive lattice transformation, *i.e.*, transformation induced plasticity (TRIP). It is well known that TRIP effect occurs when FCC austenite (γ) phase transforms to HCP ε-martensite or BCT α'-martensite phase [11]. This type of strain-induced transformation occurs geometrically at certain habit planes of the parent lattice structure, leading to changes in mechanical properties [12].

Li *et al.* [13] initiated the first study of tunable non-equiatomic HEA termed as TRIP dual phase (DP) HEA. They altered the chemical composition of FeMnCoCr HEA in order to obtain a dual phase microstructure. Changing from single phase to dual phase, TRIP HEA improved the mechanical behavior of the alloy with a better combination of strength and ductility while maintaining the solid solution strengthening effect. The friction stir welding/processing (FSW/P) technique using a non-consumable tool to plunge and stir the plate to produce heat and material transfer has been demonstrated to have beneficial effects on the microstructural modification of this HEA system [14, 15]. Nene *et al.* [16-18] applied FSP technique to a $Fe_{42}Co_{10}Cr_{15}Mn_{28}Si_5$ HEA and demonstrated that, via changing processing parameters, one can adjust the phase proportions of FCC γ and HCP ε-martensite phases. However, the phase transformation mechanisms involving martensitic transformation during FSP has not been studied in detail.

In the present study, a HEA with similar TRIP composition $Fe_{42}Co_{10}Cr_{15}Mn_{28}Si_5$ (at%) was chosen and FSP was used as a thermomechanical processing technique to study the associated microstructural modification and its effect on mechanical properties of the HEA. Previous studies on FSP of these TRIP-HEAs examined the mechanical properties mainly by performing mini-tensile testing. Here, on the other hand, compression testing was conducted both on the base metal and the stir zone. Furthermore, the underlying strengthening mechanisms operational behind the exhibited mechanical behavior of the FSPed HEA are elucidated in the light of existing theories.

2.2 Experimental procedures

The material used in this study was a HEA with a nominal composition of $Fe_{48}Co_{10}Cr_{15}Mn_{28}Si_5$ (at%). The alloy was produced by vacuum arc-casting under inert argon atmosphere at Sophisticated Alloys Inc., Butler, PA, USA. The as-cast slab was hot rolled to 20% thickness reduction to a plate of 13 mm thickness. FSP was done along the rolling direction of the plate by using a tungsten-rhenium tool with a shoulder diameter of 12 mm, a tapered pin of 3.5 mm height, and 6 mm diameter. For this single-pass FSP run, a tool rotation rate of 350 rpm, traverse speed of 50.4 mm/min, forging force of 36 kN, and tool tilt of 2^{o} were used.

Initial microstructural investigation was carried out using an Olympus PMG-3 light optical microscope. Specimen preparation for optical microscopy was done first by sectioning the FSPed plate in a transverse section. The sectioned specimens were then ground consecutively with SiC papers from 120 to 1200 grit size and polished with alumina slurry down to 0.1 μm. The specimens were cleaned using an ultrasonic cleaner before etching. A mixture of hydrochloric acid and nitric acid in the ratio of 3:1, (by volume) was used as the chemical etchant for revealing the optical microstructure. X-ray diffraction (XRD) experiments were conducted on the specimens by using a Siemens D5000 X-ray diffractometer using Copper K_{α} X-rays. The scanning step was made at 0.5^{o} across the diffraction angle (2θ) range from 40^{o} to 50^{o}. XRD was utilized to detect the presence of various phases based on their crystallographic characteristics. The peak analysis of XRD pattern was done by using Pseudo-Voigt fitting method.

For phase analysis, the specimens were further polished down to 0.05 μm with alumina slurry using a Pace Technology GIGA-900 Vibratory Polisher for 8 h. Scanning electron microscopy (SEM) was performed in a FEI Scios SEM. ThermoFisher Scientific Quasar^{TM} detector was used to perform EBSD studies to obtain information on grain boundary statistics and phase types. The parameters used for obtaining EBSD data include accelerating voltage of 20 kV and scan step sizes of 620 nm, 200 nm and 100 nm for the BM, the SZ, and the deformed or compressed BM/SZ, respectively. The beam current and dwell time for the EBSD pattern acquisitions used were 0.4 nA and 100 ms, respectively, for all specimens.

For TEM sample preparation, foils of 50 to 100 μm thickness were first prepared by mechanical grinding and polishing down to 1 μm finish, and later 3-mm diameter discs were punched out. Afterward, twinjet electropolishing (Fischione 110 electro twin jet polisher) technique was used to further thin the discs. The electrolyte used was 15% Nital (nitric acid: ethyl alcohol = 15:85, by volume). Temperature of the electrolyte was kept at -40^{o}C by using dry ice bath and electropolishing voltage was kept at 30 V for the base metal (BM) and 35 V for the FSPed specimen (SZ). In order to study the fine microstructural details, TEM was performed on the SZ and BM specimens using a FEI Tecnai TF30-FEG STwin STEM operated at an accelerating voltage of 300 kV.

Uniaxial compression testing was done on small cuboid shaped specimens with 2 mm × 2 mm cross-section and 4.5 mm height from each of the SZ and the BM. The compression specimens were taken along the FSP longitudinal direction inside the SZ and along the rolling direction of the BM. The compression tests were performed on a model 5982 Instron machine (load capacity of 100 kN) at room temperature with an initial strain rate of 10^{-3} s^{-1}. After the compression tests were done on both the BM and SZ specimens, the deformed specimens were subjected to subsequent microstructural analyses including TEM and EBSD; the details of the characterization techniques have been described previously in this section.

2.3 Results

2.3.1 Microstructural and phase characteristics

Optical metallography was performed on both the base material (BM) and the stir zone (SZ) of the FSPed HEA. **Figure 2.1(a)** and **(b)** show the light optical micrographs taken from the BM and the center location of the SZ, respectively. Several of such optical micrographs were used to determine the grain size of both the samples. The grain sizes of the BM and SZ were measured to be 120±12 μm and 5±1 μm, respectively. This clearly shows that a significant extent of grain refinement (by about 96%) was achieved via FSP. To glean little more details on the microstructure, SEM was performed on the same metallographic samples. **Figure 2.1 (c)** and **(d)** show the backscattered electron (BSE) SEM images of the BM and SZ, respectively. These images reveal that the microstructure is complex with phases of different morphologies being present in both the specimens. Energy dispersive spectroscopy (EDS) technique available with SEM was performed at various locations of both the BM and SZ microstructure, revealing no perceptible change in the local composition.

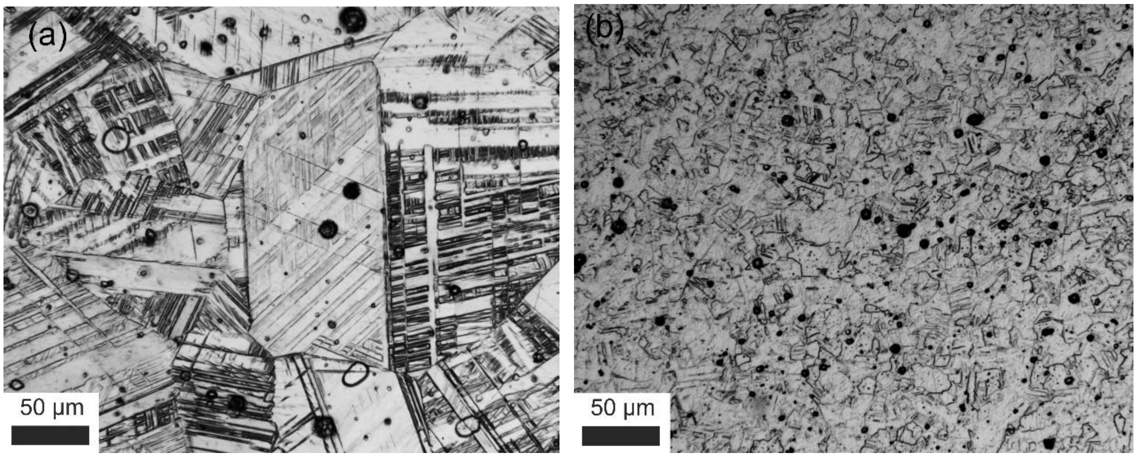

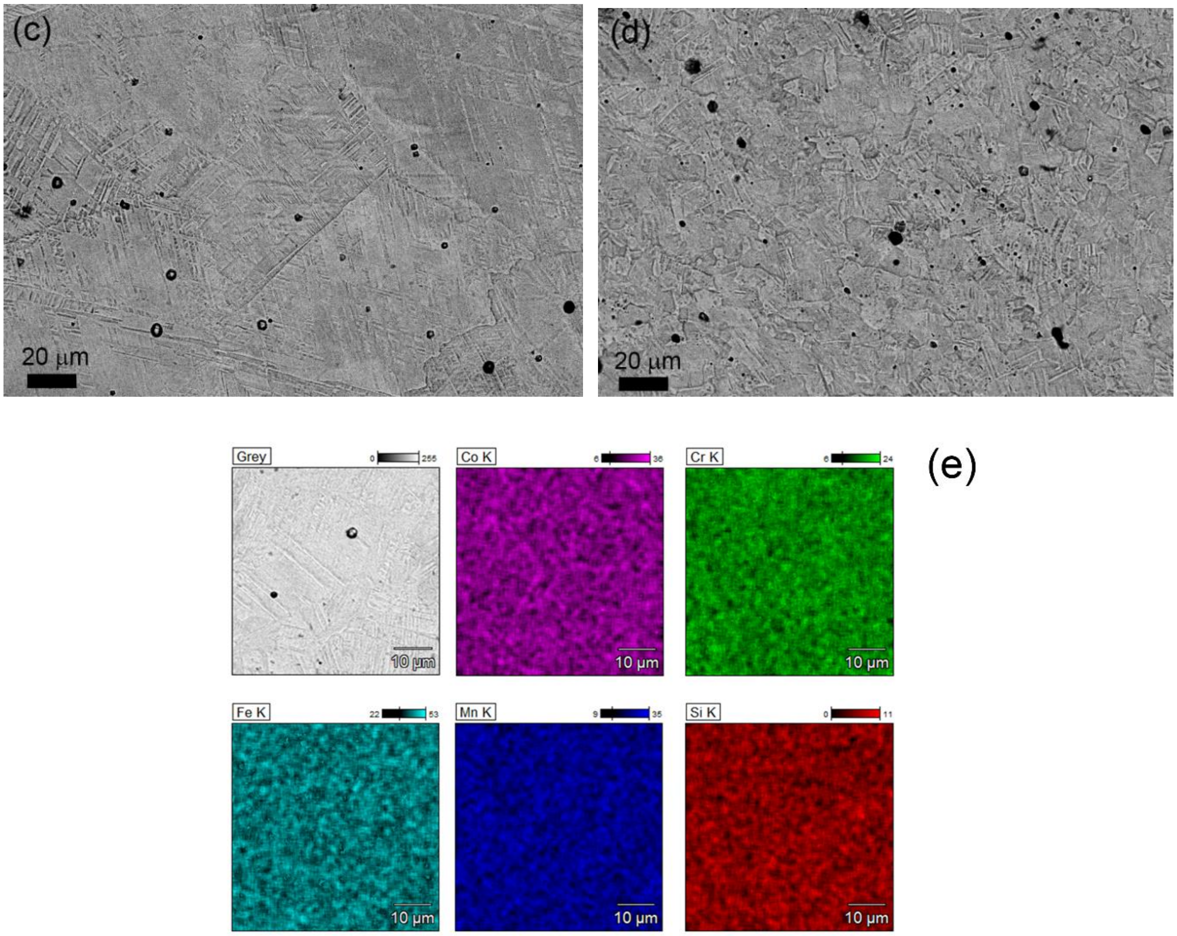

Figure 2.1. Microstructural characteristics of $Fe_{48}Co_{10}Cr_{15}Mn_{28}Si_5$ HEA: Optical micrographs of (a) the base material and (b) the stir zone. Back scattered electron SEM images of (c) the base material and (d) the stir zone, and (e) EDS elemental maps, showing the uniformity elemental distribution, from the BM.

The TRIP HEA alloy composition is expected to have a dual phase microstructure. **Figure 2.2** shows the X-ray diffraction patterns of the BM, the SZ, the deformed BM and the deformed SZ all in a single figure for crystallographic comparisons among the specimens. The XRD peak analysis reveals the presence of FCC γ-phase and HCP ε-martensite phase in all specimens. The lattice parameters were calculated from the diffraction data using the relationship $d_{hkl} = \frac{a}{\sqrt{h^2+k^2+l^2}}$ for FCC and $d_{hkl} = [\frac{4}{3}\left(\frac{h^2+k^2+hk}{a^2}\right) + \frac{l^2}{c^2}]^{-\frac{1}{2}}$ for HCP lattice, where d_{hkl} is the interplanar spacing for given $\{hkl\}$ planes of FCC and equivalent {hkl} planes of HCP crystals, , and a and c are the corresponding lattice parameters of the crystals [19]. The lattice parameter, a, of the FCC γ-phase is calculated to be 0.359 nm, and ε-phase lattice parameters slightly vary among the specimens as shown in **Table 2.1**.

Table 2.1. Lattice parameters of epsilon phase from each specimen.

Type of Specimen	a (Å)	c (Å)	c/a ratio
BM	2.528	4.099	1.622
SZ	2.537	4.099	1.616
Deformed BM	2.528	4.095	1.620
Deformed SZ	2.528	4.095	1.620

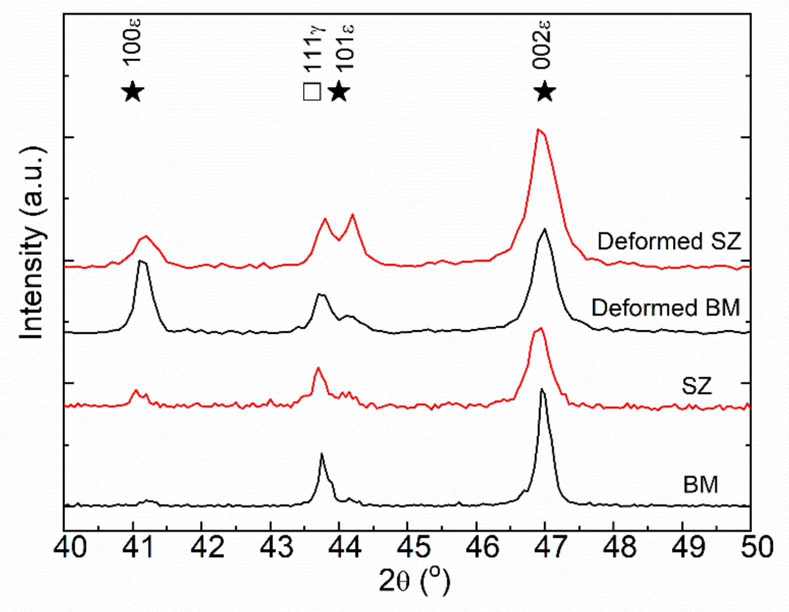

Figure 2.2. X-ray diffraction patterns of $Fe_{42}Co_{10}Cr_{15}Mn_{28}Si_5$ HEA for both the base material (BM), the stir zone (SZ), deformed base material (deformed BM), and deformed stir zone (deformed SZ) specimens.

Figure 2.3 (a) and **(b)** show an EBSD picture quality (PQ) map and phase map of the BM specimen, respectively, confirming the dual-phase (γ + ε) nature of the microstructure. From the phase map, the BM is found to have 52% HCP ε-martensite phase and 48% FCC γ phase. **Figure 2.3 (c)** and **(d)** show an EBSD PQ map and a phase map of the SZ specimen, respectively. The SZ microstructure appears to have a lower HCP ε-martensite phase fraction (39%) and an enhanced amount of fine *γ* grains (61%) as compared to the BM. No trace of any α′-martensite or ferrite phase could be detected. The *ε*-martensite phase in the BM labelled as the red regions in the phase map of **Figure 2.3 (b)** is found to have much larger 'backbone-and-branch' type morphology, whereas the same phase in the SZ exhibits no such branching ε-plate and are much smaller in dimension as shown in **Figure 2.3 (d)**. Note that the smaller size of the *ε*-phase in the SZ is due to the finer grain size (5 μm) in which they formed, compared to the grain size in the BM (120 μm). The histogram plots of grain boundary angle distribution constructed from the EBSD misorientation data of both BM and SZ are shown in **Figure 2.3 (e)**. From this figure, it can be noted that the SZ contains a higher fraction of low angle grain boundaries (LAGBs)

(24%) as compared to the BM (only 13%). In this study, LAGBs are defined as the grain boundaries having angles less than 15°.

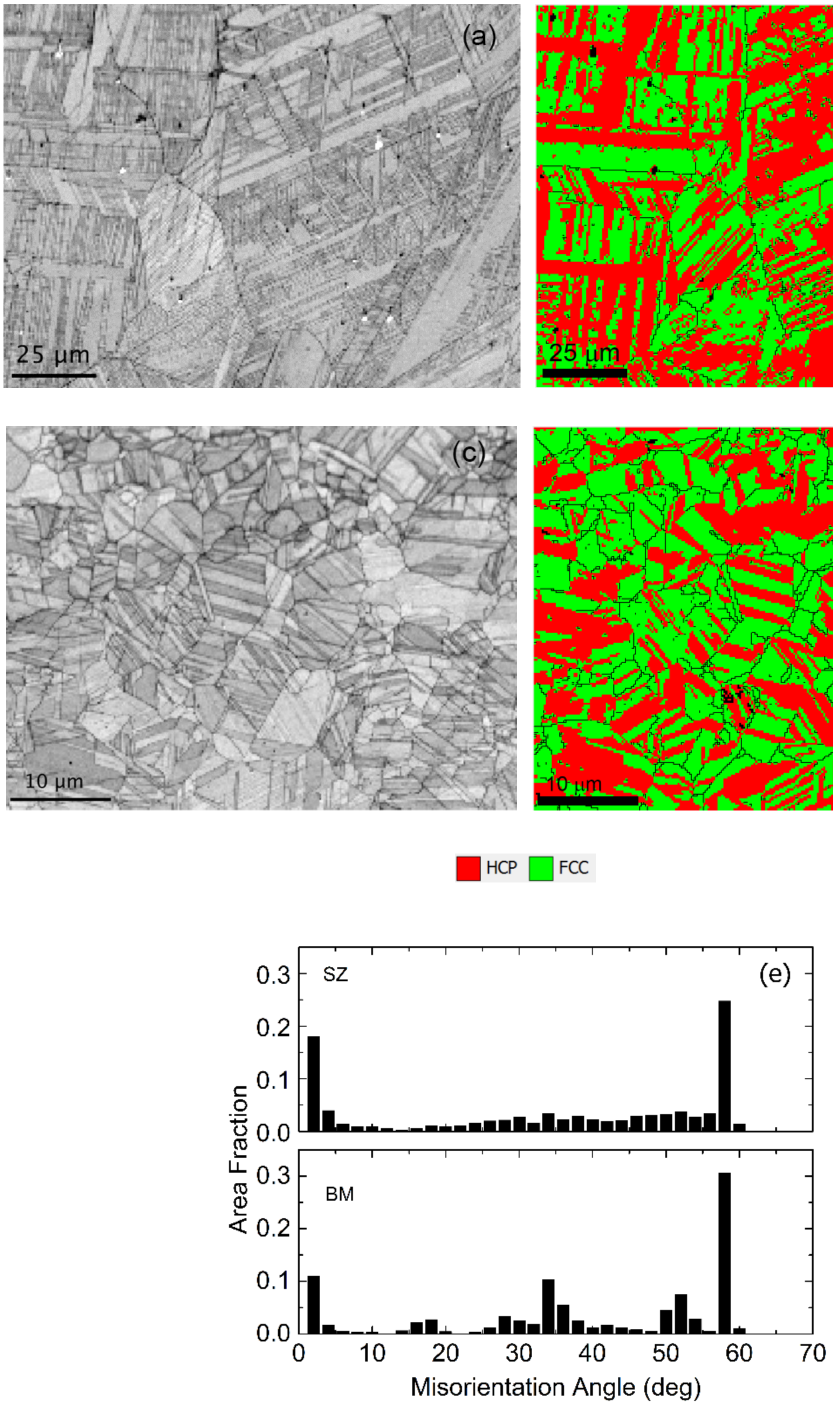

Figure 2.3. EBSD data show the phase distribution in the dual-phase TRIP HEA: HCP ε-martensite (red) and FCC γ phase (green) before and after FSP. In the BM, (a) EBSD Picture Quality (PQ) map and (b) the corresponding EBSD phase map; in the SZ, (c) PQ map and (d) the corresponding phase map. (e) Grain boundary misorientation histogram plots of the BM and SZ.

In the previous sections, a general idea of the microstructure has, so far, been developed. However, to further understand the fine details of the microstructure, TEM was performed on both BM and SZ specimens and the representative images are shown in **Figure 2.4 (a)-(d)**. TEM micrographs from both the BM and the SZ show presence of the ε-plates inside the γ-matrix Stacking faults (SF) in the BM is found to lie parallel to the ε-plate shown in **Figure 2.4 (a)**. Also, dense substructures are found inside the ε-phase as shown in **Figure 2.4 (b)**. In the SZ, the majority of ε-plates grow across the γ-grain with no secondary plates as seen in **Figure 2.4 (c)**. The SF morphology in the SZ appears as complex, parallelepiped structures within the γ matrix and the SFs are densely spaced as depicted in **Figure 2.4 (d)**.

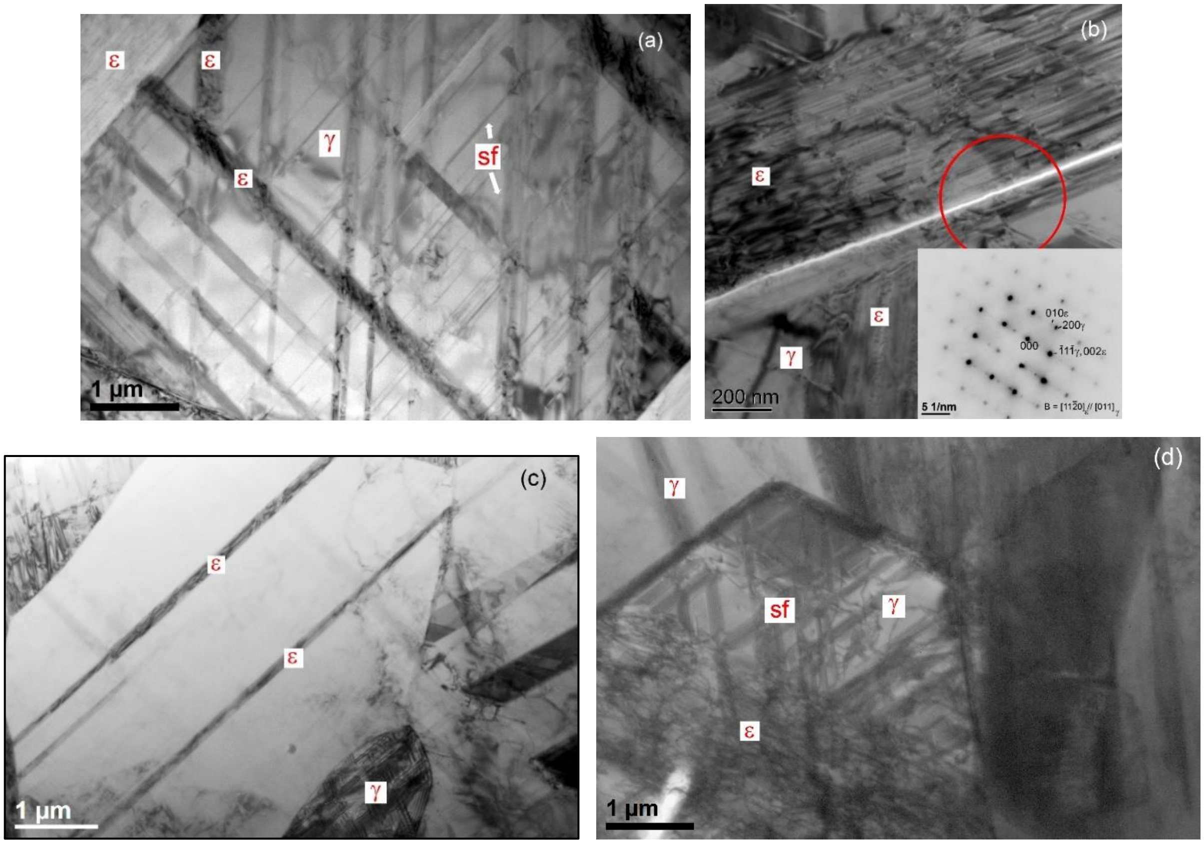

Figure 2.4. TEM bright field image from (a) and (b) the BM with the SAED pattern taken from the circled area, (c) and (d) the SZ.

The microstructure after the uniaxial compression is shown in Figure 5. The BM microstructure changed by increasing the ε-martensitic phase. The SZ deformation is accommodated by martensitic transformation and deformation twin (DT). **Figure 2.5 (a)** and **(b)** show the overlaid EBSD phase maps and picture quality maps of the deformed BM and the deformed SZ specimens. The corresponding TEM images of those specimens are shown in **Figure 2.5 (c)** and **(d**), respectively. The deformed BM specimen shows martensitic plate growth that extends between the pre-existing martensitic plates. The amount of ε-phase in the deformed BM specimen is estimated to be 72% whereas in the deformed SZ specimen the martensitic phase dominates the microstructure with the ε-phase present to the tune of 89%.

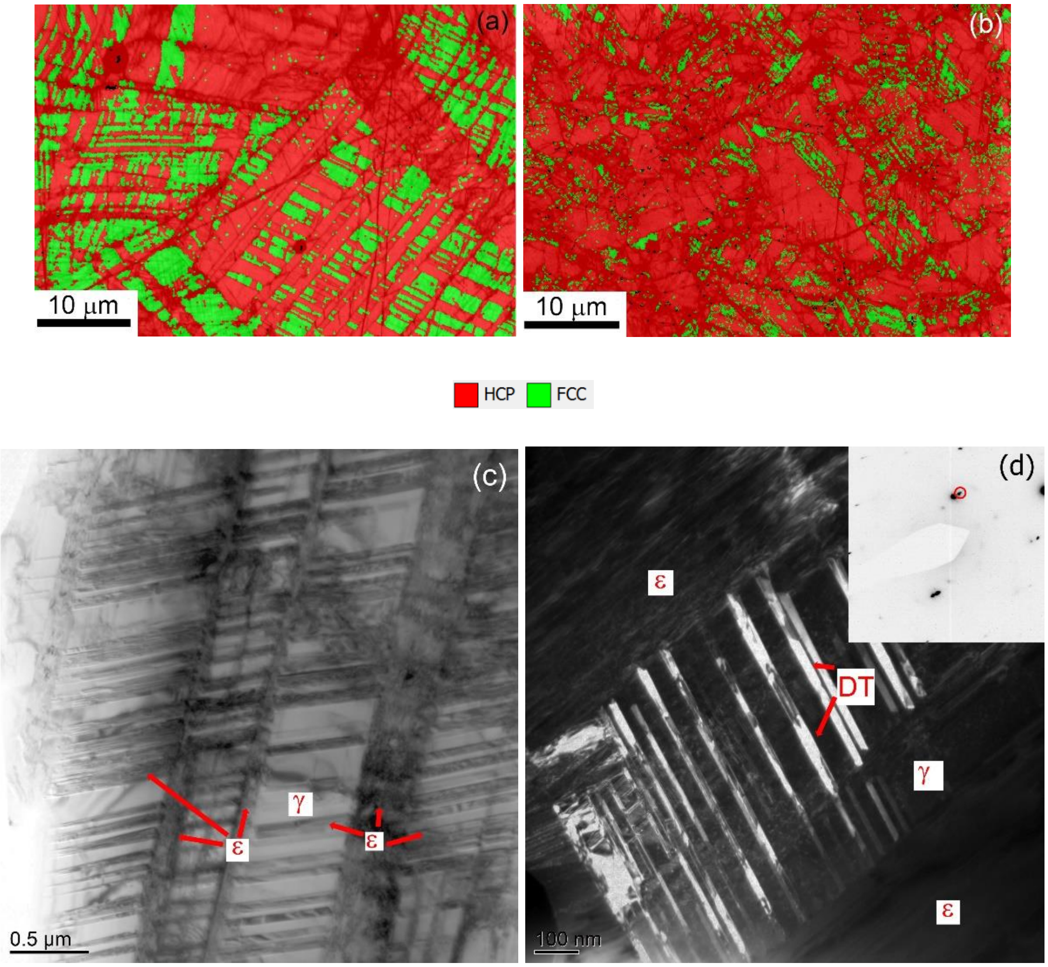

Figure 2.5. The EBSD phase maps of (a) the deformed BM and (b) the deformed SZ specimens. The brightfield TEM micrograph of (c) the deformed BM and (d) the dark field TEM micrograph of the deformed SZ with a diffraction pattern inset.

2.3.2 Mechanical properties

Compression flow curves with strain hardening rates of the BM and the SZ are plotted together in **Figure 2.6 (a)** and **(b)**, respectively. Yield strengths (σ_y) of both the specimens are determined to be 277±6 MPa and 270±2 MPa, respectively. Interestingly, the strain hardening rate of the SZ (8250±50 MPa) is found to be higher than that of the BM (5800±400 MPa). Based on Hollomon's equation, $\sigma = k\varepsilon^n$, where σ is the true stress, ε the true plastic strain, k the strength coefficient, and n the strain hardening exponent, the n values were calculated from the slope of the double logarithmic plot in

Figure 2.6 (c) and are presented in **Table II**. In this work, the strain hardening exponents are calculated using the data within approximately 3-6% strain range for comparison between the strain hardening behavior of BM and SZ. The low-strain data are not used for the strain hardening exponent calculations here because of the transient nature of the initial plastic deformation and the inherent limitations of Hollomon’s equation to capture the initial plastic flow behavior just after yielding [20].

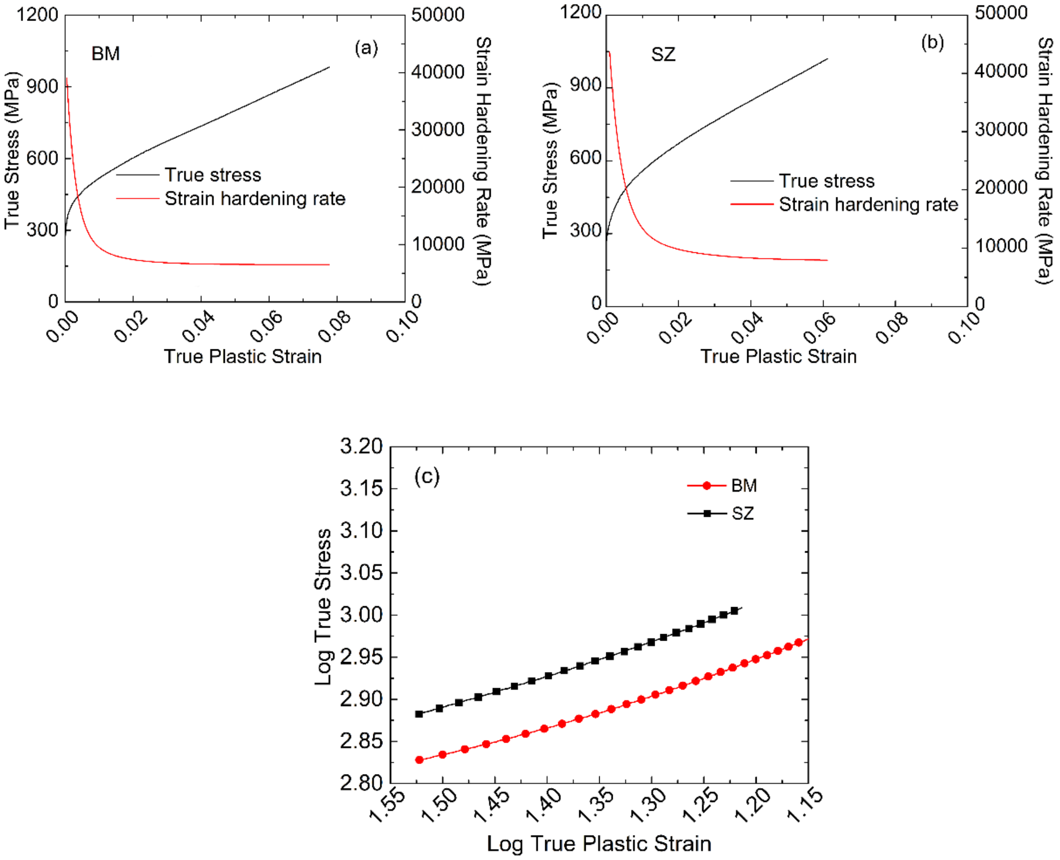

Figure 2.6. Flow curves and strain hardening curve from a) the BM and b) the SZ specimen of the HEA alloy. c) The log-log plot of flow curve data for the BM and SZ.

Table 2.2. Strain hardening exponent (n) at simultaneous strain from 3% to 6%

Log strain	**Equivalent strain (%)**	n_{BM}	n_{SZ}
-1.50 to -1.35	3.16 to 4.47	0.33	0.38
-1.35 to -1.25	4.47 to 5.62	0.41	0.44

2.4 Discussion

2.4.1 Microstructural evolution during FSP

Microstructure of the SZ underwent complex phase transformation during FSP. Dynamic recrystallization during FSP resulted in finer grain size. Newly recrystallized grains were found around grain boundaries in the SZ as shown in **Figure 2.3 (c)**, which suggests that the HEA underwent discontinuous dynamic recrystallization (DDRX) during FSP [17, 21]. The process of DDRX is common in low stacking fault energy materials where recovery is difficult [22]. This mechanism involves recrystallization at high angle grain boundaries when a strain threshold is reached. As seen previously in **Figure 2.3 (a),** the recrystallized microstructure shows groups of smaller recrystallized grains accompanied by some larger grains. This suggests that the fine, dynamically recrystallized γ-phase grains were formed during FSP (as evidenced in **Figure 2.3 (c, d)**). Subsequently, the strain field from the process itself transformed some portion of the γ-phase to ε-phase. This can be seen from the TEM micrographs (**Figure 2.4 (c)**) of the SZ, in which some grains are entirely free of any martensitic phase whereas there are also grains with a high density of stacking faults and ε-martensitic phases.

After an alloy undergoes recrystallization under thermomechanical processing, the grain boundary misorientation distribution is changed. In this work, the LAGB fraction in the BM is lower than that in the SZ (14% vs. 26%). When comparing equivalent coincident site lattice (CSL), Σ3 boundary, using criterion from Brandon's work [23], the BM has higher Σ3 boundary (43% vs. 36%) compared to the SZ. The higher amount of these special boundaries in the BM indicates that there is more fraction of twin boundaries in the BM. After the alloy underwent recrystallization during FSP, as in the SZ, newly recrystallized grains evolved at the expense of the grains containing those CSL boundaries. However, the number remained significantly high. That means there was further microstructural evolution occurring following DDRX, such as the formation. annealing twins after FSP.

The HEA alloy, $Fe_{42}Co_{10}Cr_{15}Mn_{28}Si_5$, has a dual phase microstructure comprised of FCC and HCP phases. From previous studies [14-16], it is known that the HCP phase is formed by TRIP effect and is termed as ε-martensite. Crystallographic relationship between these two phases follows Shoji-Nishiyama relation, $[011]_\gamma \; // \; [11\bar{2}0]_\varepsilon$ [24]. This relationship indicates that the phase transformation occurred via lattice translation of $(011)_\gamma$ plane along $[11\bar{2}]_\gamma$ direction by an amount of $\frac{a}{\sqrt{6}}$, which is equivalent to the Burgers vector magnitude of the partial dislocations in the FCC phase. This occurrence reflects the similarity between the mechanisms of stacking fault formation and ε-martensite nucleation in this alloy. This could be construed as the evidence of the ε-martensite phase formation from the stacking faults. FSP is considered as a severe plastic deformation process with a thermomechanical nature, resulting in significant grain refinement [25, 26]. The morphology of ε-phase is different between the BM and the SZ, which is governed by the γ phase grain size before the martensitic transformation as shown in the study from Takaki and coworkers [27]. Since the austenitic grain size is larger in the BM, the ε-martensite morphology shows *Type-IV* characteristics where the ε-martensite nucleates and grows from both γ grains and existing ε-martensite phase. Conversely, the finer grain size in the SZ shows *Type-II* martensitic morphology where ε-martensite nucleates predominantly at the γ-phase grain boundary and grows across the grains. Schematics of Type-IV and Type-II martensitic transformations are illustrated in **Figure 2.7**.

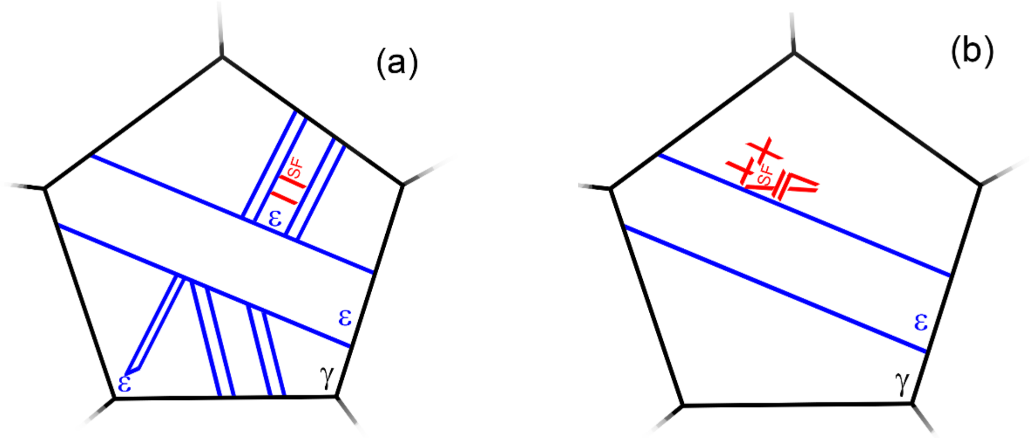

Figure 2.7. Morphology of (a) Type-IV and (b) Type II deformation induced martensitic transformation.

Apart from the martensitic phase transformation, the SFs morphology shows some interesting change. Stacking faults are easily found in materials with low SF energy. In the BM, SFs align with [111] direction. In contrast, the SFs found in the SZ have parallelepiped morphology and are densely packed. There is significantly higher number of overlapping SFs which play an important role in impeding dislocation movement. Individual SFs are considered a weak dislocation obstacle, but when more SFs are packed together, they can become strong obstacles [28].

The extent of the TRIP effect depends on the strain and the strain rate the material undergoes. The deformation behavior of a material under FSP is complex making the actual measurement of strain rather complicated. Some studies have suggested that the accumulated strain during FSP can range between 6 to 100 and the associated strain rates can reach up to 10 s^{-1} [29, 30], depending on FSP parameters. The strain rate of the rolling process can be up to 50 s^{-1} [31]. While the rolling process provides some smaller deformation, the γ to ε phase transformation can be observed but the strain energy is not high enough to make the alloy undergo recrystallization in a single step.

The recrystallized grains in the deformed SZ undergo twinning and martensitic transformation upon deformation and a large fraction of ε-phase was observed in the deformed SZ increasing to 89% from mere 39% in the as received SZ. In contrast, the deformed BM shows only transformation induced plasticity mechanism. It shows the increasing of ε-phase from 52% to 72%. Deformation twins observed in the deformed SZ specimen could be the result of the grain refinement from FSP. Grain refinement impacts the SF energy of the system by increasing the stacking fault energy of the system as the grain size decreases [33]. Thus, the deformation mechanisms in the SZ show additional twinning induced plasticity. Twinning induced plasticity effect is a phase transformation that takes place when stacking fault energy is higher than that of TRIP effect but smaller than that of dislocation glide. In the deformed SZ, there is higher martensitic transformation, where the ε-phase fraction increased substantially from 39% to 89%. On the other hand, the phase transformation in the BM after compression shows only an increase of 20% in the ε-phase fraction (from 52% to 72%). From the greater increase of the ε-phase fraction in the deformed SZ, the deformation mechanism is mainly comprised of TRIP mode. In the deformed BM, martensitic transformation is somewhat deterred due to the already existing martensitic phase.

2.4.2 Mechanical behaviors

The BM and the SZ have only slight difference in yield strength with the BM being the greater. This implies that there are other microstructural hardening contributions from higher amount of ε-martensite to the strengthening mechanisms despite the obvious grain size reduction due to FSP. However, the strain hardening rate is found to be higher in the SZ than that in the BM. Strain hardening is primarily a manifestation of interactions between dislocations. Strain hardening in both the specimens show the change that is indicative of the deformation induced phase transformation, *i.e.*, transformation induced plasticity or twinning induced plasticity during the deformation. Initial strain hardening rate decreasing after elastic deformation reflects the start of dislocation movement. The strain hardening rate plateau after the first step, reflecting dynamic Hall-Petch effect, depicts the nucleation of twinning or martensitic transformation as observed elsewhere [32-34]. This microstructural evolution evidence can be noted in **Figure 2.5**.

Strain hardening rate and exponent of the SZ were found to be higher than those of the BM, irrespective of the strain amount (**Figure 2.6 (c)**). In the TRIP assisted deformation, this type of strain hardening behavior is the combination between strain hardening behavior of γ and ε-phases [35]. It is known that the ε-phase is harder than the γ-phase and has higher hardenability. The greater extent of martensitic phase transformation in the SZ compared to the BM can be attributed as the cause of the higher strain hardening in the SZ. The smaller gap in the n value in the later stage of deformation in the SZ specimen indicated the end of the strain-induced martensitic phase transformation, while the n value of the BM started increasing.

2.5 Conclusion

In the present work, a HEA of $Fe_{42}Co_{10}Cr_{15}Mn_{28}Si_5$ composition was investigated through microstructural and mechanical characterization. The following conclusions are drawn from the study:

- The HEA alloy had a dual phase microstructure, mainly consisting of HCP ε-martensite and FCC γ-phase; the volume fraction of each phase can be adjusted by using thermomechanical processing such as FSP.
- After FSP, the alloy underwent discontinuous dynamic recrystallization resulting in fine grained γ-phase. Furthermore, the relative proportion of the two-phase types and the morphology of the ε-martensite changed as a result of FSP. Following FSP, the ε-martensite phase decreased from 52% to 39% because of the existing ε-martensite undergoing complete reversion to the γ phase during FSP and re-formation of ε-martensite just after FSP but not to an extent to reach the previous level.
- Improved room temperature work hardenability in terms of enhanced strain hardening rate and strain hardening exponent is noted after FSP due to the fine recrystallized austenitic structure and modified nature of its TRIP effect.
- Upon room temperature uniaxial compression testing, the ε-martensite proportion in the SZ increased from 39% to 89% whereas the martensitic fraction in the BM increased from 52% to 72%. The SZ is found to have greater susceptibility for the TRIP effect, *i.e.*, ε-martensite formation, than the BM.
- The present study demonstrated that FSP principles ascertained through bead-on-plate configurations may become a successful technique to weld for this type of TRIP HEAs with further studies.

Acknowledgment

This research was funded in part by an Undergraduate Research Grant from the Office of Undergraduate Research at the University of Idaho. Also, Anumat Sittiho would like to acknowledge The Royal Thai Navy for providing him with a graduate scholarship.

References

[1] A.M. Manzoni, U. Glatzel, New multiphase compositionally complex alloys driven by the high entropy alloy approach, Mater. Charact. (2019). https://doi.org/10.1016/j.matchar.2018.06.036.

[2] A. Gali, E.P. George, Tensile properties of high- and medium-entropy alloys, Intermetallics. (2013). https://doi.org/10.1016/j.intermet.2013.03.018.

[3] G. A. Salishchev, M.A. Tikhonovsky, D.G. Shaysultanov, N.D. Stepanov, A. V. Kuznetsov, I. V. Kolodiy, A.S. Tortika, O.N. Senkov, Effect of Mn and v on structure and mechanical properties of high-entropy alloys based on CoCrFeNi system, J. Alloys Compd. (2014). https://doi.org/10.1016/j.jallcom.2013.12.210.

[4] R.O. Ritchie, The conflicts between strength and toughness, Nat. Mater. (2011). https://doi.org/10.1038/nmat3115.

[5] Y. Wei, Y. Li, L. Zhu, Y. Liu, X. Lei, G. Wang, Y. Wu, Z. Mi, J. Liu, H. Wang, H. Gao, Evading the strength-ductility trade-off dilemma in steel through gradient hierarchical nanotwins, Nat. Commun. (2014). https://doi.org/10.1038/ncomms4580.

[6] V. Borovikov, M.I. Mendelev, A.H. King, R. Lesar, Effect of stacking fault energy on mechanism of plastic deformation in nanotwinned FCC metals, Model. Simul. Mater. Sci. Eng. (2015). https://doi.org/10.1088/0965-0393/23/5/055003.

[7] D.T. Pierce, J.A. Jiménez, J. Bentley, D. Raabe, J.E. Wittig, The influence of stacking fault energy on the microstructural and strain-hardening evolution of Fe-Mn-Al-Si steels during tensile deformation, Acta Mater. (2015). https://doi.org/10.1016/j.actamat.2015.08.030.

[8] P.C.J. Gallagher, The influence of alloying, temperature, and related effects on the stacking fault energy, Metall. Trans. (1970). https://doi.org/10.1007/BF03038370.

[9] S. Huang, W. Li, S. Lu, F. Tian, J. Shen, E. Holmström, L. Vitos, Temperature dependent stacking fault energy of FeCrCoNiMn high entropy alloy, Scr. Mater. (2015). https://doi.org/10.1016/j.scriptamat.2015.05.041.

[10] S. Curtze, V.T. Kuokkala, Dependence of tensile deformation behavior of TWIP steels on stacking fault energy, temperature and strain rate, Acta Mater. (2010). https://doi.org/10.1016/j.actamat.2010.05.049.

[11] Z. Nishiyama, Martensitic Transformation, Elsevier Science, Saint Louis, 2014.

[12] F.D. Fischer, G. Reisner, E. Werner, K. Tanaka, G. Cailletaud, T. Antretter, New view on transformation induced plasticity (TRIP), Int. J. Plast. (2000). https://doi.org/10.1016/S0749-6419(99)00078-9.

[13] Z. Li, K.G. Pradeep, Y. Deng, D. Raabe, C.C. Tasan, Metastable high-entropy dual-phase alloys overcome the strength-ductility trade-off, Nature. (2016). https://doi.org/10.1038/nature17981.

[14] Heidarzadeh, A., Mironov, S., Kaibyshev, R., Çam, G., Simar, A., Gerlich, A., Khodabakhshi, F., Mostafaei, A., Field, D. P., Robson, J. D., Deschamps, A., & Withers, P. J. (2020). Friction stir welding/processing of metals and alloys: A comprehensive review on microstructural evolution. In *Progress in Materials Science* (Vol. 117, p. 100752). Elsevier Ltd. https://doi.org/10.1016/j.pmatsci.2020.100752

[15] Meng, X., Huang, Y., Cao, J., Shen, J., & dos Santos, J. F. (2021). Recent progress on control strategies for inherent issues in friction stir welding. In *Progress in Materials Science* (Vol. 115, p. 100706). Elsevier Ltd. https://doi.org/10.1016/j.pmatsci.2020.100706

[16] S.S. Nene, M. Frank, K. Liu, S. Sinha, R.S. Mishra, B. McWilliams, K.C. Cho, Reversed strength-ductility relationship in microstructurally flexible high entropy alloy, Scr. Mater. (2018). https://doi.org/10.1016/j.scriptamat.2018.05.043.

[17] S.S. Nene, M. Frank, K. Liu, R.S. Mishra, B.A. McWilliams, K.C. Cho, Extremely high strength and work hardening ability in a metastable high entropy alloy, Sci. Rep. (2018). https://doi.org/10.1038/s41598-018-28383-0.

[18] S.S. Nene, S. Sinha, M. Frank, K. Liu, R.S. Mishra, B.A. McWilliams, K.C. Cho, Unexpected strength–ductility response in an annealed, metastable, high-entropy alloy, Appl. Mater. Today. (2018). https://doi.org/10.1016/j.apmt.2018.09.002.

[19] A._Jackson, Handbook of crystallography, Springer-Verlag New York, New York, 1991.

[20] Roilett, A. D., & Kocks, U. F. (1993). Title: A Review of the Stages of Work Hardening. In *Proceeding of Dislocations-93 conference at Aussois, France, 1-9 Apr 1993*. Los Alamos National Laboratory. https://digital.library.unt.edu/ark:/67531/metadc1342227/

[21]_K. Huang, R.E. Logé, A review of dynamic recrystallization phenomena in metallic materials, Mater. Des. (2016). https://doi.org/10.1016/j.matdes.2016.09.012.

[22] F. Humphreys, Recrystallization and Related Annealing Phenomena. Elsevier, 2017.

[23] D.G. Brandon, The structure of high-angle grain boundaries, Acta Metall. (1966). https://doi.org/10.1016/0001-6160(66)90168-4.

[24] H. Shoji, Geometric relationships among the structures of modifications of a substance. Kristallogr. (1931).

[25] C. Zener, J.H. Hollomon, Effect of strain rate upon plastic flow of steel, J. Appl. Phys. 15 (1944) 22–32. https://doi.org/10.1063/1.1707363.

[26] C.I. Chang, C.J. Lee, J.C. Huang, Relationship between grain size and Zener-Holloman parameter during friction stir processing in AZ31 Mg alloys, Scr. Mater. (2004). https://doi.org/10.1016/j.scriptamat.2004.05.043.

[27] S. Takaki, H. Nakatsu, Y. Tokunaga, Effects of austenite grain size on ε martensitic transformation in Fe-15mass%Mn alloy, Mater. Trans. JIM. (1993). https://doi.org/10.2320/matertrans1989.34.489.

[28] K. Rajan, J.B. Vander Sande, Room temperature strengthening mechanisms in a Co-Cr-Mo-C alloy, J. Mater. Sci. (1982). https://doi.org/10.1007/BF00540374.

[29] A. Arora, Z. Zhang, A. De, T. DebRoy, Strains and strain rates during friction stir welding, Scr. Mater. (2009). https://doi.org/10.1016/j.scriptamat.2009.07.015.

[30] Y. Morisada, H. Fujii, Y. Kawahito, K. Nakata, M. Tanaka, Three-dimensional visualization of material flow during friction stir welding by two pairs of X-ray transmission systems, Scr. Mater. (2011). https://doi.org/10.1016/j.scriptamat.2011.09.021.

[31] Y.W. Cheng, R.L. Tobler, B.J. Filla, K.J. Coakley, Constitutive behavior modeling of steels under hot-rolling conditions. NIST Technical Note 1500-6, Washington, 1999.

[32] C. Celada-Casero, H. Kooiker, M. Groen, J. Post, D. San-Martin, In-situ investigation of strain-induced martensitic transformation kinetics in an austenitic stainless steel by inductive measurements, Metals (Basel). (2017). https://doi.org/10.3390/met7070271.

[33] E. El-Danaf, S.R. Kalidindi, R.D. Doherty, Influence of grain size and stacking-fault energy on deformation twinning in fcc metals, Metall. Mater. Trans. A Phys. Metall. Mater. Sci. (1999). https://doi.org/10.1007/s11661-999-0272-9.

[34] C. Celada-Casero, J. Sietsma, M.J. Santofimia, The role of the austenite grain size in the martensitic transformation in low carbon steels, Mater. Des. (2019). https://doi.org/10.1016/j.matdes.2019.107625.

[35] W.J. Dan, S.H. Li, W.G. Zhang, Z.Q. Lin, The effect of strain-induced martensitic transformation on mechanical properties of TRIP steel, Mater. Des. (2008). https://doi.org/10.1016/j.matdes.2007.02.019.

Chapter 3: Weldability of $Fe_{42}Co_{10}Cr_{15}Mn_{28}Si_5$ High Entropy Alloys by Pressure Resistance Welding Technique

Abstract

Pressure resistance welding (PRW) is applied to conduct PRW weldability of the TRIP HEA $Fe_{48}Co_{10}Cr_{15}Mn_{28}Si_5$. The weld parameters are varied to prototype the welding parameter on this type of material. The microstructural analyses utilizing optical microscopy and scanning electron microscopy are conducted to evaluate the quality of the weld in the TRIP HEA. The finite element analysis using the electro-thermo-mechanical analysis model is created for visualizing the heat generation and material behavior during the PRW process. The result of the weld depends on the time and the amount of heat generated by the current applied in the coupon. The microstructure of the successful PRWed specimen shows recrystallized microstructure. However, the Vickers microhardness test does not detect a significant change in the material property throughout the weld cross-section.

3.1 Introduction

High entropy alloy (HEA) is an emerging type of metallic alloy that comprises 5 or more near equimolar elements. The concept of using the HEA was proposed by J. W. Yeh and Cantor [1, 2]. After the time of their discovery, the HEAs gain tremendous interest for their excellent properties, *e.g.*, high fracture toughness, corrosion resistance, exceptional cryogenic behavior [3-6].

$Fe_{42}Co_{10}Cr_{15}Mn_{28}Si_5$ is one of the outstanding HEA for the accident tolerated application since it shows the phase tunability by having an unstable FCC phase which, under deformation, undergoes a martensitic transformation that greatly increases strain hardening of the alloy. This feature makes this HEA overcame the strength ductility trade-off in the metallic alloy [7-11]. This behavior of the TRIP HEA makes this alloy a prospective material for accidental tolerates material.

Despite this HEA shows the novel capability, the HEA is still immature in industrial applications. there is limited research on the weldability of this alloy [12]. Joining alloy by using the fusion welding method has been known for the compromise of the alloy’s strength [13]. Pressure resistant welding (PRW) is a solid-state welding technique where two specimens are joined by the effect of Joule heating. The technique is adapted from resistance welding which is widely used in the automotive industry because of the quick and autonomous nature of the process. Kanne [14] reported the advantage of the PRW in joining non-weldable alloys. PRW is typically chosen for welding of high-temperature materials and dispersion strengthened materials because of the benefit of the no-melting joining process [15, 16].

This work aims to attempt applying pressure resistance welding on this $Fe_{42}Co_{10}Cr_{15}Mn_{28}Si_5$ and determine the initial welding schedule. The microstructure of the PRWed will also be discussed to correlate to the effect of the PRW process on the microstructural evolution governing the mechanical properties outcome.

3.2 Experimental procedure

TRIP HEA having a chemical composition of $Fe_{42}Co_{10}Cr_{15}Mn_{28}Si_5$ was procured from Sophisticated Alloys, Inc, Butler, PA. The alloy then was made into a coupon of two different sizes as depicted in **Figure 3.1**. Welding coupon surfaces were prepared by grinding with SiC paper down to 1200 um and then polished with 1um slurry alumina. Then welding coupons were weld using the Voltza® Transgun procured from the Centerline Ltd. with the capability of producing 5340 N of the forging force and 30 kA current. The weld time is control by varying cycles, based on 60 cycles per second, one cycle is 16.7 ms. There are 3 PRW weld programs used in this study namely, set current and time function, current slope function, and current impulse function. The current and force chart between each of the welding programs are shown in **Figure 3.2**. After the welding, the specimens were prepared for metallographic study and Vickers microhardness testing. The welded specimens were grinded with SiC paper down to 1200 grit and then polished with slurry alumina down to 0.3 µm. Vickers microhardness test was done using the load of 200gf and indentation interval of 0.254 mm (1/100 in). The etching process prior to optical metallography was done by using aqua regia etchant (HNO_3:HCl = 1:3 by volume). After the PRW is done the finite element analysis (FEA) model was made by ABAQUS™ software (student edition) by using thermo-electro-mechanical couple analysis.

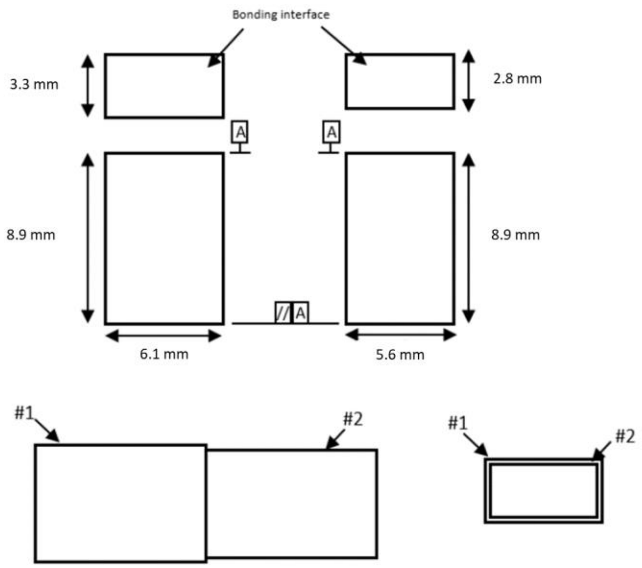

Figure 3.1. Drawing of the designed PRW coupons adapted from [13].

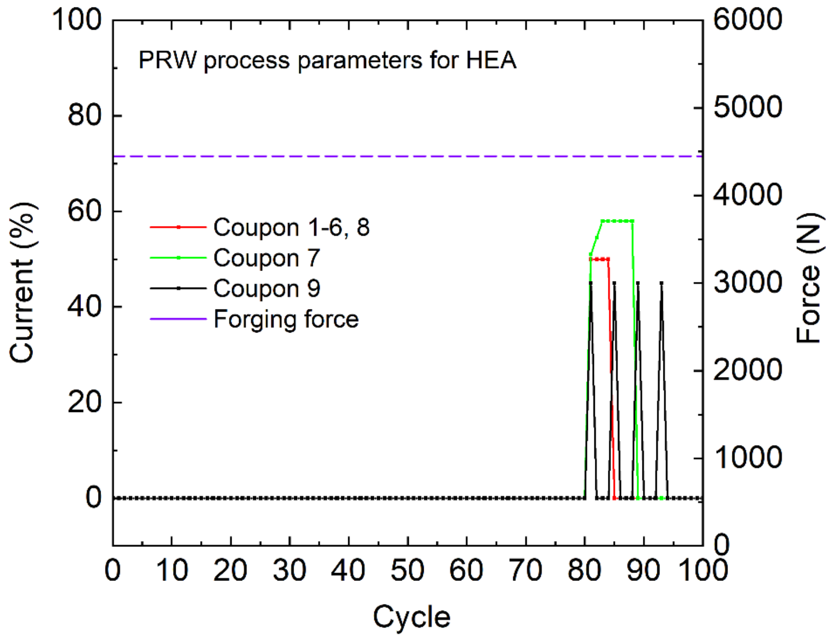

Figure 3.2. PRW process parameters schematics used in this work

Table 3.1. PRW parameters for each specimen

Specimen	**Cycles**	**Current rate (%)**	**Remarks**
1	3	57	Good
2	3	44	Bad
3	3	50	Bad
4	3	50	Bad
5	2	57	Bad
6	4	50	Good
7	3	51-58	Current slope function, Good
8	4	44	Good
9	4	51	Impulse function, Bad

After the PRW is done the finite element analysis (FEA) model was made by ABAQUS™ software (student edition) by using thermo-electro-mechanical couple analysis. The model parameters and material properties are listed in Table 3.2

Table 3.2. Material parameter used in the calculation

Parameter	Value	Unit
Density	7680	kg/m^3
Elastic modulus	198.9	GPa
Thermal Conductivity	100	W/m·K
Electrical conductivity	1450	S/m
Specific heat	0.5	J/K
Yield strength at 21^{o}C	320	MPa
Yield strength at 400^{o}C	200	MPa
Yield strength at 800^{o}C	100	MPa
Yield strength at 1000^{o}C	60	MPa
Joule’s heat fraction	1	
Contact electrical conductivity	60×10^{-6}	Ω
Contact pressure	285	MPa

3.3 Results and Discussion

After the PRW, all of the specimens were successfully attached. The deformation predominantly on the smaller coupon side. There is a flash formation in the specimens 1, 4, 6, 7, and 8. The microstructure under the optical micrograph displays the microstructure of the welded coupon. The PRWed coupons excessive flash results in the recrystallized grain structure with the weld zone width are about 400 μm in specimens 1, 6, 7, 8. Specimen 4, despite showing some amount of flash formation, does not produce a complete weld. The rest of the specimens do not have flash formation after weld. These specimens' microstructure appears to have an unwelded line in the center of the weld with discontinuity of the microstructure between both sides of the weld as seen in **Figure 3.3 (b, c, d, e, and i)**.

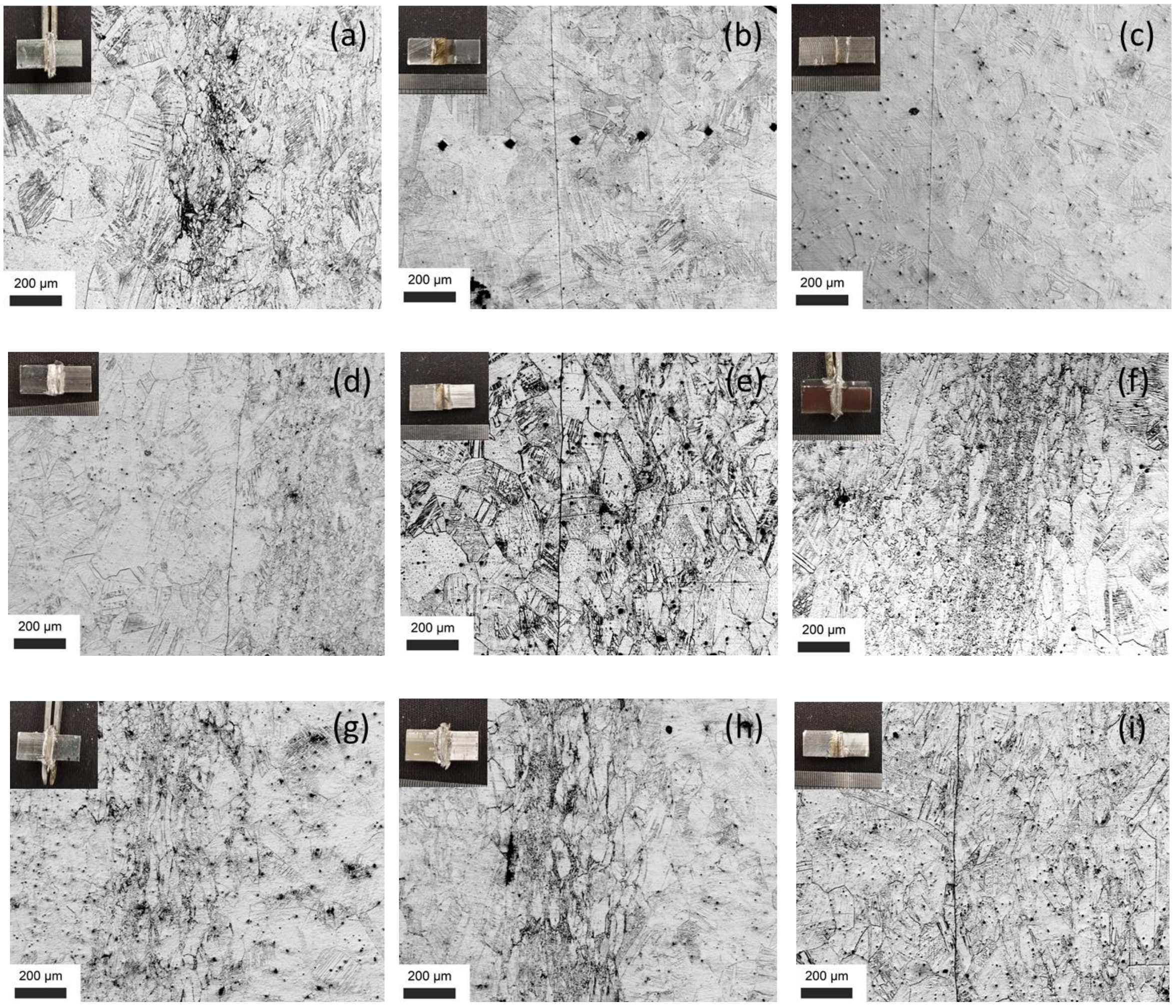

Figure 3.3. (a) to (i) The weld interface images of PRWed TRIP HEA form PRWed coupon 1 to 9, respectively. Note that the larger weld-coupon is on the left side of the images as seen from the macro images inset.

The backscattered SEM images reveal the presence of ε-martensite plate inside γ-grain in the based metal (BM) appearing as the band contrast. The microstructure in the weld depicts the recrystallized grain with small ε-phase band contrast and the presence of annealing twins. However, the amount of ε-martensite phase decreases drastically. This is likely the result of high temperature, high strain rate process such as PRW.

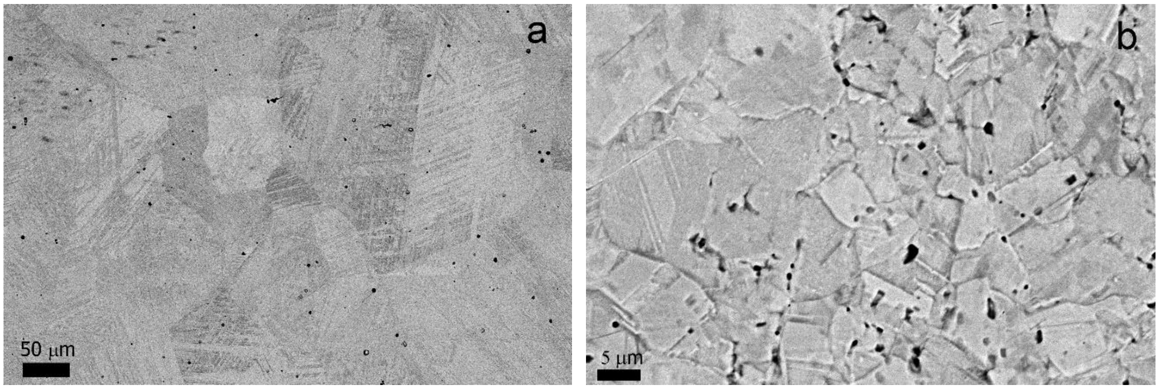

Figure 3.4. The SEM backscattered electron image reveals the microstructure of the (a) based metal and (b) welded zone specimen.

The effect of PRW parameters on the success of the weld is shown in **Figure 3.5.** As constant forging force is used in this work, the effect of the current and the weld time can be understood. The heat generation in the PRW process comes from Joule heating given the high resistance at the butting interface and the current passed as written in **Equation 3.1**.

$$H = I^2 \cdot R \cdot t \qquad (3.1)$$

where H is the total heat input (in J), I is the current (in A), R is resistance on the weld coupon at the contact (in Ω), and t is the welding duration (in s). The dashed line on the plot roughly shows the heat input threshold to produce sound weld on this HEA at 4450 N forging force. The forging force and weld surface roughness affect the resistance (R) value in Equation 3.1. In this work, all the PRW coupons were prepared in the same fashion. The surface roughness, hence, is assumed to be the same for all the specimens. The resistivity value at the interface is measured to be 60 μΩ on average. Then, the calculated heat input minimum threshold is 810 J.

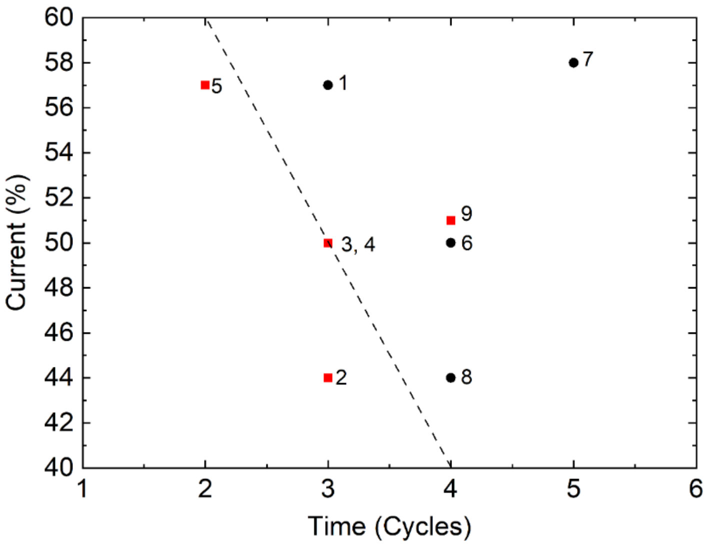

Figure 3.5. Effect of PRW parameters on the quality of the weld. Black circles represent the sound welded specimens while the red squares are the failed to weld specimens. The numbers next to the spot are specimen numbers.

The $Fe_{42}Co_{10}Cr_{15}Mn_{28}Si_5$ is TRIP-assisted HEA, *i.e.*, under the deformation, strain-induced gamma to epsilon phase transformation taking place. The PRW process is solid-state welding that affects the welded coupon on both temperature and strain, causing the weld joint to recrystallize. The strength of the PRWed HEA is displayed by using Vickers microhardness. Vickers microhardness indentation results from each specimen are compiled in **Figure 3.6**. There is no discernable hardness difference along the cross-section of the weld despite having a smaller grain size (50 µm) compared to that of the base metal (200 µm). This occurrence is because of the effect of the martensitic phase present in the base metal but not in the weld to the same extent. However, the smaller grain size leading to the Hall-Petch strengthening may be counteracting the loss of martensite strengthening at the weld joint and keeping the hardness change across the joint not significant.

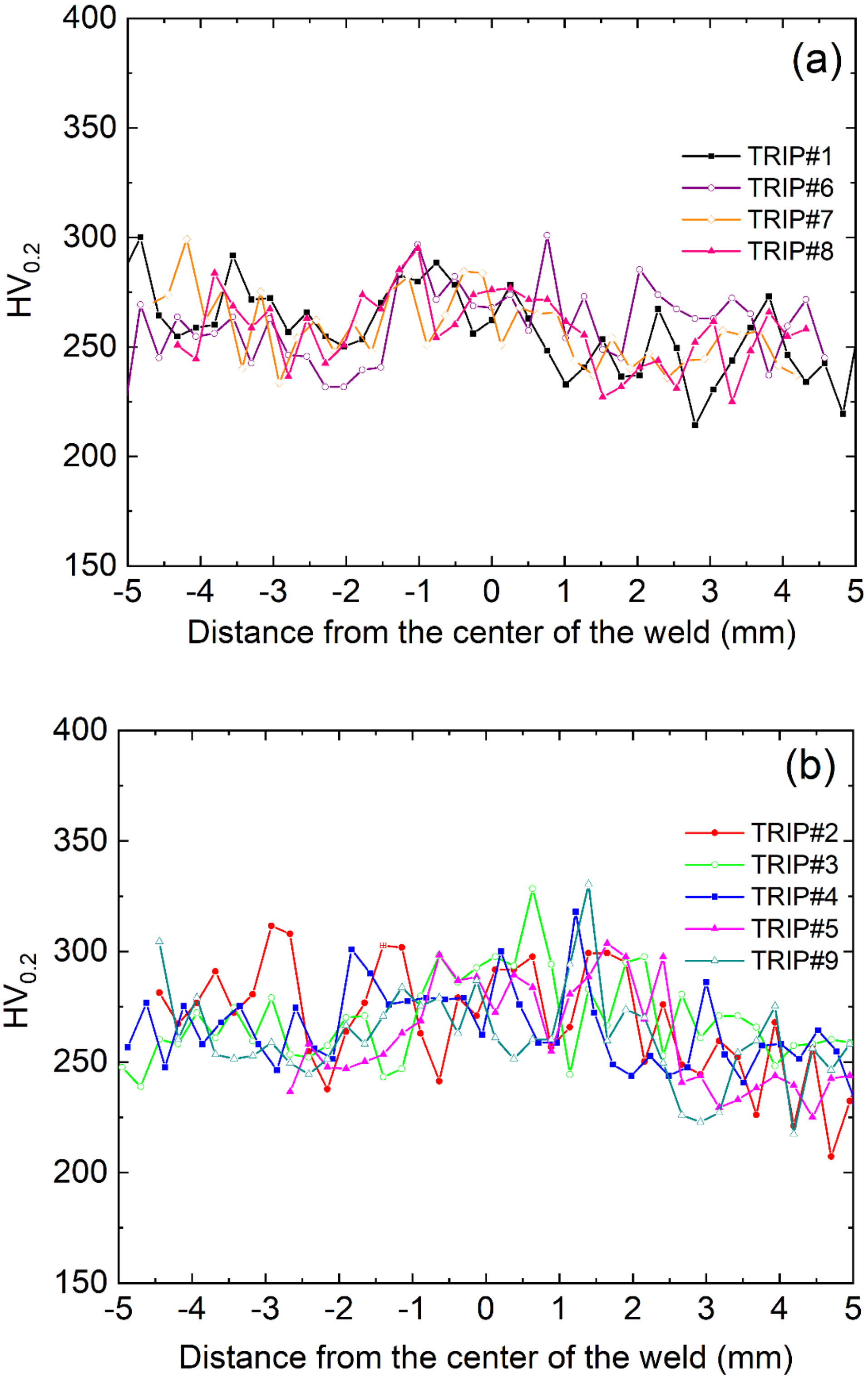

Figure 3.6. Vickers hardness across the weld of the PRWed coupon that is (a) successful weld and (b) failed to weld.

The finite element model was calculated using PRW parameters from specimen 6. The material parameters used in the calculation are listed in **Table 3.2**. The results in **Figure 3.7** show that the heat and deformation distribution is mainly concentrated on the smaller coupon side.

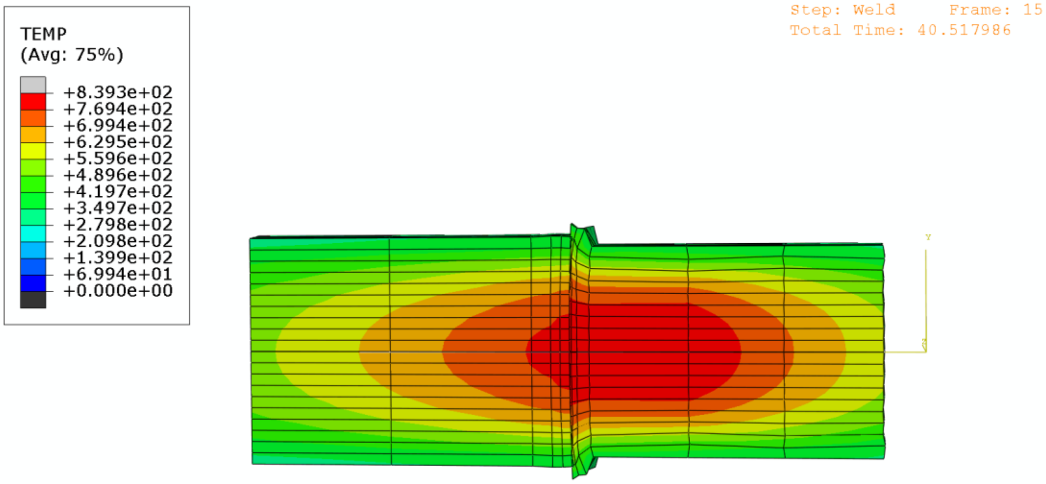

Figure 3.7. Finite element analysis from quarter symmetry model showing the parallel cut from the weld coupon. The heat generation and deformation during the weld concentrate on the small weld coupon side during the PRW process.

3.4 Conclusion

From the preceding study, the following conclusions can be drawn:

1. The PRW produced sound welds in the $Fe_{42}Co_{10}Cr_{15}Mn_{28}Si_5$ with no loss of strength in the alloy, *i.e.*, having close to 100% weld efficiency.

2. The minimum heat input threshold for producing a sound weld is calculated to be 810 J.

3. The transformative nature of this alloy helps preserve the strength of the HEA after PRW.

4. FEA model reveals the majority of heat distribution and deformation are concentrated in the smaller weld coupon.

Acknowledgment

Anumat Sittiho would like to thank The Royal Thai Navy for financial support for his graduate study.

References

[1] Yeh, J. W., Chen, S. K., Lin, S. J., Gan, J. Y., Chin, T. S., Shun, T. T., Tsau, C. H., & Chang, S. Y. (2004). Nanostructured high-entropy alloys with multiple principal elements: Novel alloy design concepts and outcomes. *Advanced Engineering Materials*, *6*(5), 299-303+274. https://doi.org/10.1002/adem.200300567

[2] Cantor, B., Chang, I. T. H., Knight, P., & Vincent, A. J. B. (2004). Microstructural development in equiatomic multicomponent alloys. *Materials Science and Engineering A*. https://doi.org/10.1016/j.msea.2003.10.257

[3] Li, Z., Pradeep, K. G., Deng, Y., Raabe, D., & Tasan, C. C. (2016). Metastable high-entropy dual-phase alloys overcome the strength-ductility trade-off. *Nature*. https://doi.org/10.1038/nature17981

[4] Miracle, D. B., & Senkov, O. N. (2017). A critical review of high entropy alloys and related concepts. In *Acta Materialia*. https://doi.org/10.1016/j.actamat.2016.08.081

[5] Tsai, M. H., & Yeh, J. W. (2014). High-entropy alloys: A critical review. *Materials Research Letters*. https://doi.org/10.1080/21663831.2014.912690

[6] Zhang, C., Zhu, C., Harrington, T., Casalena, L., Wang, H., Shin, S., & Vecchio, K. S. (2019). Multifunctional Non-Equiatomic High Entropy Alloys with Superelastic, High Damping, and Excellent Cryogenic Properties. *Advanced Engineering Materials*. https://doi.org/10.1002/adem.201800941

[7] Ritchie, R. O. (2011). The conflicts between strength and toughness. *Nature Materials*. https://doi.org/10.1038/nmat3115

[8] Nene, S. S., Frank, M., Liu, K., Sinha, S., Mishra, R. S., McWilliams, B., & Cho, K. C. (2018). Reversed strength-ductility relationship in microstructurally flexible high entropy alloy. *Scripta Materialia*. https://doi.org/10.1016/j.scriptamat.2018.05.043

[9] Mishra, R. S., Nene, S. S., Frank, M., Sinha, S., Liu, K., & Shukla, S. (2020). Metastability driven hierarchical microstructural engineering: Overview of mechanical properties of metastable complex concentrated alloys. *Journal of Alloys and Compounds*. https://doi.org/10.1016/j.jallcom.2020.155625

[10] Nene, S. S., Sinha, S., Frank, M., Liu, K., Mishra, R. S., McWilliams, B. A., & Cho, K. C. (2018). Unexpected strength–ductility response in an annealed, metastable, high-entropy alloy. *Applied Materials Today*. https://doi.org/10.1016/j.apmt.2018.09.002

[11] Nene, S. S., Frank, M., Liu, K., Mishra, R. S., McWilliams, B. A., & Cho, K. C. (2018). Extremely high strength and work hardening ability in a metastable high entropy alloy. *Scientific Reports*. https://doi.org/10.1038/s41598-018-28383-0

[12] Heidarzadeh, A., Mironov, S., Kaibyshev, R., Çam, G., Simar, A., Gerlich, A., Khodabakhshi, F., Mostafaei, A., Field, D. P., Robson, J. D., Deschamps, A., & Withers, P. J. (2020). Friction stir welding/processing of metals and alloys: A comprehensive review on microstructural evolution. In *Progress in Materials Science* (Vol. 117, p. 100752). Elsevier Ltd. https://doi.org/10.1016/j.pmatsci.2020.100752

[13] Wu, Z., David, S. A., Leonard, D. N., Feng, Z., & Bei, H. (2018). Microstructures and mechanical properties of a welded CoCrFeMnNi high-entropy alloy. *Science and Technology of Welding and Joining*. https://doi.org/10.1080/13621718.2018.1430114

[14] Kanne, Jr, W R. *Solid-state resistance upset welding: A process with unique advantages for advanced materials*. United States.

[15] Jerred, N., Zirker, L., Jaques, B., Bradshaw, T., Carrillo, J., Young, E., Charit, I., Cole, J., Frary, M., Butt, D., Meyer, M., & Murty, K. L. (2010). *Pressure Resistance Welding of High Temperature Metallic Materials MS&T 2010 Pressure Resistance Welding of High Temperature Metallic Materials*.

[16] Seki, M., Hirako, K., Kono, S., Kihara, Y., Kaito, T., & Ukai, S. (2004). Pressurized resistance welding technology development in 9Cr-ODS martensitic steels. *Journal of Nuclear Materials*, *329–333*(1-3 PART B), 1534–1538. https://doi.org/10.1016/j.jnucmat.2004.04.172

[17] Instasi, S. M. (2018). *Solid-State Joining of Molybdenum Based Materials via Pressure Resistance Welding* (Master of Science). The University of Idah.

Chapter 4: Mechanical Properties and Deformation Mechanism Study of $Al_{0.4}CoCrFeNi$ High Entropy Alloy

Abstract

High entropy alloy (HEA) is gaining attention on recent research topics because of its promising mechanical properties. In this study, a HEA, having chemical composition $Al_{0.4}CoCrFeNi$, produced by casting is investigated for studying the mechanical behavior and the microstructure relationship. Bulk compression testing and micropillar compression testing were used to study the mechanical behavior of the alloy. Electron microscopy techniques *i.e.*, SEM (scanning electron microscopy) and TEM (transmission electron microscopy) were used for characterizing changes between as cast and deformed specimens. This alloy shows that the dislocation structure evolves from perfect glide to microband as the strain magnitude increases. The intrinsic deformation twin of this alloy is then studied by using micropillar compression testing. The results exhibit distinct behavior between [001] and [111] oriented micropillar that the compressive yield strength in [001] oriented micropillar is smaller than that of [111] oriented micropillar (320 MPa vs 570 MPa). The critical resolve shear stress

4.1 Introduction

High entropy alloy (HEA) is an emerging class of metallic materials made of five or more major alloying elements. The concept of utilizing multicomponent for the alloys was introduced in the same year by Yeh and Cantor [1][2]. Later, these equiatomic multicomponent alloys were known as high entropy alloys because of their inherent high configurational entropy ($S_{config} > 1.6R$), where R is the gas constant. This high entropy affects the alloys by mitigating their intermetallic phases formation. As a result, HEAs exhibit single-phase disordered solid solution microstructure. These HEAs are found to have crystal structures of BCC, FCC, or HCP types [3-7]. However, due to the complexity of compositions in the HEAs, the production of single-phase solid solution HEA is rather difficult [8]. Despite not having a single-phase solid solution microstructure, the HEAs exploit the heterogeneous microstructure to obtain more favorable mechanical properties from their duplex structure or metastable phases [8-15].

Mechanical properties of HEAs are somewhat predictable like that of the conventional alloy as they follow the crystallographic behavior. For instance, the BCC HEAs are expected to have higher strength but lower ductility compared to that of the FCC HEAs. The FCC HEAs, even though having lower yield strength, often have higher ductility so they are a decent option for accidental tolerated applications. One of the examples is the CoCrNi medium entropy alloy that shows the tensile strength of 760 MPa and ductility of 73.2%. [16]. The CoCrFeNi HEA has a tensile strength of 400 MPa and ductility of 45% [17]. This excellent strength ductility combination is attributed to the stacking fault energy (SFE) and the deformation-induced phase transformation, *i.e.*, twinning induced plasticity (TWIP) and/or transformation induced plasticity (TRIP) [18-22].

Phase tunability is observed in the HEAs with the $Al_xCoCrFeNi$ compositions. The amount of Al determines the stable phase of the systems. The HEAs exhibit FCC phase when $x \leq 0.3$, BCC+FCC phases when x is in the range of 0.5 to 0.7, and a single BCC phase when x is greater than 0.7 [15]. The exploration of the mechanical properties of $Al_xCoCrFeNi$ HEAs was done on several different Al content as displayed in **Figure 4.1**. $Al_{0.1}CoCrFeNi$ is shown to have good ductility with relatively low strength (YS = 180 UTS = 320 MPa) which improved by grain refinement through friction stir processing (FSP) technique. The grain refinement increases YS to 320 MPa and UTS to 620 MPa. This alloy shows to have a good Hall-Petch coefficient value of 824 $MPa \cdot \mu m^{-0.5}$[18]. The $Al_{0.3}CoCrFeNi$ HEA shows deformation twin when underwent high-velocity deformation with the yield strength around 200 MPa [19, 20]. The deformation twin is favorable because it gives the exceptional high work hardenability of the alloy, *i.e.*, strain hardening rate greater than 1500 MPa. For $Al_{0.5}CoCrFeNi$, the yield strength of the alloy is significantly different from that of $Al_{0.3}CoCrFeNi$ HEA. The tensile yield strength of 420 MPa with 10% elongation on fracture [11].

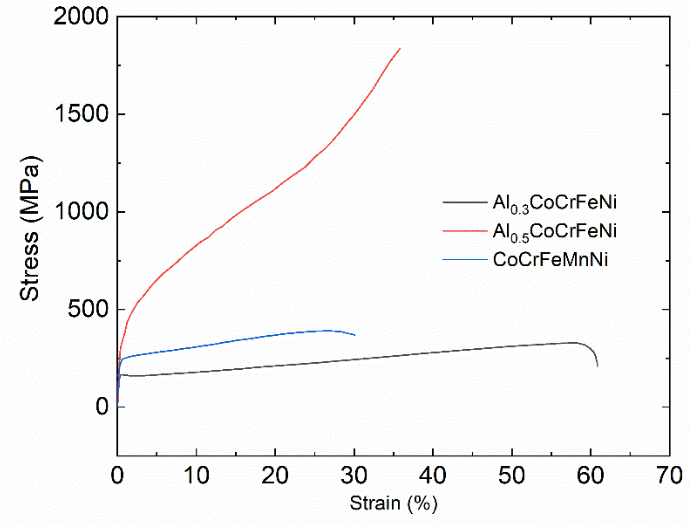

Figure 4.1. Comparative mechanical behaviors of some relevant HEAs [11, 17, 20].

The study of the plasticity of the HEA helps understand the behaviors of the alloy. The discovery of the TWIP and TRIP effect on the $Al_xCoCrFeNi$ [11-14, 21, 22] sparks the intriguing on the mechanisms of the phenomenon. The technique that is suitable to explore this occurring is micropillar compression testing as the loading direction is known and the deformation system can be predicted. In FCC metals, the deformation of the crystal is well defined to be on the <011>{111} systems.

The objective of this paper is to examine the mechanical behaviors and deformation behaviors under compression load via correlation with dislocation evolution in the $Al_{0.4}$CoCrFeNi HEA at room temperature and study the micromechanical behavior of the alloy by using micropillar compression testing for observing the micromechanical behavior in different crystal orientations.

4.2 Experimental procedures

The $Al_{0.4}$CoCrFeNi cast block with the dimension of 75×75×20 mm was produced by vacuum arc casting vacuum arc-casting under inert argon atmosphere at Sophisticated Alloys Inc., Butler, PA, USA. The as-casted specimen (AC) microstructure was examined by using an optical micrograph and electron microscope.

4.2.1 Microstructural examination

To study the microstructure of the HEA, the alloy was grinded with SiC paper down to 1200 grit followed by polishing with 1 µm and 0.5 µm slurry alumina. The chemical etching was done using aqua regia etchant which is the mixture of nitric acid and methanol in 1:3 parts by volume. Afterward, the etched specimen was examined using optical microscopy (Olympus PGM-3) and scanning electron microscopy (Zeiss supra) equipped with energy-dispersive x-ray spectroscopy (EDS). Transmission microscopy specimen were prepared by mechanical grinding down to the thickness between 50 – 100 µm. Then, 3 mm diameter discs were punched from the thin foil. Then, the discs were made electron transparent by electro twin jet polishing method in the 10 % Nital solution (10% Nitric acid and 90% Methanol by volume) at the temperature of -40°C. The voltage used during the electrojet polishing was 30V. Finally, the electro-polished specimens were cleaned by using Gatan PIPsII^{TM} ion polishing system.

4.2.2 Focused ion beam micropillar fabrication and micropillar compression testing

The micropillars were fabricated by using the focused ion beam milling method. Before the focused ion beam (FIB) milling, a specimen was mapped for its crystallographic orientation by using the electron backscatter diffraction (EBSD) technique. After the crystal orientations are known, the FIBing was conducted in the FEI QUANTA 3D FEG equipped with EBSD. Then, 2 micropillars were milled from each [001] and [111] oriented direction which represented soft and hard orientations. These micropillars had a cuboidal shape with the lateral dimension of 10 x 10 µm and the height was 2 to 2.5 times the lateral dimensions. The micropillar design dimension of 10 µm was designed to minimize the size effect that makes the micropillar having excessively stronger compared to the bulk compression testing due to the defect source scarcity [23]. This micropillar geometry aspect ratio is used elsewhere to minimize the size effect of the micropillar on the mechanical properties [24].

4.2.3 Bulk uniaxial compression testing

Bulk uniaxial compression testing specimens were prepared to have a cylindrical shape with a diameter of 4 mm and a height of 6 mm. This diameter to height ratio was designed following the ASTM E9 standard for metallic compression testing. The instrument used for the test was Instron 5982 universal testing frame with a load capacity of 100 kN. During the test, a boron nitride lubricant was applied to minimize the friction between compression fixtures and the specimens. The compression tests were done at different strain rates, for observing the material responses to the various strain rates, ranging from 10^{-4} to 10^{-2} s^{-1}.

Micropillar compression testing was done on the Hysitron SEM Picoindenter system^{TM}. After the indentation, the corrections for the system compliance and micropillar Hysitron software, running on the OriginPro^{TM}, to observe the in situ micro compression analysis and the system compliances correction [25, 26].

4.3 Results

4.3.1 Microstructure of the as-cast block

The as-cast (AR) microstructures of the $Al_{0.4}CoCrFeNi$ comprises columnar grain with dendritic structure that resembles the conventional cast microstructures of metallic alloys. The average secondary dendritic arm distance is 21±1 um. The grain size of the AR specimen is greater than 200 µm. There is obvious localized phase segregation, seen as a dark spot, in the interdendritic area from Figure 2(a). Phase analysis by SEM EDS indicates the phase segregates to be NiAl (B2) phase. The chemical compositions of the HEA matrix and the segregate are shown in *Table I*. However, the matrix shows superlattice diffraction from selected area electron diffraction (SAED). The SEAD index shows that the crystallographic relationship between FCC matrix and B2 precipitates is $[001]_{FCC}$ // $[001]_{BCC}$.

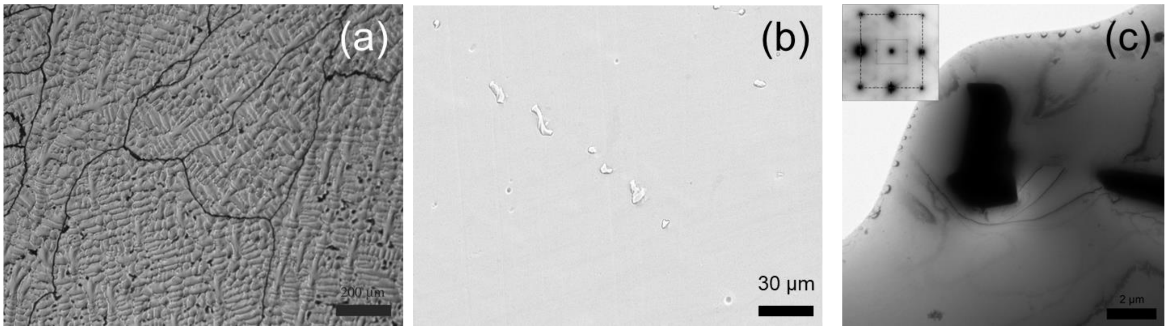

Figure 4.2. Microstructure of the AR specimen taken via (a) optical microscopy, (b) SEM secondary electron image, and (c) TEM at B=[001] with SEAD inset.

Table 4.1. Chemical composition in atomic % of the as cast block.

Elements	Co	Cr	Fe	Ni	Al
Matrix	21.1	23	24.2	21.4	10.3
Segregates	15.2	7.5	9.9	32.3	35.1

4.3.2 Mechanical behavior of $Al_{0.4}CoCrFeNi$ HEA

The room temperature compressive mechanical behavior of the HEA up to 28% strain is shown in **Figure 4.3(a)**. The yield strength at 0.002 strain is 320 MPa. S-Shape strain hardening curve is observed. The strain hardening rate of the alloy is ranging from 1500 MPa to 3500 MPa.

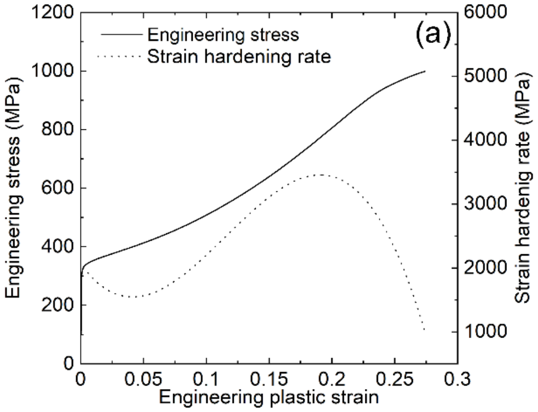

Figure 4.3. Room temperature mechanical behavior of the alloy under room temperature uniaxial compression test at 10^{-3} s^{-1}

Micropillar compression testing mechanical behavior is shown in **Figure 4.4**. The alloy shows anisotropic behavior between [001] and [111] compressed micropillar. The [001] oriented micropillar has some discrepancy in yields strength between those 2 compression tests. The average yield strength of those [001] oriented micropillars is 327 ± 60 MPa. Nonetheless, the [111] oriented micropillar has more consistent yield strength with an average of 520 ± 16 MPa.

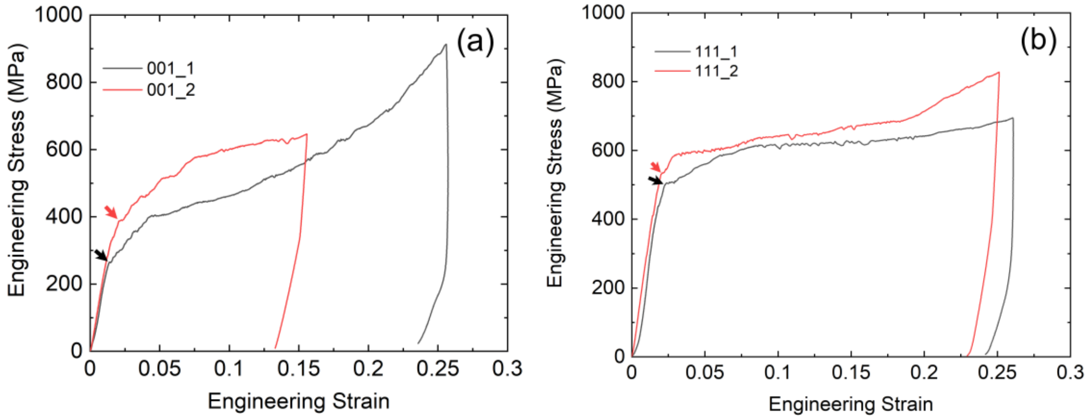

Figure 4.4. Micropillar compression engineering stress-strain curves of 2 micropillars each from (a) [001] and (b) [111] oriented micropillars.

4.3.3 Microstructure evolution during uniaxial compression

After deformation, the alloy shows the dislocation evolution progression through various strain levels. At 3% strain, the perfect dislocation glide with mixing planar and wavy dislocation characteristics dominates the plasticity. Dislocation loops and dipoles can be observed at this strain level. At 10% strain, the perfect dislocation glide with the majority planar glide characteristic dominates the plasticity. Dislocation bands start forming at this level. At 24% strain, the microbands form and store a lot of dislocation inside those bands. The density of the dislocation band is higher compared to the 10% strain. Those microstructural evolutions are shown in **Figure 4.5**.

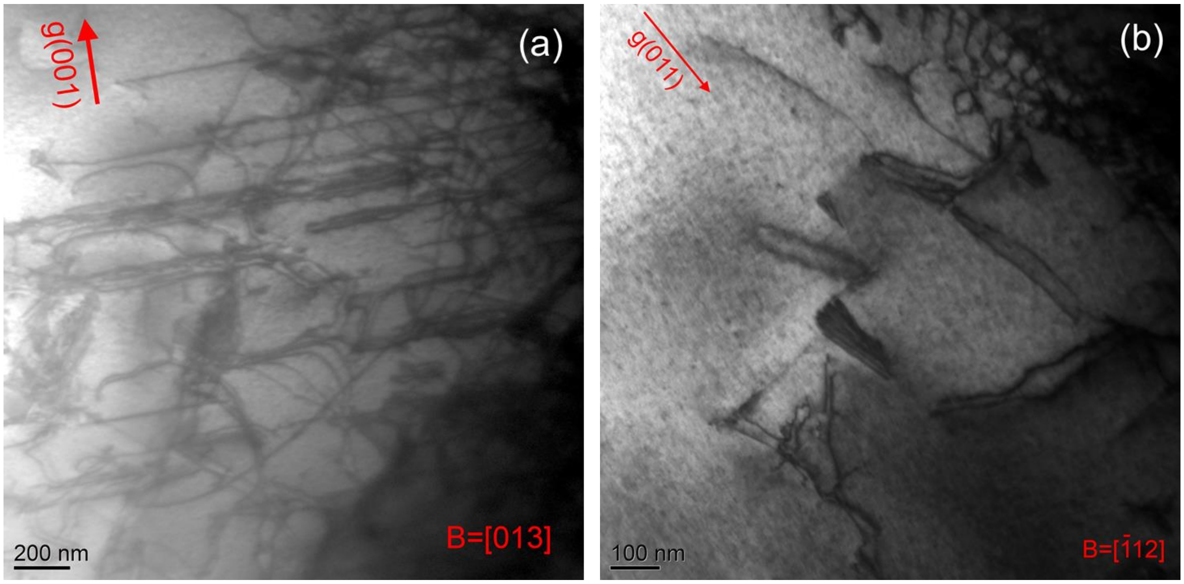

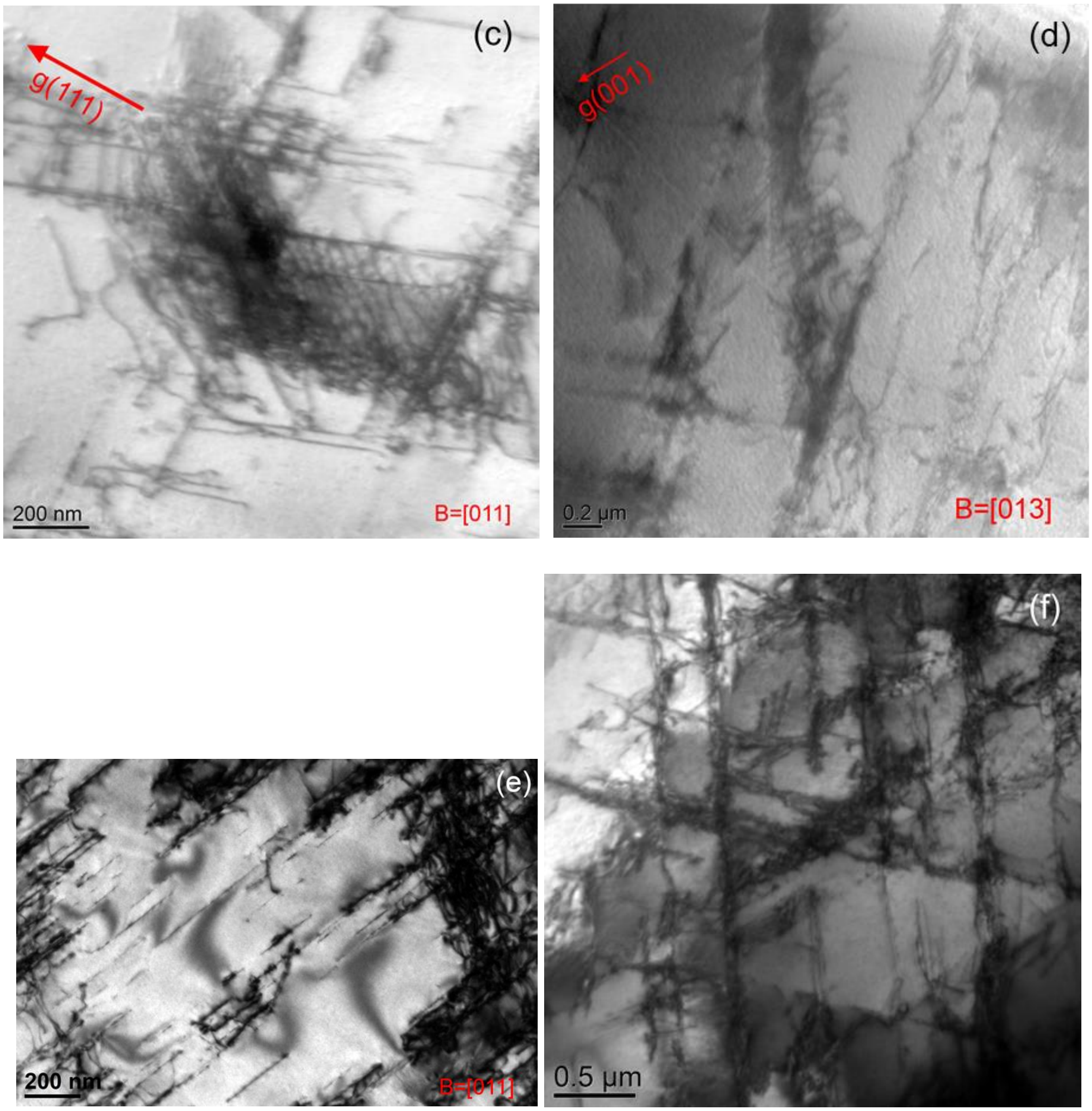

Figure 4.5. Dislocation structure evolution at the different strain levels. At ε= 3% (a, b), the perfect dislocation glide shows the wavy and planar dislocation structure with some dislocation cells. Individual stacking faults form in the specimen. At ε= 10% (c, d), extended dislocation dipoles, lying perpendicular to g=<111> forms microbands boundaries that contain dislocation train in between them. At ε= 24% (e, f), microbands become denser and start form dislocation cells.

Moire fringes image analysis with the fast furrier transformed of the image inset was conducted to study the detailed microstructure in the 24% deformed specimen. The band boundaries, appearing as black lines, contains high dislocation densities in between them as seen in **Figure 4.6 (a)**. Small SRO phase, observed in **Figure 4.6 (b)**, having size of 3 nm is also detected using the technique along with the formation of dislocation loop.

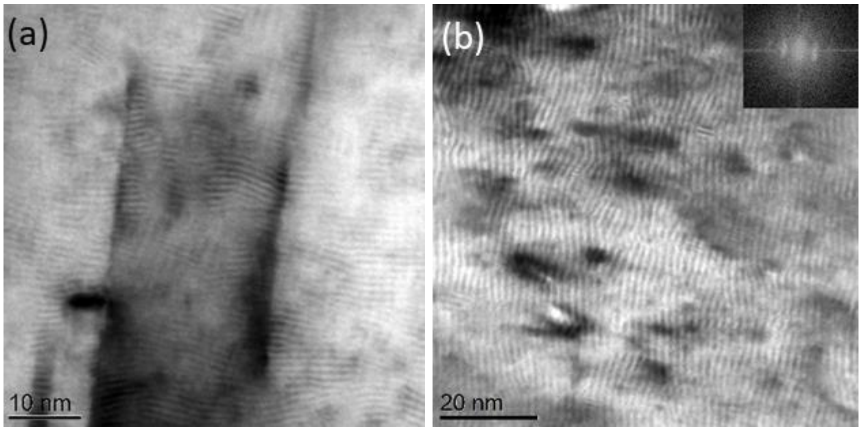

Figure 4.6. Moiré fringe images from 10% deformed specimen show the presence of **(a)** high dislocation density in between the microbands boundaries and **(b)** 3 nm size precipitates.

4.3.4 Microstructure of deformed micropillars

Micropillar for both orientations shows uniform deformation during compression. The [001] oriented micropillar slip trace exhibits 56° from the loading axis while the [111] oriented micropillar shows 45° as shown in **Figure 4.7**. The corresponding TEM images of the deformed micropillars are shown in **Figure 4.8**. In the deformed [001] oriented micropillar, the planar dislocation dominated the plasticity. While in the [111] oriented micropillar, dislocation moves downwards parallel to the loading axis.

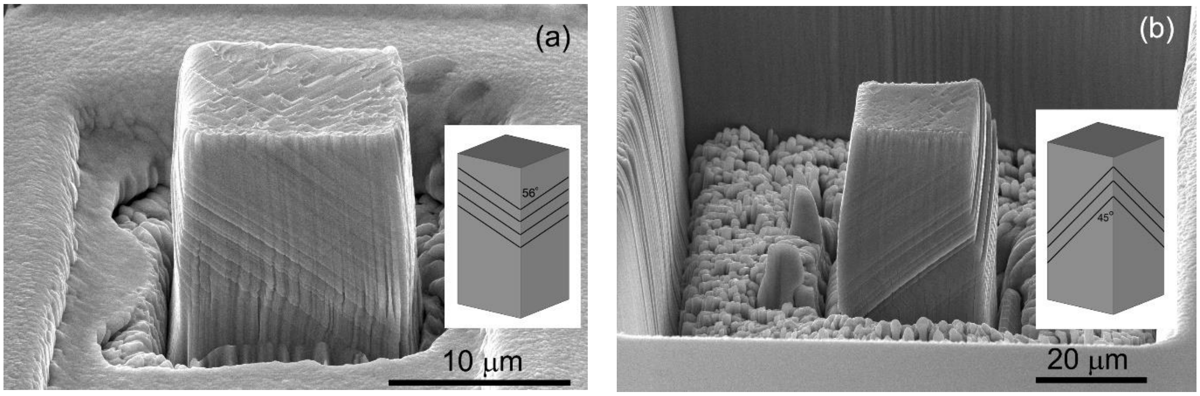

Figure 4.7. SEM image with the slip trace schematics inset of **(a)** [001] micropillar and **(b)** [111] oriented micropillars.

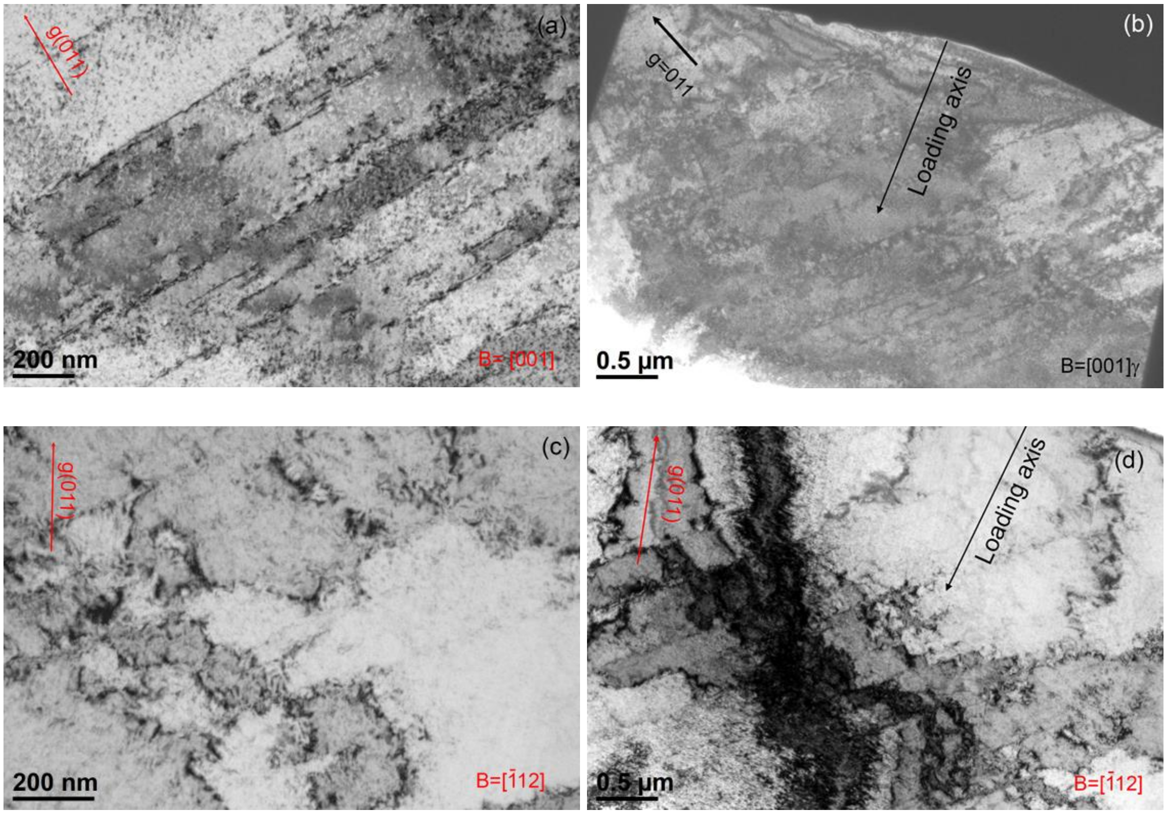

Figure 4.8. (a) and **(b)**The brightfield TEM from the [001] oriented micropillar, operating on B=[001] axis, display predominantly planar dislocation perpendicular to g={011} directions. **(c)** and **(d)** The brightfield TEM image from the deformed [111] oriented micropillar shows the wavy dislocation glide on {111} planes. There is no indication of any dislocation on the slip bands. SEAD pattern shows that B2 has [011] // FCC [-112] axis.

4.4 Discussion

4.4.1 Mechanical behaviors response in bulk compression.

The mechanical behaviors from bulk compression testing exhibit distinct work hardening stages. These stages of work hardening are (I) easy glide, (II) athermal work hardening, (III) dynamic recovery, and (IV) large strain stages like that described by Roilette [27]. The S-curve strain hardening rate, as observed in low SFE metals, gives a hint of some microstructural evolutions during the deformation [10-12, 28]. This dynamic behavior of Compression yield strength of 320 MPa is in between that of the $Al_{0.3}CoCeFeNi$ (180 MPa) and $Al_{0.5}CoCeFeNi$ (420 MPa) HEAs [11, 20]. This shows that the SRO, evidenced from the SAED and Moiré fringes image, contributes to strengthening mechanisms of $Al_{0.4}CoCrFeNi$. Estimation of the contribution from B2 SRO phase on yield strength (σ_y) can be done using a linear strengthening mechanism model in **Equation 4.1**[29].

$$\sigma_y = \sigma_0 + \sigma_{SS} + \sigma_{H-P} + \sigma_{Orowan} + \sigma_{Dislocation} \qquad (4.1)$$

Where σ_0 is lattice friction stress, σ_{SS} is solid solution strengthening, σ_{H-P} is the Hall-Petch strengthening effect, σ_{Orowan} is the effect of precipitation strengthening, and $\sigma_{Dislocation}$ is dislocation strengthening. The effect of solid solution strengthening for 0.1 mol extra Al composition in this $Al_{0.4}CoCrFeNi$ is reported to be 10 MPa per 0.1 mol of Al [30]. Lattice frictional stress and Hall-Petch coefficient taken from $Al_{0.3}CoCrFeNi$ are 96 MPa and 824 MPa·µm$^{-0.5}$, respectively [18]. Taken all accounting from lattice frictional stress solid solution strengthening and Hall-Petch effect, the yield strength of this HEA is 195 MPa. Another 125 MPa contribution could be from the effect of dislocation strengthening and Orowan strengthening from B2 SRO.

The microstructure of $Al_{0.4}CoCrFeNi$ HEA is typical for cast structure which contains a dendritic structure. The alloy exhibits a single-phase microstructure like that $Al_{0.3}CoCeFeNi$ with an additional short-range ordered B2 (NiAl) phase which is displayed as the superlattice diffraction in the AR specimen TEM SAED pattern. No slip lines are observed in the AR specimen as observed in the TEM micrographs. After the compression, the dislocation evolution progress from perfect dislocation glide, planar dislocation glide to dislocation forming microbands as the strain increases. This change in dislocation behavior during the deformation suggests that the SFE decreases as the deformation progresses to the higher strain [31].

The deformation mode of the FCC metals is strongly relating to their stacking faults energy (SFE). The estimated SFE of 30 mJ/m^2 from $Al_{0.1}CoCrFeNi$ is reported to assist the formation of TWIP in this HEA [32]. Later, calculated intrinsic stacking faults energy from $Al_{0.375}CoCrFeNi$ is shown to be 33.7 mJ/m^2 and decrease as the amount of Al in the system increase [33]. Thus, using the data reported from the study for extrapolation, the SFE in this HEA is about 33 mJ/m^2. This relatively low SFE reflects in good strain hardening rate of the HEA. The alloy exhibits good hardening behavior with the strain hardening rate of 1500 MPa at ε=5% and 3500 MPa at ε=25%. The strain hardening that shows the increase after plateau around ε=5% is the characteristic of dynamics deformation induces phase transformation that shortens the dislocation mobility distance, *e.g.*, twinning induced plasticity or transformation induced plasticity effects in coarse grain size [28]. This characteristic is predominant in coarse grain metals. In smaller grain metals, this increase in strain hardening is not predominant as the effect is undercast by the random grain boundary Hall-Petch effect.

4.4.2 Dislocation dynamics in bulk compression testing

The mechanical properties and microstructures correlation can be explained by looking at the individual strain level. The work hardening rate at 3% strain is smallest then progressively increases at 10% and plateau out at 24%. The mobility of dislocation in the FCC metals is known to be active on the {111} planes as it is the plane of stacking faults. At the initial stage of work hardening, the dislocation comprises the majority of planar dislocations. The planar dislocations then pile up forming bands. This stacking is the result of Lomer-Cottrell lock or Stair rod dislocation where the interaction from two dissecting glide planes reacts and forming sessile dislocation [34-36]. The TEM image at 3% shows the straight-line dislocation that is on [110] directions indicated that the straight-line dislocation serves as the Lomer-Cottrell lock that impedes the following dislocation by inserting back stress to them. Two dislocations from two intersected dislocation glide planes (xy and x′y′) interact with each other and form new dislocation (x′′y′′). This new dislocation has the burgers vector of $\frac{a}{2}[110]$. This dislocation geometry is best observed near B=[110] zone axis as it appears as an extension line dislocation to the $[1\bar{1}0]$ normal to the image plane. Then during stage II, the strain hardening rate increases during the coupling effect of evolved sessile dislocation and dislocation piled-up, as a witness in the microstructure of 10% strain. At 20% strain, the work hardening rate plateau out at 3500 MPa reflecting the annihilation of dislocation. Based on work hardening the stage IV, where the work hardening rate decreases, has been thought to be the result of temperature recovery of strain recovery [37-39]. In the 24% strain TEM image, the dislocation becomes dense cells. This feature is a behavior of strain recovery metal.

4.4.3 Micromechanical behavior of $Al_{0.4}$CoCrFeNi micropillar HEA

Mechanical behavior of the micropillar shows that the yield strength of [001] oriented micropillar is 335 ± 68 MPa whilst yield strength from [111] oriented micropillars is 537 ± 3 MPa. The slip traced from the [001] oriented micropillar shows the angle between the slip and the loading direction is 56^{o}. The implication from the trace shows the deformation belongs to $<011>\{111\}$ systems. In contrast, the slip trace from [111] oriented micropillar is at 45^{o}, which is the maximum shear plane from the loading direction, does not seem to associate with any dislocation movement. The yield strength of the micropillars is higher than that of the bulk specimen. Even in the soft orientation *i.e.* [001] direction, the yield strength is higher than that of the bulk compression specimen. This implies that the 10 um micropillar has a size effect on the mechanical properties. It is also evidenced by not having many dislocations in the TEM micrograph compared to the relatively similar strain of 10% in the bulk compression test. Dislocation in [001] micropillar exhibit planar dislocation along the slip lines with some dissociation into dislocation dipole like that 10% deformation in a bulk specimen. In contrast, dislocation structures found in [111] oriented micropillar are mostly perfect wavy dislocation.

The mechanical behavior of the micropillars is the mechanical properties of the single crystal that have the same orientation as the micropillars' orientations. Critical shear stress calculated from [001] oriented micropillar can be calculated from the following equation.

$\tau_{CRSS} = \sigma cos\phi cos\lambda$ (4.2)

where ϕ is the angle between slip plane normal and loading direction, λ is the angle between slip direction and loading direction, and σ is the yield stress. Calculating CRSS using yield strength from [001] oriented micropillar of 327 MPa, the <011>{111} type slip, having Schmid factor of 0.41, has the CRSS of 134 MPa. While using measurement data from [111] oriented micropillar, with a Schmid factor of 0.27, gives the CRSS of 140 MPa.

The strength in a small scale mechanical test smaller than 30 µm is higher than that of a bulk specimen because of the lack of the dislocation sources available in the specimen. Hence, the CRSS obtained from our micropillar size (base dimension 10 μm) needs to be scaled down for comparing with bulk material [40-44]. The regression slope for scaling down used by Okamoto *et al*. [40] for the CoCrFeMnNi HEA is -0.63. Based on this scaling factor, the calculated CRSS in $Al_{0.4}$CoCrFeNi HEA is 69-89 MPa (based on the expected micropillar base dimension of 30 and 20 µm). This number is higher than that of the reported 33 MPa for CoCrFeMnNi HEA by Okamoto et al [40]. This is most likely due to the effect of the SRO that makes the $Al_{0.4}$CoCrFeNi micropillar stronger than the single-phase CoCrFeMnNi HEA [41]. To compare the CRSS with other FCC metals, the CRSS usually normalized with its shear modulus [40, 42-44]. The calculated shear modulus of this $Al_{0.4}$CoCrFeNi is 76 GPa, using Young's modulus of 200 GPa and the Poisson ratio of 0.32. The normalized CRSS of this alloy is 1.17×10^{-3}. This number is greater than that of the single crystal TWIP steel as reported elsewhere [42]. This could be because of the coupling effect from the presence of SRO and the heavy lattice distortion effect in HEAs.

4.5 Conclusion

1. The bulk mechanical of as cast alloy displays compressive yield strength of 320 MPa with exceptional work hardening rate in the range of 1500 to 3500 MPa.
2. $Al_{0.4}$CoCrFeNi dislocation structure evolved from perfect dislocation glide to microband induced plasticity as the strain magnitude increases.
3. Low stacking faults energy promotes perfect planar dislocation slip which benefits in generating the sessile dislocation. These sessile dislocations, known as Lomer-Cottrell lock, help the alloy having exceptional compression work hardenability. By forming
4. Micropillar compression test shows that the [001] oriented micropillar has higher compressive yield strength compared to that of bulk deformation which could be the size effect of the micropillar.

5. The high CRSS value in this HEA comes from the presence of SRO and heavy lattice distortion.

Acknowledgment

This research was funded in part by an Undergraduate Research Grant from the Office of Undergraduate Research at the University of Idaho. Also, Anumat Sittiho would like to acknowledge The Royal Thai Navy for providing him with a graduate scholarship.

References

[1] Yeh, J. W., Chen, S. K., Lin, S. J., Gan, J. Y., Chin, T. S., Shun, T. T., … Chang, S. Y. (2004). Nanostructured high-entropy alloys with multiple principal elements: Novel alloy design concepts and outcomes. *Advanced Engineering Materials*, *6*(5), 299–303+274. https://doi.org/10.1002/adem.200300567

[2] Cantor, B., Chang, I. T. H., Knight, P., & Vincent, A. J. B. (2004). Microstructural development in equiatomic multicomponent alloys. *Materials Science and Engineering A*. https://doi.org/10.1016/j.msea.2003.10.257

[3] Zhao, Y. J., Qiao, J. W., Ma, S. G., Gao, M. C., Yang, H. J., Chen, M. W., & Zhang, Y. (2016). A hexagonal close-packed high-entropy alloy: The effect of entropy. *Materials and Design*. https://doi.org/10.1016/j.matdes.2016.01.149

[4] Maresca, F., & Curtin, W. A. (2020). Mechanistic origin of high strength in refractory BCC high entropy alloys up to 1900K. *Acta Materialia*. https://doi.org/10.1016/j.actamat.2019.10.015

[5] Murty, B. S. (2014). *High entropy alloys*. London: Butterworth-Heinemann.

[6] Miracle, D. B., & Senkov, O. N. (2017). A critical review of high entropy alloys and related concepts. *Acta Materialia*. https://doi.org/10.1016/j.actamat.2016.08.081

[7] Senkov, O. N., Wilks, G. B., Miracle, D. B., Chuang, C. P., & Liaw, P. K. (2010). Refractory high-entropy alloys. *Intermetallics*. https://doi.org/10.1016/j.intermet.2010.05.014

[8] Troparevsky, M. C., Morris, J. R., Kent, P. R. C., Lupini, A. R., & Stocks, G. M. (2015). Criteria for predicting the formation of single-phase high-entropy alloys. *Physical Review X*. https://doi.org/10.1103/PhysRevX.5.011041

[9] Li, Z., Pradeep, K. G., Deng, Y., Raabe, D., & Tasan, C. C. (2016). Metastable high-entropy dual-phase alloys overcome the strength-ductility trade-off. *Nature*. https://doi.org/10.1038/nature17981

[10] Mishra, R. S., Nene, S. S., Frank, M., Sinha, S., Liu, K., & Shukla, S. (2020). Metastability driven hierarchical microstructural engineering: Overview of mechanical properties of metastable complex concentrated alloys. *Journal of Alloys and Compounds*. https://doi.org/10.1016/j.jallcom.2020.155625

[11] Bönisch, M., Wu, Y., & Sehitoglu, H. (2018). Twinning-induced strain hardening in dual-phase FeCoCrNiAl0.5 at room and cryogenic temperature. *Scientific Reports*, *8*(1), 10663. https://doi.org/10.1038/s41598-018-28784-1

[12] Li, Z., Tasan, C. C., Pradeep, K. G., & Raabe, D. (2017). A TRIP-assisted dual-phase high-entropy alloy: Grain size and phase fraction effects on deformation behavior. *Acta Materialia*, *131*, 323–335. https://doi.org/10.1016/j.actamat.2017.03.069

[13]5. Li, Z., Pradeep, K. G., Deng, Y., Raabe, D., & Tasan, C. C. (2016). Metastable high-entropy dual-phase alloys overcome the strength-ductility trade-off. *Nature*, *534*(7606), 227–230. https://doi.org/10.1038/nature17981

[14] Li, Z., Tasan, C. C., Springer, H., Gault, B., & Raabe, D. (2017). Interstitial atoms enable joint twinning and transformation induced plasticity in strong and ductile high-entropy alloys. *Scientific Reports*, *7*. https://doi.org/10.1038/srep40704

[15] Wang, W. R., Wang, W. L., & Yeh, J. W. (2014). Phases, microstructure and mechanical properties of AlxCoCrFeNi high-entropy alloys at elevated temperatures. *Journal of Alloys and Compounds*, *589*, 143–152. https://doi.org/10.1016/j.jallcom.2013.11.084

[16] Sohn, S. S., Song, H., Kwak, J. H., & Lee, S. (2017). Dramatic improvement of strain hardening and ductility to 95% in highly-deformable high-strength duplex lightweight steels. *Scientific Reports*, *7*(1), 1927.

[17] Huo, W., Zhou, H., Fang, F., Hu, X., Xie, Z., & Jiang, J. (2017). Strain-rate effect upon the tensile behavior of CoCrFeNi high-entropy alloys. *Materials Science and Engineering A*, *689*(February), 366–369. https://doi.org/10.1016/j.msea.2017.02.077

[18] Gwalani, B., Soni, V., Lee, M., Mantri, S. A., Ren, Y., & Banerjee, R. (2017). Optimizing the coupled effects of Hall-Petch and precipitation strengthening in a Al0.3CoCrFeNi high entropy alloy. *Materials and Design*, *121*(121), 254–260. https://doi.org/10.1016/j.matdes.2017.02.072

[19] Li, Z., Zhao, S., Diao, H., Liaw, P. K., & Meyers, M. A. (2017). High-velocity deformation of Al0.3 CoCrFeNi high-entropy alloy: Remarkable resistance to shear failure. *Scientific Reports*. https://doi.org/10.1038/srep42742

[20] Shun, T. T., & Du, Y. C. (2009). Microstructure and tensile behaviors of FCC Al0.3CoCrFeNi high entropy alloy. *Journal of Alloys and Compounds*. https://doi.org/10.1016/j.jallcom.2008.12.088

[21] Feng, X. B., Fu, W., Zhang, J. Y., Zhao, J. T., Li, J., Wu, K., … Sun, J. (2017). Effects of nanotwins on the mechanical properties of AlxCoCrFeNi high entropy alloy thin films. *Scripta Materialia*, *139*, 71–76. https://doi.org/10.1016/j.scriptamat.2017.06.009

[22] Feng, X., Zhang, J., Wu, K., Liang, X., Liu, G., & Sun, J. (2018). Ultrastrong Al 0.1 CoCrFeNi high-entropy alloys at small scales: effects of stacking faults vs. nanotwins, *10*, 13329–13334. https://doi.org/10.1039/c8nr03573c

[23] Uchic, M. D., Dimiduk, D. M., Florando, J. N., & Nix, W. D. (2004). Sample dimensions influence strength and crystal plasticity. *Science*. https://doi.org/10.1126/science.1098993

[24] Mayer, C. R., Yang, L. W., Singh, S. S., Llorca, J., Molina-Aldareguia, J. M., Shen, Y. L., & Chawla, N. (2016). *Anisotropy, size, and aspect ratio effects on micropillar compression of AleSiC nanolaminate composites*. https://doi.org/10.1016/j.actamat.2016.05.018

[25] Fei, H., Abraham, A., Chawla, N., & Jiang, H. (2012). Evaluation of micro-pillar compression tests for accurate determination of elastic-plastic constitutive relations. *Journal of Applied Mechanics, Transactions ASME*.

[26] Greer, J. R., Oliver, W. C., & Nix, W. D. (2005). Size dependence of mechanical properties of gold at the micron scale in the absence of strain gradients. *Acta Materialia*. https://doi.org/10.1016/j.actamat.2004.12.031

[27] Roilett, A. D., & Kocks, U. F. (1993). Title: A Review of the Stages of Work Hardening. In *Proceeding of Dislocations-93 conference at Aussois, France, 1-9 Apr 1993*. Los Alamos National Laboratory. https://digital.library.unt.edu/ark:/67531/metadc1342227/

[28] Tian, Y. Z., Zhao, L. J., Chen, S., Shibata, A., Zhang, Z. F., & Tsuji, & N. (2015). Significant contribution of stacking faults to the strain hardening behavior of Cu-15%Al alloy with different grain sizes OPEN. *Scientific RepoRts |*, *5*, 16707. https://doi.org/10.1038/srep16707

[29] Sittiho, A., Tungala, V., Charit, I., & Mishra, R. S. (2018). Microstructure, mechanical properties and strengthening mechanisms of friction stir welded Kanthal APMT^{TM} steel. *Journal of Nuclear Materials*, *509*. https://doi.org/10.1016/j.jnucmat.2018.07.001

[30] Xu, X. D., Liu, P., Hirata, A., Song, S. X., Nieh, T. G., & Chen, M. W. (2018). Microstructural origins for a strong and ductile Al0.1CoCrFeNi high-entropy alloy with ultrafine grains. *Materialia*, *4*, 395–405. https://doi.org/10.1016/j.mtla.2018.10.015

[31] Branicio, P. S., Srolovitz, D. J., Branicio, P. S., & Zhang, J. Y. (2013). Effect of strain on the stacking fault energy of copper: A first-principles study Working mechanism of polycarboxylate ether superplasticizers for concrete View project Effect of strain on the stacking fault energy of copper: A first-principles study. *PHYSICAL REVIEW B*, *88*, 64104. https://doi.org/10.1103/PhysRevB.88.064104

[32] Kumar, N., Ying, Q., Nie, X., Mishra, R. S., Tang, Z., Liaw, P. K., … Cho, K. C. (2015). High strain-rate compressive deformation behavior of the Al0.1CrFeCoNi high entropy alloy. *Materials and Design*, *86*, 598–602. https://doi.org/10.1016/j.matdes.2015.07.161

[33] Beyramali Kivy, M., & Asle Zaeem, M. (2017). Generalized stacking fault energies, ductilities, and twinnabilities of CoCrFeNi-based face-centered cubic high entropy alloys. *Scripta Materialia*. https://doi.org/10.1016/j.scriptamat.2017.06.014

[34] Cottrell, A. H. (1952). LX. The formation of immobile dislocations during slip. *The London, Edinburgh, and Dublin Philosophical Magazine and Journal of Science*, *43*(341), 645–647. https://doi.org/10.1080/14786440608520220

[35] Lomer, W. M. (1951). A dislocation reaction in the face-centred cubic lattice. *The London, Edinburgh, and Dublin Philosophical Magazine and Journal of Science*, *42*(334), 1327–1331. https://doi.org/10.1080/14786444108561389

[36] Whelan, M. J., Whelan, & J., M. (1959). Dislocation interactions in face-centred cubic metals, with particular reference to stainless steel. *Proceedings of the Royal Society of London. Series A. Mathematical and Physical Sciences*, *249*(1256), 114–137. https://doi.org/10.1098/rspa.1959.0011

[37] Anderson, P. M., Hirth, J. P., & Lothe, J. (2017). *Theory of dislocations*. Cambridge University Press.

[38] Orowan, E. (1946). Creep in Metals. *J. West Scotland Iron & Steel Inst.*, *54*, 45.

[39] Kocks, U. F., & Mecking, H. (2003). Physics and phenomenology of strain hardening: The FCC case. In *Progress in Materials Science* (Vol. 48, Issue 3, pp. 171–273). Pergamon. https://doi.org/10.1016/S0079-6425(02)00003-8

[40] Okamoto, N. L., Fujimoto, S., Kambara, Y., Kawamura, M., Chen, Z. M. T., Matsunoshita, H., Tanaka, K., Inui, H., & George, E. P. (2016). Size effect, critical resolved shear stress, stacking fault energy, and solid solution strengthening in the CrMnFeCoNi high-entropy alloy. *Scientific Reports*, *6*(October), 1–10. https://doi.org/10.1038/srep35863

[41] Kim, J. H., & Na, Y. S. (2019). Tensile Properties and Serrated Flow Behavior of As-Cast CoCrFeMnNi High-Entropy Alloy at Room and Elevated Temperatures. *Metals and Materials International*, *25*(2), 296–303. https://doi.org/10.1007/s12540-018-0200-x

[42] Choi, W. S., Sandlöbes, S., Malyar, N. V., Kirchlechner, C., Korte-Kerzel, S., Dehm, G., De Cooman, B. C., & Raabe, D. (2017). Dislocation interaction and twinning-induced plasticity in face-centered cubic Fe-Mn-C micro-pillars. *Acta Materialia*. https://doi.org/10.1016/j.actamat.2017.04.043

[43] Dou, R., & Derby, B. (2009). A universal scaling law for the strength of metal micropillars and nanowires. *Scripta Materialia*, *61*(5), 524–527. https://doi.org/10.1016/j.scriptamat.2009.05.012

[44] Frick, C. P., Clark, B. G., Orso, S., Schneider, A. S., & Arzt, E. (2008). Size effect on strength and strain hardening of small-scale [1 1 1] nickel compression pillars. *Materials Science and Engineering A*, *489*(1–2), 319–329. https://doi.org/10.1016/j.msea.2007.12.038

Chapter 5: Thermal Stability of $Al_{0.4}CoCrFeNi$ High Entropy Alloy

Abstract

$Al_{0.4}CoCrFeNi$ is a high entropy alloy (HEA) having a single-phase FCC microstructure. The thermal stability of this HEA is studied by using high temperature compression testing, dilatometry, and thermal aging. The HEA exhibits Vickers microhardness increment due to the formation of NiAl B2 phase precipitation after thermally aged at temperature range between 820 – 1000^{o}C. and would reach the peak hardness after 4,000 h of aging. The high temperature flow behavior of the alloy exhibits serrated flow at the temperature of 600^{o}C. The homogenization of this HEA alters the serration flow behavior and its strain rate sensitivity. Dilatometry of the HEA revealed phase changes occurring at specific temperature ranges and a higher thermal expansion coefficient of this HEA compared to other FCC based HEAs and alloys from the literature.

5.1 Introduction

High entropy alloys (HEA) are a class of unique metallic alloys that maximize their configurational entropy by having multiple principal elements [1, 2]. Because of the high configurational entropy effect, the HEAs are found to have simple phases well below the amount theorized by Gibbs phase rules [3]. Despite the expected presence of single-phase disordered solid solution in HEAs, they normally exhibit several phases in the system due to the effect of the mixing enthalpy of some intermetallics present in the systems [4-6]. These second phases, under certain circumstances, can be beneficial to the HEA.

One of the well-studied HEA alloy systems is $Al_xCoCrFeNi$ HEAs where x is between 0 to 1.5 [6-9]. This alloy shows phase tunability varying with x value. The single-phase FCC and BCC happened when $x < 0.3$ and $x > 1.2$, respectively. In between, the alloy shows to have FCC+BCC phases. Mechanical behaviors of the $Al_{0.3}CoCrFeNi$ and $Al_{0.5}CoCrFeNi$ show to have higher strength in the dual-phase alloy [10-14]. The yield strength of the single-phase $Al_{0.3}CoCrFeNi$ is 180 MPa is significantly less than that of $Al_{0.5}CoCrFeNi$ at 400 MPa. The mechanical properties of $Al_{0.4}CoCrFeNi$, transition composition between those two HEAs, is not well studied even though it can be the transition bridge to understand the behavior of this HEA system when the system evolves from single-phase to dual-phase type microstructure. Although HEAs have desirable mechanical properties at room temperature, the high temperature properties are needed to be examined to evaluate the feasibility of using such materials in practical applications. The present study aims to explore the thermal stability characteristics of

$Al_{0.4}$CoCrFeNi HEA, focusing onthe phase transformation, thermal expansion, and mechanical properties at the elevated temperatures.

5.2 Experimental procedure

The $Al_{0.4}$CoCrFeNi used in this study was made via vacuum arc casting by Sophisticated Alloys Inc, Butler, PA, USA. The alloy was studied for its thermal stability of the as cast specimen compared to the heat treated specimens. Their microstructural characteristics were examined by means of optical electron microscopy and electron microscopy. The metallographic specimens and SEM specimens were prepared by grinding specimen with SiC paper down to 1200 grit followed by polishing with alumina slurry down to 0.3 µm surface finish. Then the polished specimens were etched with a solution containing HNO_3 and HCl (1:3 by volume). The optical metallography was performed using Olympus PGM-3 inverted light microscope. Scanning electron microscopy was carried out using a Zeiss Supra 35 SEM equipped with Thermofisher Noran System 6 energy dispersive spectroscopy (EDS), respectively. All the SEM analysis was done at the operating voltage of 20 keV.

Later, based on the phase calculations done by Zhang *et al*. [15], the as cast specimens were heat-treated at 1350^{o}C for 24 h followed by normalizing to achieve homogenization. Subsequently, some homogenized samples aged at 820^{o}C, 900^{o}C, and 1000^{o}C for up to 7500 min to study the kinetics of the phase transformation. After aging, the specimens were tested for Vickers microhardness using a LECO LM-100 Microhardness Tester under a load of 0.5 kg_f (4.91 N)

Elevated temperature mechanical behavior of the as received and heat treated HEA specimens were characterized by using uniaxial compression testing done on Instron 5982 model universal testing frame with a maximum load capacity of 100 kN. The tests were carried on at different temperatures and strain rates, ranging from 10^{-5} to 10^{-2} s^{-1}, to examine the flow behavior of the alloy under various loading conditions. Thermal expansion characteristics of the HEA were examined using Netzch 403C dilatometer equipped with alumina crucible and push rod. Prior to the test, the calibration was done using a polycrystalline alumina rod. The test was done in 3 heating and 3 cooling cycles under argon atmosphere to ensure the reproducibility. The heating/cooling rate during the test was 10 K/min and the maximum temperature was 1200 ^{o}C.

5.3 Results and discussion

The microstructural evolutions of the alloy resulting from thermal heat treatment are examined by optical microscopy and scanning electron microscopy. The as cast microstructure shows a dendritic microstructure with a coarse grain size (grain size greater than 200 µm), as shown in **Figure 5.1(a)**. **Figure 5(b)** depicts corresponding SEM electron backscattered (BSE) image showing some phase segregation at the interdendritic region. This segregated phase was identified as NiAl phase from EDS analysis. After homogenizing heat treatment at 1320°C for 24 h, the dendritic microstructure was successfully removed with no detectable second phase precipitates as shown in optical and SEM images as in **Figure 5.1(c)** and **(d)**, respectively. The prolonged aging (7500 h) at 900°C resulted in the precipitation of NiAl (B2) phases, revealed by optical, SEM, and the EDS elemental maps in **Figure 5.1 (e-g)**. The rod-shaped NiAl precipitates at both the grain boundary and inside the grains. There is no Cr-rich σ-phase precipitate detected. The hardness decreases from 346 $HV_{0.5}$ in the as cast specimen and to 129 $HV_{0.5}$ in the homogenized one.

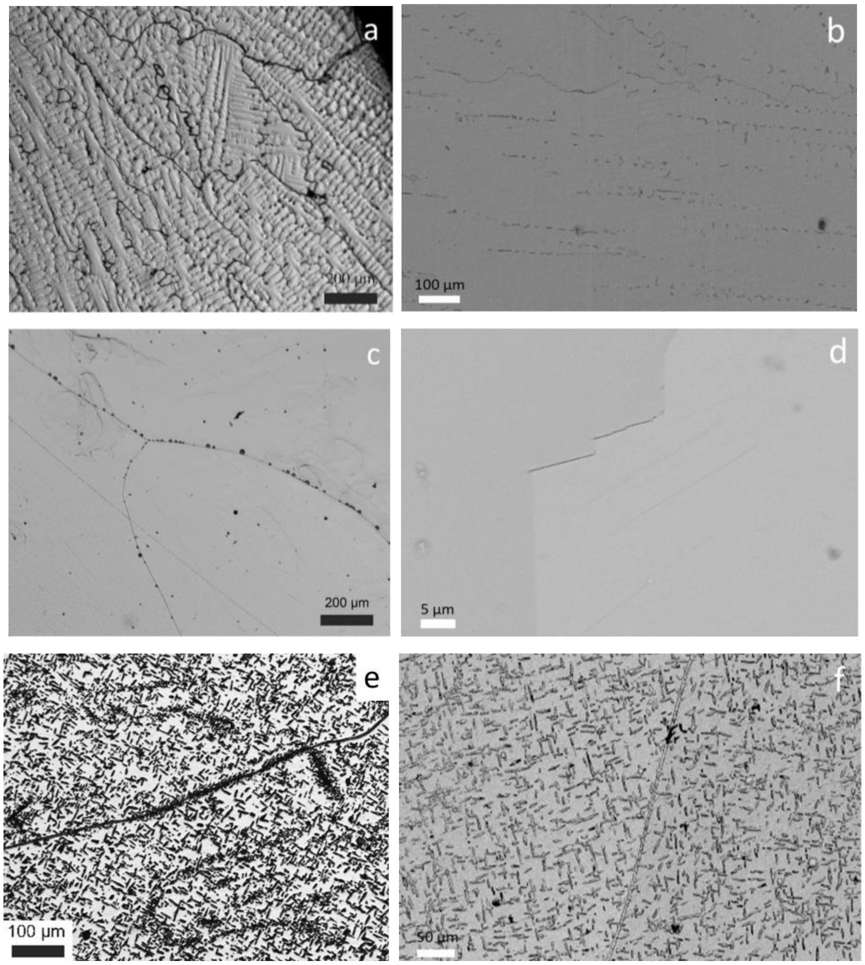

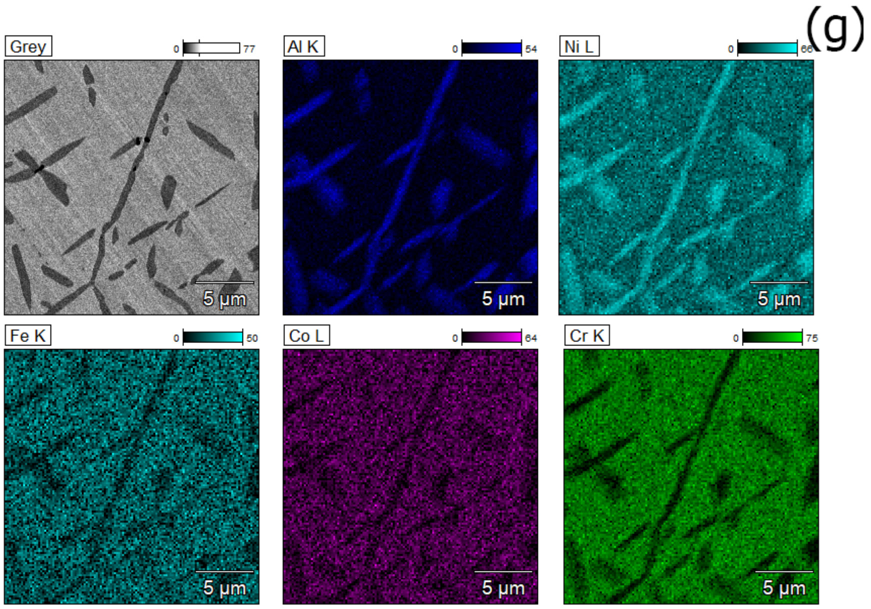

Figure 5.1. The optical and SEM backscattered images of **(a, b)** as cast, **(c, d)** homogenized, and **(e, f)** 7000 h aged at 900°C. (g) EDS elemental map from 8000h 900°C aged specimen

The Vickers hardness test on the HEA reveals the change responding to the heat treatment as displayed in **Figure 5.2(a)**. After homogenization heat treatment, the hardness decreases from 346 $HV_{0.5}$ in the as cast specimen and to 129 $HV_{0.5}$. Then, the progressive increase in Vickers microhardness are observed in the aging heat treatment of the alloy specimens at 820°C, 900°C, and 1000°C. The peak aging was reached after 4000 min. The increase in hardness at the peak aged condition was measured to be 45 $HV_{0.5}$ increase from the homogenized specimen. The increase in hardness is the results of microstructural evolution during aging heat treatment [16-19]. The overall yield strength of $Al_xCoCrFeNi$ is contributed by five individual strengthening mechanisms as shown in the following equation:

$$\sigma_y = \sigma_0 + \sigma_{SS} + \sigma_{HP} + \sigma_{Dis} + \sigma_{Oro} \qquad (5.1)$$

where σ_y is yield strength, σ_0 is lattice friction stress, σ_{SS} is solid solution strengthening, σ_{HP} is Hall-Petch strengthening, σ_{Dis} is dislocation strengthening, and σ_{Oro} is Orowan strengthening. In this study, it is reasonable to assume that contributions from σ_0, σ_{SS}, and σ_{HP} remain the same in the strengthening mechanisms as there is no change in chemical compositions nor the grain size during the aging treatment. Dislocation density is also unlikely to increase during aging without any mechanical work done to the system. Hence, the yield strength of the system varies as a function of the Orowan strengthening mechanism which is expressed as **Equation (5.2)**.

$$\sigma_{Oro} = \frac{Gb}{L} \quad (5.2)$$

where G is the shear modulus, b is the Burgers vector, and L is the inter-particle distance which is the function of volume fraction and size of the precipitates. **Figure 5.2 (b)** shows the engineering stress – engineering plastic strain from which compressive yield strengths (ε = 0.2%) of the alloy are estimated to be 159 MPa and 216 MPa for homogenized and aged specimens, respectively. This demonstrates the importance of the precipitates on the room temperature yield strength of this HEA. Similarly, the Vickers microhardness of the homogenized specimen is 129 $HV_{0.5}$ and for the aged specimen (900°C / 50 h) is 175 $HV_{0.5}$. This shows the proportional relationship between Vickers microhardness and yield strength in this HEA. Thus, the continuous change in Vickers hardness over time during the aging heat treatment is due to the precipitation kinetics in the $Al_{0.4}CoCrFeNi$ HEA.

The kinetics of phase transformation at different temperatures of this HEA can be estimated by using Avrami kinetics equation which is applicable for nucleation-growth based phase transformation at a constant temperature. The kinetics of phase transformation is more aptly described by Johnson-Mehl-Avrami (JMA) equation as shown in **Equation 5.3** [20-22].

$$1 - Y = EXP(-Kt)^n \quad (5.3)$$

where Y is the transformed phase fraction, K is the relevant rate constant, t is time, and n is Avrami exponent. In this study, the transformed phase fraction can be obtained via **Equation (5.4)**.

$$Y = \frac{HV_t - HV_0}{HV_f - HV_0} \quad (5.4)$$

where the subscripts, t, f, and 0 denote the Vickers microhardness as a function of time variable, homogenized, and peak aged, respectively. The JMA plot of aging kinetics at different aging temperatures is shown in **Figure 5.2 (c)**. The characteristic of the NiAl precipitation kinetics is similar between 900°C and 1000°C aged specimens where the Avrami exponent is 1.78. The lower Avrami exponent is found in 820°C aged specimen with a value of 1.48.

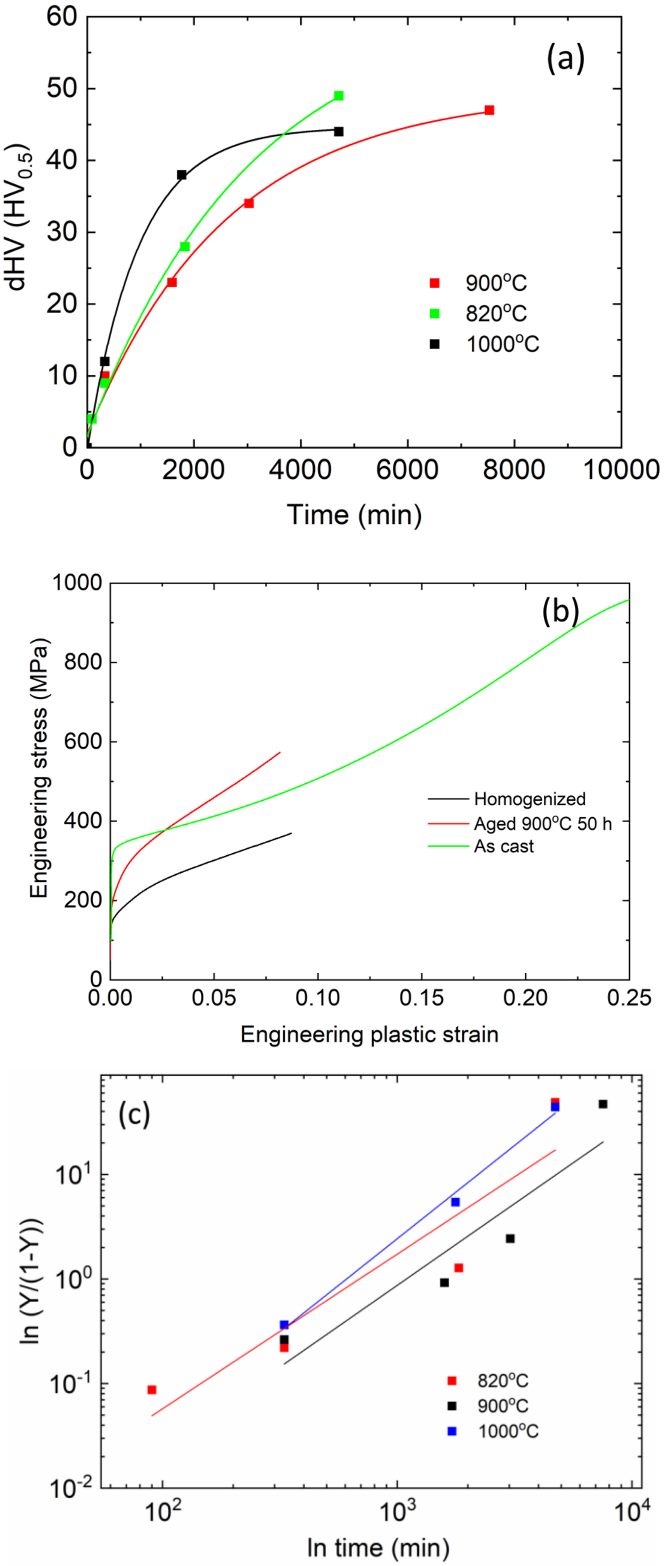

Figure 5.2. (a) The change in hardness over time at different aging temperatures of Al0.4CoCrFeNi. (b) The room temperature flow behavior of homogenized and 900ºC 50h aged specimens. (b) Kinetics of phase transformation of the alloy at different temperatures.

$Al_{0.4}CoCrFeNi$ HEA shows serrated flow behavior at elevated temperature. The serrated flow is observed in both as cast and homogenized specimens during the compression test at 600°C. This serrated flow behavior has been reported in this HEA system as a result of the dynamic strain aging effect (DSA). Yasuda et al. [23] reported the DSA of the $Al_{0.3}CoCrFeNi$ single crystal can be observed between 600°C to 800°C. Komarasamy *et al*. [24] observed that the DSA behavior of $Al_{0.1}CoCrFeNi$ was presented at a lower temperature range of 200°C to 400°C. The serration flow in the substitution solution alloy behavior in this alloy changes relative to the strain rate, strain level, as well as deformation temperature [25]. In **Figure 5.3 (a)**, the DSA of the as cast specimen at 600°C appears to involve type-E serrations at the 10^{-2} s^{-1} strain rate through all strain levels. However, the type-A serrations alternating with type-B are seen in the strain rate range of 10^{-3} and 10^{-4} s^{-1}. In **Figure 5.3(b)**, the strain rate change compression test of the homogenized specimen exhibits serrations of type-B through all the strain levels. The schematic of the serration flow in substitutional alloys is shown in **Figure 5.3(c)**.

The strain rate sensitivity (SRS) of this alloy at 600°C is shown in the uniaxial compression step test as **Figure 5.3 (a)** and **(b)**. At this temperature, the HEA exhibits the inverse SRS. It is believed to be because of the flow instability occurring during DSA. The strain rate sensitivity, m, can be calculated using the following equation:

$$m = \frac{log\frac{\sigma_1}{\sigma_2}}{log\frac{\dot{\varepsilon}_1}{\dot{\varepsilon}_2}} \qquad (5.5)$$

where σ and $\dot{\varepsilon}$ are true stress and strain rate, respectively. From this **Equation 5.5**, the m value for this HEA at 600°C is -0.006. The negative SRS is the result of the DSA at high temperatures [26-28]. On the contrary, the homogenized specimen compression step test at 600°C does not show the SRS effect (m = 0).

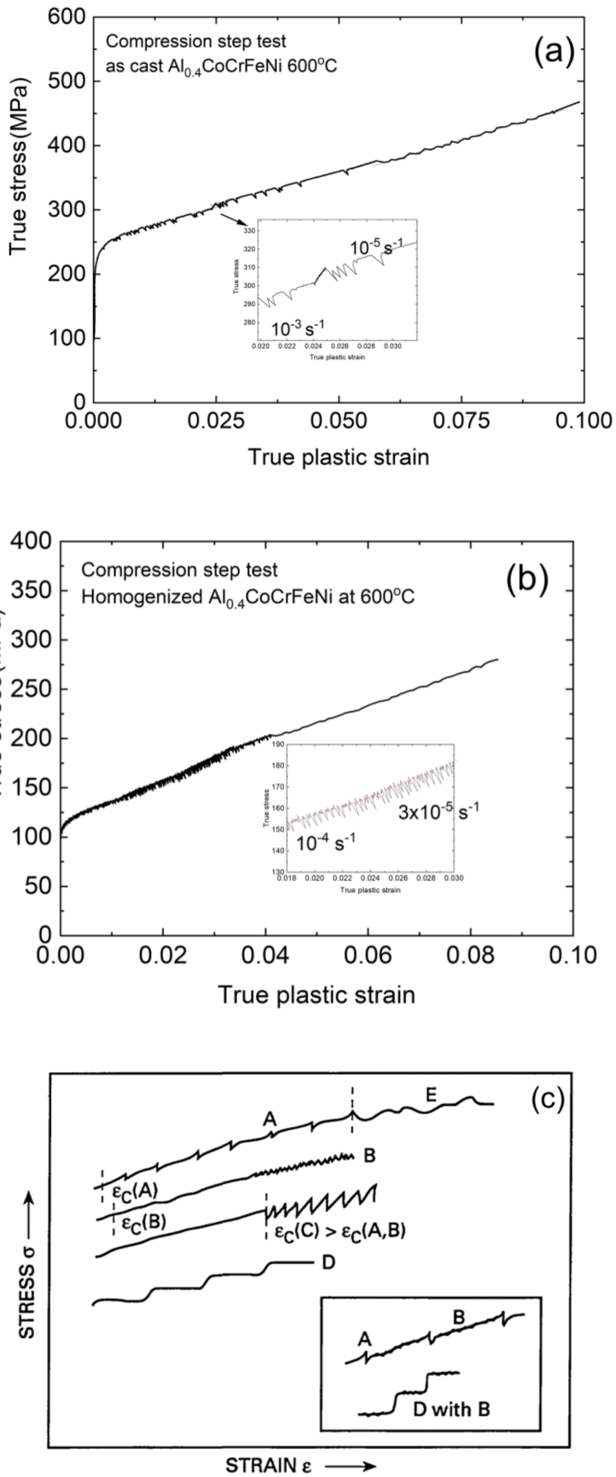

Figure 5.3. Flow curves of (a) the as-cast $Al_{0.4}$CoCrFeNi and (b) the homogenized at 600°C. (c) Schematic of serration flow types observed in substitutional solid solution alloys [25].

Thermal expansion as the function of the temperature of this alloy is shown in **Figure 5.4**. The thermal expansion behavior of this alloy is linear. There is an increase in thermal expansion coefficient from 600ºC to 800ºC. The thermal coefficient (CTE, α) can be calculated from **Equation 5.6**. The Thermal expansion coefficient value is summarized in **Table 5.1**.

$$\alpha = \frac{d}{dT}\left(\frac{L}{Lo}\right) \qquad (5.6)$$

where $\Delta L/L_o$ is the thermal strain and T is the temperature.

Table 5.1. Thermal expansion coefficient of $Al_{0.4}CoCrFeNi$

Temperature (ºC)	Thermal expansion coefficient ($10^{-}6 \cdot K^{-1}$)	Thermal strain (%)
300	22.1	0.336
400	23.2	0.563
500	23.6	0.796
600	28.6	1.057
700	36.1	1.370
800	29.2	1.715
900	29.0	2.003
1000	29.6	2.296
1100	31.0	2.596

The thermal expansion coefficient of this HEA is higher than that of Inconel 718 and $Al_{0.3}CoCrFeNi$ by an order of magnitude. This can be the influence of the excessive amount of Al in the HEA as the Al thermal expansion coefficient is around 25×10^{-6} K^{-1}. There is a big jump in the α value of this HEA, which occurs around 500ºC and reaches a peak at 750ºC. This behavior suggests that there is a phase transformation occurring across this temperature range [29].

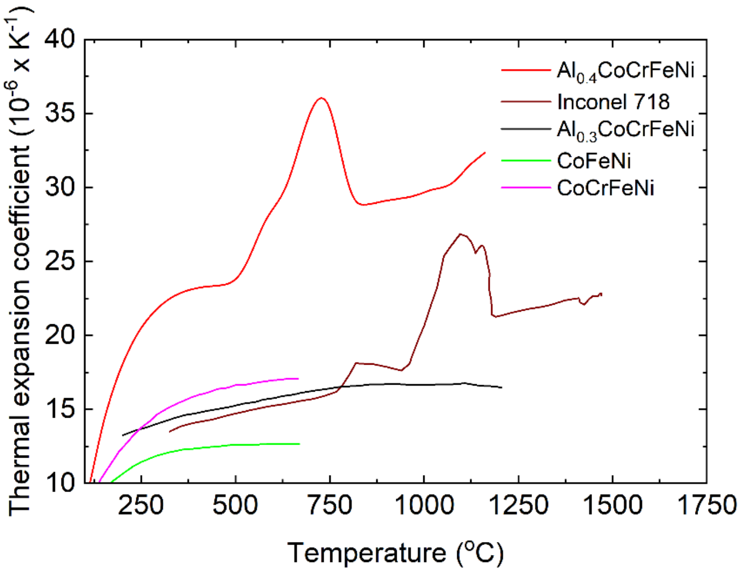

Figure 5.4. Linear thermal expansion coefficient of $Al_{0.4}$CoCrFeNi in comparison of other alloys [24, 29-31].

5.4 Conclusion

This work was undertaken to study the thermal stability of the $Al_{0.4}$CoCrFeNi HEA. The following conclusions are drawn from this study:

1. $Al_{0.4}$CoCrFeNi shows dendritic structure with some NiAl phase segregation at the interdendritic regions of the as cast specimen.

2. After homogenization, prolonged aging at 900°C promotes precipitation of rod-shaped B2-NiAl precipitates both at the grain boundaries and grain interior.

3. Kinetics of NiAl precipitates follows Avrami kinetics with Avrami exponent of in the range of 1.48 to 1.78.

4. The alloy exhibits DSA both under homogenized condition (with a majority of A-type serrations) and as cast condition (with type-B serrations) under compression at 600°C.

Acknowledgment

Anumat Sittiho would like to thank The Royal Thai Navy for financial support for his graduate study.

References

[1] Cantor, B., Chang, I. T. H., Knight, P., & Vincent, A. J. B. (2004). Microstructural development in equiatomic multicomponent alloys. *Materials Science and Engineering A*. https://doi.org/10.1016/j.msea.2003.10.257

[2] Yeh, J. W., Chen, S. K., Lin, S. J., Gan, J. Y., Chin, T. S., Shun, T. T., Tsau, C. H., & Chang, S. Y. (2004). Nanostructured high-entropy alloys with multiple principal elements: Novel alloy design concepts and outcomes. *Advanced Engineering Materials*, *6*(5), 299-303+274. https://doi.org/10.1002/adem.200300567

[3] Miracle, D. B., & Senkov, O. N. (2017). A critical review of high entropy alloys and related concepts. In *Acta Materialia*. https://doi.org/10.1016/j.actamat.2016.08.081

[4] Debski, A., Debski, R., & Gasior, W. (2015). New Features of Entall Database: Comparison of Experimental and Model Formation Enthalpies/ Nowe Funkcje Bazy Danych Entall: Porównanie Doświadczalnych I Modelowych Entalpii Tworzenia. *Archives of Metallurgy and Materials*. https://doi.org/10.2478/amm-2014-0228

[5] Otto, F., Yang, Y., Bei, H., & George, E. P. (2013). Relative effects of enthalpy and entropy on the phase stability of equiatomic high-entropy alloys. *Acta Materialia*. https://doi.org/10.1016/j.actamat.2013.01.042

[6] Chou, H. P., Chang, Y. S., Chen, S. K., & Yeh, J. W. (2009). Microstructure, thermophysical and electrical properties in AlxCoCrFeNi ($0 \leq x \leq 2$) high-entropy alloys. *Materials Science and Engineering B: Solid-State Materials for Advanced Technology*. https://doi.org/10.1016/j.mseb.2009.05.024

[7] Kao, Y. F., Chen, T. J., Chen, S. K., & Yeh, J. W. (2009). Microstructure and mechanical property of as-cast, -homogenized, and -deformed AlxCoCrFeNi ($0 \leq x \leq 2$) high-entropy alloys. *Journal of Alloys and Compounds*, *488*(1), 57–64. https://doi.org/10.1016/j.jallcom.2009.08.090

[8] Wang, W. R., Wang, W. L., & Yeh, J. W. (2014). Phases, microstructure and mechanical properties of AlxCoCrFeNi high-entropy alloys at elevated temperatures. *Journal of Alloys and Compounds*. https://doi.org/10.1016/j.jallcom.2013.11.084

[9] Yang, T., Xia, S., Liu, S., Wang, C., Liu, S., Zhang, Y., Xue, J., Yan, S., & Wang, Y. (2015). Effects of AL addition on microstructure and mechanical properties of AlxCoCrFeNi High-entropy alloy. *Materials Science and Engineering A*. https://doi.org/10.1016/j.msea.2015.09.034

[10] Guo, T., Li, J., Wang, J., Wang, W. Y., Liu, Y., Luo, X., Kou, H., & Beaugnon, E. (2018). Microstructure and properties of bulk Al0.5CoCrFeNi high-entropy alloy by cold rolling and subsequent annealing. *Materials Science and Engineering A*, *729*, 141–148. https://doi.org/10.1016/j.msea.2018.05.054

[11] Shun, T. T., & Du, Y. C. (2009). Microstructure and tensile behaviors of FCC Al0.3CoCrFeNi high entropy alloy. *Journal of Alloys and Compounds*. https://doi.org/10.1016/j.jallcom.2008.12.088

[12] Bönisch, M., Wu, Y., & Sehitoglu, H. (2018). Twinning-induced strain hardening in dual-phase FeCoCrNiAl0.5 at room and cryogenic temperature. *Scientific Reports*, *8*(1), 1–9. https://doi.org/10.1038/s41598-018-28784-1

[13] Gwalani, B., Soni, V., Lee, M., Mantri, S. A., Ren, Y., & Banerjee, R. (2017). Optimizing the coupled effects of Hall-Petch and precipitation strengthening in a Al0.3CoCrFeNi high entropy alloy. *Materials and Design*, *121*(121), 254–260. https://doi.org/10.1016/j.matdes.2017.02.072

[14] Li, Z., Zhao, S., Diao, H., Liaw, P. K., & Meyers, M. A. (2017). High-velocity deformation of Al0.3 CoCrFeNi high-entropy alloy: Remarkable resistance to shear failure. *Scientific Reports*. https://doi.org/10.1038/srep42742

[15] Zhang, C., Zhang, F., Diao, H., Gao, M. C., Tang, Z., Poplawsky, J. D., & Liaw, P. K. (2016). Understanding phase stability of Al-Co-Cr-Fe-Ni high entropy alloys. *Materials and Design*. https://doi.org/10.1016/j.matdes.2016.07.073

[16] Béres, G., & Weltsch, Z. (2019). Estimation of strength properties from microhardness results in dual phase steels with different martensite volume fraction. *Periodica Polytechnica Transportation Engineering*, *47*(3), 206–212. https://doi.org/10.3311/PPtr.12113

[17] Sharma, R., Welch, R. S., Kang, M., Goncalves, C., Blanco, C., Buff, A., Fauvel, V., Loretz, T., Rivero-Baleine, C., & Richardson, K. (2020). Impact of morphology and microstructure on the mechanical properties of Ge-As-Pb-Se glass ceramics. *Applied Sciences (Switzerland)*, *10*(8), 2836. https://doi.org/10.3390/APP10082836

[18] An, X. H., Wu, S. D., Zhang, Z. F., Figueiredo, R. B., Gao, N., & Langdon, T. G. (2010). Evolution of microstructural homogeneity in copper processed by high-pressure torsion. *Scripta Materialia*, *63,* 560–563. https://doi.org/10.1016/j.scriptamat.2010.05.030

[19] Zhang, P., Li, S. X., & Zhang, Z. F. (2011). General relationship between strength and hardness.

Materials Science and Engineering A. https://doi.org/10.1016/j.msea.2011.08.061

[20] Avrami, M. (1941). Granulation, phase change, and microstructure kinetics of phase change. III. *The Journal of Chemical Physics*, *9*(2), 177–184. https://doi.org/10.1063/1.1750872

[21] Capdevila, C., Miller, M. K., Pimentel, G., & Chao, J. (2012). Influence of recrystallization on phase separation kinetics of oxide dispersion strengthened Fe-Cr-Al alloy. *Scripta Materialia*, *66*(5), 254–257. https://doi.org/10.1016/j.scriptamat.2011.11.003

[22] Todinov, M. T. (2000). On some limitations of the Johnson-Mehl-Avrami-Kolmogorov equation. *Acta Materialia*, *48*(17), 4217–4224. https://doi.org/10.1016/S1359-6454(00)00280-9

[23] Yasuda, H. Y., Shigeno, K., & Nagase, T. (2015b). Dynamic strain aging of Al0.3CoCrFeNi high entropy alloy single crystals. *Scripta Materialia*, *108*, 80–83. https://doi.org/10.1016/j.scriptamat.2015.06.022

[24] Komarasamy, M., Alagarsamy, K., & Mishra, R. S. (2017). Serration behavior and negative strain rate sensitivity of Al0.1CoCrFeNi high entropy alloy. *Intermetallics*, *84*, 20–24. https://doi.org/10.1016/j.intermet.2016.12.016

[25] Robinson, J. M., & Shaw, M. P. (1994). Microstructural and mechanical influences on dynamic strain aging phenomena. *International Materials Reviews*, *39*(3), 113–122. https://doi.org/10.1179/imr.1994.39.3.113

[26] Picu, R. C. (2004). A mechanism for the negative strain-rate sensitivity of dilute solid solutions. *Acta Materialia*, *52*(12), 3447–3458. https://doi.org/10.1016/j.actamat.2004.03.042

[27] Beese, A. M., Wang, Z., Stoica, A. D., & Ma, D. (2018). Absence of dynamic strain aging in an additively manufactured nickel-base superalloy. *Nature Communications*, *9*(1). https://doi.org/10.1038/s41467-018-04473-5

[28] Yasuda, H. Y., Shigeno, K., & Nagase, T. (2015a). Dynamic strain aging of Al0.3CoCrFeNi high entropy alloy single crystals. *Scripta Materialia*. https://doi.org/10.1016/j.scriptamat.2015.06.022

[29] Wang, J., Niu, S., Guo, T., Kou, H., & Li, J. (2017). The FCC to BCC phase transformation kinetics in an Al0.5CoCrFeNi high entropy alloy. *Journal of Alloys and Compounds*, *710*(October), 144–150. https://doi.org/10.1016/j.jallcom.2017.03.249

[30] Agazhanov, A. S., Samoshkin, D. A., & Kozlovskii, Y. M. (2019). Thermophysical properties of Inconel 718 alloy. *Journal of Physics: Conference Series*, *1382*(1). https://doi.org/10.1088/1742-

6596/1382/1/012175

[31] Laplanche, G., Gadaud, P., Bärsch, C., Demtröder, K., Reinhart, C., Schreuer, J., & George, E. P. (2018). Elastic moduli and thermal expansion coefficients of medium-entropy subsystems of the CrMnFeCoNi high-entropy alloy. *Journal of Alloys and Compounds*, *746*, 244–255. https://doi.org/10.1016/j.jallcom.2018.02.251

Chapter 6: Conclusion and Suggested Future Work

High entropy alloy (HEA), $Fe_{42}Co_{10}Cr_{15}Mn_{28}Si_5$, appears to exhibit good solid state weldability using two solid-state welding techniques – friction stir welding (FSW) and pressure resistance welding (PRW). This observation would pave the way in expanding the boundary of the HEA from just being prototype alloys of academic curiosity to practical applications. The detailed study in the recrystallization of the transformation induced plasticity (TRIP) helps in understanding the fundamental phase transformation characteristics of this TRIP-HEA. The following salient observations and conclusions can be made:

1. $Fe_{42}Co_{10}Cr_{15}Mn_{28}Si_5$ HEA exhibits microstructural evolution through discontinuous dynamic recrystallization due to FSW. The stir zone (SZ) is found to be more susceptible to the deformation-induced martensitic transformation compared to the base metal (BM) specimen. Deformation created by the trailing edge of the FSW tool subsequently transforms γ-matrix to ε-martensite phase.
2. Grain refinement influences the type of martensitic transformation and improves strain hardenability of the $Fe_{42}Co_{10}Cr_{15}Mn_{28}Si_5$ HEA because of enhanced phase transformation upon deformation.
3. PRW technique should produce sound welds for the $Fe_{42}Co_{10}Cr_{15}Mn_{28}Si_5$ HEA with the minimum heat input threshold of 810 J. The microstructure after the welding exhibits recrystallized grain structure.
4. Finite element analysis depicts the state of the heat distribution and deformation during PRW with a predominant thermal/strain field at the side of the smaller coupon. This prediction agrees well with the experimental observations.

In this work, a detailed study on the deformation mechanism and high temperature properties of $Al_{0.4}CoCrFeNi$ HEA reveal the plasticity of this HEA system which has not been examined in detail in prior studies. This alloy shows good hardenability that comes from the microbands induced plasticity (MBIP). This fundamental study will help us understand the mechanism of the MBIP generation and designing of alloys. From this part of the study, the following observations/conclusions are made:

1. Dislocation dynamics in this HEA involves microband formation that initiate from the presence of stair rod dislocation. The MBIP deformation mechanism increases the strain hardening capability of this HEA.
2. Micropillar compression testing from the two differently oriented micropillars, [001] and [111], shows the anisotropic nature of the alloy. The critical resolved shear stress (CRSS) is higher

than the conventional TWIP steel. This is the result of the presence of the short-range order phase in the $Al_{0.4}CoCrFeNi$ HEA.

3. The $Al_{0.4}CoCrFeNi$ HEA shows serrated flow at 600ºC, being more prominent in the solutionized specimen compared to the as cast one, which is the result of the solute atoms being dissolved in the matrix and interacting with dislocations. Negative or negligible strain rate sensitivity obtained in this HEA points toward the operation of dynamic strain aging under the testing conditions.
4. Thermal expansion in this HEA is considerably greater than typical FCC alloy.

Some future work recommendations can lead to further advancement of these particular research areas undertaken in this dissertation work:

1. Do mini tensile testing on the friction stir welded $Fe_{42}Co_{10}Cr_{15}Mn_{28}Si_5$ HEA to investigate the tensile properties and ductility of the HEA to examine tension-compression asymmetry, if any.
2. Conduct more PRW on the $Fe_{42}Co_{10}Cr_{15}Mn_{28}Si_5$ HEA to refine the PRW parameter window for producing sound weld.
3. Improve the PRW model of the $Fe_{42}Co_{10}Cr_{15}Mn_{28}Si_5$ HEA using ABAQUS FEA analysis.
4. Study the dislocation structure of the $Al_{0.4}CoCrFeNi$ HEA by using high-resolution TEM for atomic-scale imaging.
5. Conduct tensile testing on $Al_{0.4}CoCrFeNi$ HEA to inspect the effect of microbands on the ductility of the HEA.